University of California
Santa Barbara

Revealing the Progenitor Systems of Type Ia Supernovae with Early High-cadence Multiwavelength Data

A dissertation submitted in partial satisfaction
of the requirements for the degree

Doctor of Philosophy
in
Physics

by

Jamison Frost Burke

Committee in charge:

Professor D. Andrew Howell, Co-Chair
Professor Lars Bildsten, Co-Chair
Professor Timothy Brandt

December 2022

The dissertation of Jamison Frost Burke is approved.

Professor Timothy Brandt

Professor Lars Bildsten, Committee Co-Chair

Professor D. Andrew Howell, Committee Co-Chair

October 2022

Revealing the Progenitor Systems of Type Ia Supernovae with Early High-cadence Multiwavelength Data

by

Jamison Frost Burke

"[T]he best material model for a cat is another, or preferably the same cat."

–Arturo Rosenblueth and Norbert Wiener, "The Role of Models in Science"

"And what rough beast, its hour come round at last,
Slouches towards Bethlehem to be born?"

–W. B. Yeats, "The Second Coming"

Acknowledgements

To quote the Netflix show Russian Doll, "No one can do anything by themselves." I could not have got through this PhD without the help and support of an enormous number of people.

I would like to thank the American taxpayer for funding this work through a medley of grants, primarily NSF grants AST-1313484 and AST-1911225, as well as by NASA grant 80NSSC19kf1639. Couldn't have done it without you.

Thank you to the many mentors I have had over the years, whether I met them directly or not: to Mr. Rodgers, who initially inspired my love of physics and scientific rigor; to David Cohen and Eric Jensen at Swarthmore, who introduced me to the astronomical community; to Carl Sagan, who got arrested multiple times while protesting for nuclear disarmament and who showed me that astrophysics and activism are not mutually exclusive; and lastly of course to my current advisor Andy Howell, who showed me that you can do serious science and still have some fun on the side too.

To my labmates, past and present: Iair, Curtis, Griffin, Giacomo, Craig, Joseph, Este, Megan, and Daichi – thank you all for making the office a great place to work, for answering my seven million questions about how things work, for asking me several million more questions, and (to Joseph) for driving faster than you were supposed to when I was in the car on the drag strip.

To my coworkers for one brief summer in the Emirates, thank you for the temporary diversion from my research, for the many late and long and interesting conversations, and for going on some adventures into the desert together: Carrie, Carla, Tony, Brittany, and Brittney. Camel Crew forever.

Thanks to the broader LCO community, to Lisa, Austin, David, Lindy, Rachel, Joey, Matt, Nan, Jody, Sarah, and everyone else, for both running this crazy machine and

for making the office experience more pleasant than most grad students will ever get. Thanks to the softies for all your time spent training me (and other astronomers) on how to write functioning code, may we pay you back somehow sometime.

In what I assume is a first in the acknowledgments section of a UCSB Physics dissertation, a big thank you to everyone at Mountain Lake Biological Station in western Virginia: Butch, Tom, Joseph, station Jaime, both Davids, all the Hannahs, everyone in the Brodie lab, the REU students and everyone else who played volleyball, and Eric, for using a projector and a bedsheet to show Rocky Horror on the side of his RV, allowing me to scream obscenities next to my partner's advisor. Thanks also to Fisher, for constructing a smoker out of a used industrial sink so we could roast whole pigs for the Fourth of July, and thanks to everyone involved in making pig sink quesadillas in the wee hours of the Fourth. A sincere thank you to everyone for the beautiful experiences in a beautiful place, I couldn't imagine a better way to spend the summers.

Thanks to everyone in the Global Supernova Project, especially Dave (practically my second advisor, science forever), Rachael, Peter, Saurabh, and Marc, for your varied subjects of expertise and for keeping the Project alive and functioning. And a special shoutout to Azalee, who spearheaded the push to make our pipeline better and more portable over the pandemic. You have distributed the labor of data reduction and are helping to train and motivate new people, thank you.

To all my cohort-mates and UCSB friends, Byron, Jakkarin, Mike, Jared, Mark, Dan, Mirek, Sarah, Will, and to long-lost Gino and all the rest, thanks for coming to this campus by the sea, I wish you luck with the rest of your lives.

To my roommates, past and present, and to the rest of movie night crew: Alex, Dylan, Gabi, Bryant, Zach, Nic, Jenny, Cosmo, Roxy, and Leela. There's no one else I'd rather shriek at a television with. Thank you for the joy.

To those two guys in a truck in Orange County who unexpectedly gave me a ride

to the trailhead, to that nice old couple in Redwoods National Park who gave me and my bike a lift when I'd gone a little too far into the woods, to those folks who kept me company during the last few miles of the Mt. Whitney trail, thanks for the kindness of strangers and for sharing California's many beautiful public lands with me.

Thanks to the various internet content creators with whom I formed parasocial relationships during the course of the pandemic, especially Magi and Contrapoints. Thanks also to all the authors who have provided me some much-needed wonder, peace, and food for thought, especially Ursula K. Le Guin, Brian K. Vaughan and Fiona Staples, Tamsyn Muir, Torrey Peters, Connie Willis, Ted Chiang, and Hidetaka Miyazaki. My life is richer for all of your tangential inclusions.

Thanks of course to my family, mom, dad, Chris, Emily, Will, and Radar, for being surprisingly functional! Go us. And thanks to other old friends: to Peter, for being a part of such a wonderful little book club; to Matt, may we each find something both enjoyable and useful to do with our lives; and to the recently resurrected ML Tables crew (Dyan, Ashley, Liz, Books, Erika, and all y'all), may we continue to host Salons of Literary Decline.

Thanks to everyone in my new hometown, Pittsburgh, for being so welcoming: to Ollie, Murphy, Tessa, the rest of the Fresh Fruits and the wider PGH queer bocce community, and everyone in the PGH Melee scene. I'm excited to live among such excellent and admirable folk.

Lastly, thanks are due in immeasurable quantity to my partner, Phoebe. Thank you for being a constant source of joy and support as we both figure out what to do with our lives. It's hard to imagine the person I would be today if I hadn't met you 11 years ago. I can't wait to make our future together.

Curriculum Vitæ

Jamison Frost Burke

EDUCATION

University of California, Santa Barbara September 2016 – December 2022
Ph.D. Physics, Astrophysics Emphasis, September 2022
M.A. Physics, Astrophysics Emphasis, November 2019
Advisor: Professor D. Andrew Howell

Swarthmore College August 2011 – May 2015
B.A. Classical Studies and Astrophysics

RESEARCH

Las Cumbres Observatory January 2017 – December 2022
Graduate Student Researcher
Global Supernova Project and the Supernova Key Project
Advisor: D. Andrew Howell

Kitt Peak National Observatory June 2014 – August 2014
REU student
LSST Site Performance
Advisor: Chuck Claver

University of Wyoming June 2013 – August 2013
REU student
Massive Star Binarity in the Cygnus OB2 Association
Advisor: Chip Kobulnicky

OBSERVING

Las Cumbres Observatory January 2017 – Present
Imaging with Sinistro, SBIG, MuSCAT, and Spectral
Spectroscopy with FLOYDS

Gemini Observatory June 2017 – Present
Spectroscopy with the Gemini Multi-Object Spectrographs

Neil Gehrels *Swift* Observatory December 2018 – Present
Imaging with the Ultraviolet/Optical Telescope
Imaging and spectroscopy with the X-Ray Telescope

Lick Observatory October 2018
Imaging with the Nickel Direct Imaging Camera
Spectroscopy with the Kast Double Spectrograph and Hamilton Echelle Spectrograph

W. M. Keck Observatory August 2018
Spectroscopy with the Low Resolution Imaging Spectrometer

Wyoming Infrared Observatory June 2013 – August 2013
Spectroscopy with the WIRO Long-Slit spectrograph

Peter van de Kamp Observatory August 2018
Optical imaging

TEACHING

Johns Hopkins Center for Talented Youth July 2019 – August 2019
Instructor of record
Introduction to Astronomy

University of California, Santa Barbara September 2016 – June 2018
Teaching Assistant
ASTRO 1 – Basic Astronomy

Cape Henry Collegiate School January 2016 – June 2016
High school teacher
Latin I–IV and AP Latin

Swarthmore College January 2014 – May 2015
Lab assistant
Astro 1: Introductory Astronomy
Course creator and instructor of record
Classics 93 & 94: Survey of Greek and Roman Literature

OUTREACH

Astronomy on Tap Santa Barbara January 2018 – February 2020
Organizer and host of free, short, public, astronomy-related presentations in a bar

AWARDS & HONORS

Brython Davis Fellowship Fall 2018
University of California, Santa Barbara

Outstanding Teaching Assistant Award 2017 – 2018
University of California, Santa Barbara

SOFTWARE

`snex2` github.com/jfrostburke/snex2
Manages targets and observations for the Global Supernova Project

`lcogtsnpipe` github.com/LCOGT/lcogtsnpipe
Measures photometry on images from the Las Cumbres Observatory

`floyds_pipeline` github.com/LCOGT/floyds_pipeline
Reduces spectra from the Las Cumbres Observatory FLOYDS spectrographs

PRESENTATIONS

10. Mountain Lake Biological Station summer seminar series — July 2021
"Supernovae: Observations of Dying Stars"
9. UCSB Lunch & Learn (virtual) — July 2021
"Supernovae: Observations of Dying Stars"
8. LSSTC Enabling Science 2021 Broker Workshop part II (virtual) — April 2021
"Supernova Exchange 2.0: Utilizing the TOM Toolkit"
7. UCSB Astro Tea (virtual) — January 2021
"A Bright UV Excess in the Transitional 02es-like Type Ia Supernova 2019yvq"
6. AAS 235 — January 2020
"Optical Photometric Inhomogeneities in a Sample of 9 Type Ia Supernova"
5. Managing Follow-up Observations in the Era of ZTF and LSST — September 2019
"SNEx 2.0"
4. Hot-Wiring the Transient Universe VI — August 2019
"Using the TOM Toolkit to Upgrade the Supernova Exchange"
3. UCSB Astro Lunch — October 2018
"Inhomogeneities in Early Type Ia Supernova Lightcurves"
2. KNAC undergraduate research symposium — August 2014
"LSST Site: Sky Brightness"
1. KNAC undergraduate research symposium — August 2013
"The Cygnus OB2 Radial Velocity Survey"

PUBLICATIONS

Lead Author

3. Burke, J. et al. 2022, "Companion Shocking Fits to the 2018 ZTF Sample of SNe Ia Are Consistent with Single-Degenerate Progenitor Systems," submitted to ApJ (arXiv:2208.11201)
2. Burke, J. et al. 2022, "Early Lightcurves of Type Ia Supernovae are Consistent with Nondegenerate Progenitor Companions," submitted to ApJ (arXiv:2207.07681)
1. Burke, J. et al. 2021, "A Bright Ultraviolet Excess in the Transitional 02es-like Type Ia Supernova 2019yvq," ApJ, 919, 142

Co-author

59. Hosseinzadeh, G. et al. 2022, "Weak Mass Loss from the Red Supergiant Progenitor of the Type II SN 2021yja," ApJ, 935, 31
58. Medler, K. et al. 2022, "SN 2020acat: an energetic fast rising Type IIb supernova," MNRAS, 513, 5540

57. Valerin, G. et al. 2022, "Low luminosity Type II supernovae – IV. SN 2020cxd and SN 2021aai, at the edges of the sub-luminous supernovae class," MNRAS, 513, 4983

56. Hosseinzadeh, G. et al. 2022, "Constraining the Progenitor System of the Type Ia Supernova 2021aefx," ApJL, 933, 45

55. Fiore, A. et al. 2021, "Close, bright and boxy: the superluminous SN 2018hti," MNRAS, 512, 4484

54. Gangopadhyay, A. et al. 2022, "Evolution of A Peculiar Type Ibn Supernova SN 2019wep," ApJ, 930, 127

53. Graham, M.L. et al. 2022, "Nebular-Phase Spectra of Type Ia Supernovae from the Las Cumbres Observatory Global Supernova Project," MNRAS, 511, 3682

52. Irani, I. et al. 2021, "Less than 1% of Core-Collapse Supernovae in the local universe occur in elliptical galaxies," ApJ, 927, 10

51. Ni, Y. et al. 2022, "Infant-phase reddening by surface Fe-peak elements in a normal Type Ia Supernova," NatAs, 6, 568

50. Pellegrino, C. et al. 2021, "Circumstellar Interaction Powers the Light Curves of Luminous Rapidly-evolving Optical Transients," ApJ, 926, 125

49. Wang, Q. et al. 2021, "SN2018agk: A prototypical Type Ia Supernova with a smooth power-law rise in Kepler (K2)," ApJ, 923, 167

48. Sand, D. J. et al. 2021, "Circumstellar Medium Constraints on the Environment of Two Nearby Type Ia Supernovae: SN 2017cbv and SN 2020nlb," ApJ, 922, 21

47. Parrag, E. et al. 2021, "SN 2019hcc: a Type II supernova displaying early O II lines," MNRAS, 506, 4819

46. Jencson, J. et al. 2021, "AT 2019qyl in NGC 300: Early Outflow Collisions for a Very Fast Nova in a Symbiotic Binary," ApJ, 920, 127

45. Johansson, J. et al. 2021, "Near-IR Type Ia SN distances: host galaxy extinction and mass-step corrections revisited," ApJ, 923, 237

44. Kilpatrick, C. et al. 2021, "The Gravity Collective: A Search for the Electromagnetic Counterpart to the Neutron Star-Black Hole Merger GW190814," ApJ, 923, 258

43. Zeng, X. et al. 2021, "SN 2017fgc: A Fast-Expanding Type Ia Supernova Exploded in Massive Shell Galaxy NGC 474," ApJ, 919, 49

42. Utrobin, V. P. et al. 2021, "Enormous explosion energy of Type IIP SN 2017gmr with bipolar ^{56}Ni ejecta," MNRAS, 505, 116

41. Gutiérrez, C. P. et al. 2021, "The double-peaked Type Ic supernova 2019cad: another SN 2005bf-like object," MNRAS, 504, 4907

40. Medler, K. et al. 2021, "SN 2020cpg: an energetic link between type IIb and Ib supernovae," MNRAS, 506, 1832

39. Hiramatsu, D. et al. 2021, "Luminous Type II Short-Plateau Supernovae 2006Y, 2006ai, and 2016egz: A Transitional Class from Stripped Massive Red Supergiants," ApJ, 913, 55

38. Baltay, C. et al. 2021, "Low-redshift Type Ia Supernova from the LSQ/LCO Collaboration," PASP, 133, 4002

37. Xiang, D. et al. 2021, "The Peculiar Transient AT 2018cow: A Possible Origin of a Type Ibn/IIn Supernova," ApJ, 910, 42

36. Zeng, X. et al. 2021, "SN 2017hpa: A Nearby Carbon-rich Type IA Supernova with a Large Velocity Gradient," ApJ, 909, 176

35. Khetan, N. et al. 2021, "A new measurement of the Hubble constant using Type Ia supernovae calibrated with surface brightness fluctuations," A&A, 647, 72

34. Rho, J. et al. 2021, "Near-Infrared and Optical Observations of Type Ic SN 2020oi and Broad-lined Ic SN 2020bv," ApJ, 908, 232

33. Tartaglia, L. et al. 2021, "The Early Discovery of SN 2017ahn: Signatures of Persistent Interaction in a Fast-declining Type II Supernova," ApJ, 907, 52

32. Dong, Y. et al. 2021, "Supernova 2018cuf: A Type IIP Supernova with a Slow Fall from Plateau," ApJ, 906, 56

31. Jacobson-Galan, Wynn V. et al. 2021, "SN 2019ehk: a Double-peaked Ca-rich Transient with Luminous X-Ray Emission and Shock-ionized Spectral Features," ApJ, 898, 166

30. Prentice, S. J. et al. 2020, "SN 2018gjx confirms that some SNe Ibn are SNe IIb exploding in dense circumstellar material," MNRAS, 499, 1450

29. Nicholl, Matt et al. 2020, "An outflow powers the optical rise of the nearby, fast-evolving tidal disruption event AT2019qiz," MNRAS, 499, 482

28. Hiramatsu, Daichi et al. 2020, "The electron-capture origin of supernova 2018zd," Nature Astronomy, 5, 903

27. Müller-Bravo, Tomás E. et al. 2020, "The low-luminosity Type II SN 2016aqf: a well-monitored spectral evolution of the Ni/Fe abundance ratio," MNRAS, 497, 361

26. Barna, Barnábas et al. 2021, "SN 2019muj – a well-observed Type Iax SN fills the gap in the subclass," MNRAS, 501, 1078

25. Fiore, A. et al. 2021, "SN 2017gci: a nearby Type I Superluminous Supernova with a bumpy tail," MNRAS, 502, 2120

24. Pritchard, T. A. et al. 2020, "The Exotic Type Ic Broad-Lined Supernova SN 2018gep: Blurring the Line Between Supernovae and Fast Optical Transients," ApJ, 915, 121

23. Gutiérrez, C. P. et al. 2020, "SN 2017ivv: two years of evolution of a transitional Type II supernova," MNRAS, 499, 974

22. Short, P. et al. 2020, "The Tidal Disruption Event AT 2018hyz: - I. Double-peaked emission lines and a flat Balmer decrement," MNRAS, 498, 4119

21. Yang, Y. et al. 2020, "The Young and Nearby Normal Type Ia Supernova 2018gv: UV-Optical Observations and the Earliest Spectropolarimetry," ApJ, 902, 46

20. Pellegrino, C. et al. 2020, "Constraining the Source of the High Velocity Ejecta in the Type Ia SN 2019ein," ApJ, 897, 159

19. Han, X. et al. 2020, "SN 2017cfd: A Normal Type Ia Supernova Discovered Very Young," ApJ, 892, 142

18. Gangopadhyay, A. et al. 2020, "Flash ionisation signatures in Type Ibn supernova SN 2019uo," ApJ, 889, 170

17. Bostroem, K. A. et al. 2020, "Discovery and Rapid Follow-up of the type II SN 2018ivc in NGC 1068," ApJ, 895, 31

16. Dastidar, R. et al. 2019, "SN 2015an: a normal luminosity type II supernova with low expansion velocity at early phases," MNRAS, 490, 1605

15. Andrews, J. et al. 2019, "SN 2017gmr: An energetic Type II-P supernova with asymmetries," ApJ, 885, 43

14. Trakhtenbrot, B. et al. 2019, "1ES 1927+654: an AGN Caught Changing Look on a Timescale of Months," ApJ, 883, 94

13. Galbany, L. et al. 2019, "On the Ca-strong 1991bg-like type Ia supernova 2016hnk: evidence for a Chandrasekhar-mass explosion," A&A, 630, A76

12. Sand, D. et al. 2019, "Nebular Hα Limits for Fast Declining Type Ia Supernovae," ApJ, 877L, 4

11. Pastorello, A. et al. 2019, "A luminous stellar outburst during a long-lasting eruptive phase, then SN IIn 2018cnf," A&A, 628, A93

10. Szalai, T. et al. 2019, "The Type II-P Supernova 2017eaw: From Explosion to the Nebular Phase," ApJ, 876, 19

9. Leloudas, G. et al. 2019, "The Spectral Evolution of AT 2018dyb and the Presence of Metal Lines in Tidal Disruption Events," ApJ, 887, 218

8. Li, W. et al. 2019, "Photometric and Spectroscopic Properties of Type Ia Supernova 2018oh(ASASSN-18bt) with Early Excess Emission from the Kepler 2 Observations," ApJ, 870, 12

7. Sollerman, J. et al. 2019, "Late-time observations of the extraordinary Type II supernova iPTF14hls," A&A, 621, 30

6. Dimitriadis, G. et al. 2018, "K2 Observations of SN 2018oh Reveal a Two-Component Rising Light Curve for a Type Ia Supernova," ApJL, 870, 1

5. Anderson, J. et al. 2018, "A nearby superluminous supernova with a long pre-maximum 'plateau' and strong CII features," A&A, 620, 67

4. Sand, D. et al. 2018, "Nebular Spectroscopy of the 'Blue Bump' Type Ia Supernova 2017cbv," ApJ, 663, 24
3. De, K. et al. 2018, "A hot and fast ultra-stripped supernova forming a compact neutron star binary," Science, 362, 201
2. McCully, C. et al. 2017, "The Rapid Reddening and Featureless Optical Spectra of the Optical Counterpart of GW170817, AT 2017gfo, during the First Four Days," ApJL, 848, L32
1. Kobulnicky, H. A. et al. 2014, "Toward Complete Statistics of Massive Binary Stars: Penultimate Results from the Cygnus OB2 Radial Velocity Survey," ApJS, 213, 34

Astronomical Circulars

256 transient classifications and circulars (87 as lead author).

Abstract

Revealing the Progenitor Systems of Type Ia Supernovae with Early High-cadence Multiwavelength Data

by

Jamison Frost Burke

Over 10,000 astronomical transients are now discovered every year. Pairing this wealth of objects with rapid followup facilities such as Las Cumbres Observatory (LCO) allows for high-cadence multiwavelength characterization of supernovae (SNe) within days or even hours of their explosion. Although Type Ia SNe (SNe Ia) are a relatively homogeneous population around peak brightness, notably used as standardizable candles to measure cosmological parameters, at early times their lightcurves show a dramatic range of behavior. One effect sometimes visible in their early lightcurves is a UV excess, likely indicative of the exploding white dwarf having a nondegenerate companion which shocks the SN ejecta as the two collide. Studying their varied early lightcurves can thus reveal information about their progenitor systems, which remain poorly understood beyond the fact that the explosion originates from a white dwarf. Here I present three advancements in SNe Ia research: (1) SN 2019yvq is a SN Ia which displayed the strongest early UV excess ever observed in SNe Ia. This SN shared some characteristics with a rare subclass of SNe Ia called 02es-likes, which for some reason seem to display these excesses more frequently than their predicted rarity. (2) In a sample of 9 SNe Ia with excellent early data from LCO, the distribution of early excess strengths and best-fit viewing angles are consistent with the progenitor systems of SNe Ia predominantly containing a nondegenerate companion. (3) In a sample of 127 SNe Ia observed by the ZTF survey, the rate of early excesses is again consistent with the single-degenerate progenitor scenario.

Contents

Chapter 1

Introduction

1.1 Supernovae

Supernovae (SNe) are the terminal explosions of massive stars or white dwarfs (WDs). They are so bright that they can outshine their host galaxies and be seen at cosmological distances (see Figure 1.1). SNe are relevant to every scale of astrophysics: on the nuclear scale, they are the sites of nucleosynthesis; on the stellar scale, they are the endpoints of stellar evolution; on the galactic scale, they can induce star formation and drive galactic winds; and on the cosmological scale, SNe Ia are used as standardizable candles to measure cosmological parameters. They are important as endpoints of stellar evolution and as probes of extreme physics, but many aspects of them remain poorly understood.

1.2 Early Blue Excesses in SNe Ia

This thesis focuses on Type Ia SNe (SNe Ia). As discussed in the introductory sections of later chapters, SNe Ia have been understood for decades to be the explosions of white dwarfs (Hoyle & Fowler 1960). There is consensus on that statement, but beyond that almost every detail about their physical systems, notably the precise explosion mechanism and the makeup of the progenitor system, is hotly debated.

The white dwarfs most likely explode due to accretion onto them from a companion. That companion could be another white dwarf (often referred to as the double-degenerate case, see Iben & Tutukov 1984) or the companion could be a non-degenerate main sequence or red giant star (the single-degenerate case, see Whelan & Iben 1973). In the single-degenerate scenario, Kasen (2010) predicted that as the SN ejecta collide with the companion it will get shock-heated, resulting in excess flux especially in blue/UV bands visible in the days after explosion.

Figure 1.2 reproduces salient figures from Kasen (2010), showing schematically the collision of ejecta with a companion (top panel), and also its effect on the SN's lightcurve (bottom panel). Crucially, the strength of the observed early excess is highly dependent on the viewing angle of the system: even if every SN Ia arose from a single-degenerate progenitor system, and even if every object was observed with the early, high-cadence, multiwavelength data needed to characterize such early excesses, you would still only see strong early excesses in $\sim$10% of events due to viewing angle effects.

These early excesses are difficult to observe, and have primarily been reported in a handful of single-object papers (see the introductory sections of the following chapters for lists). They occur when the SN is $\sim$2.5 magnitudes fainter than its peak magnitude: for a sample of SNe Ia discovered by magnitude-limited surveys, this will automatically limit the number of objects where such an excess could be observed to a few percent of the sample, and the viewing angle effect will again limit the fraction of objects with observable excesses to a further $\sim$10% of that subsample. Since the excesses are wavelength-dependent, you need multiwavelength data to fully characterize them and compare to predictions, and since the effect only lasts for a few days before the shocked ejecta dissipate and cool you need high-cadence data to observe them at all. The data needed to observe these early excesses must therefore be early, high-cadence, and multiwavelength, which is exactly the kind of followup that Las Cumbres Observatory is optimally suited

to provide.

1.3 Las Cumbres Observatory

Las Cumbres Observatory (LCO; Brown et al. 2013) consists of a network of twenty-five robotic optical telescopes at seven different sites around the world (see Figure 1.3), and is a primary data source for Chapters 2 and 3. The telescopes are remotely scheduled and robotically controlled, and collectively operate as a single facility. Since the telescopes are distributed in longitude across both the northern and southern hemisphere, they allow for prompt and continuous monitoring of any kind of optical astronomical transient.

The SN group at LCO consists of eight members who share responsibilities in selecting new targets for observation, monitoring data acquisition, reducing data, and maintaining our data reduction pipelines. In addition to a wide variety of research on SNe, we were also one of the six teams that independently discovered the first kilonova (Abbott et al. 2017), although I will not be discussing that work here.

Beyond the eight members of the SN group at LCO we also draw upon the experience of the Global Supernova Project (GSP; Howell & Global Supernova Project 2017), a global collaboration of more than 150 SN observers and theorists. The GSP is also one of the Key Projects at LCO, with access to more than 3000 hours of telescope time per year, allowing us to monitor ∼50 SNe at any given time. The large collaboration provides expertise in all subtypes and aspects of SNe, in addition to telescope time at the world's largest ground-based telescopes, such as the W. M. Keck Observatory and Gemini Observatory, as well as space-based telescopes such as the Neil Gehrels *Swift* Observatory and *Hubble Space Telescope* (*HST*). This enables observations across the electromagnetic spectrum, from X-ray to mid-infrared, allowing us to study aspects of SNe inaccessible at optical wavelengths. We also closely collaborate with the Public ESO

Spectroscopic Survey for Transient Objects (PESSTO; Smartt et al. 2015), which uses the 3.58 m New Technology Telescope (NTT) for SN classifications and follow-ups.

The GSP focuses on SN followup, and so we rely on other groups to discover the objects. The objects which are the focus of Chapters 2 and 3 were all discovered by either the Distance Less Than 40 Mpc survey (DLT40; Tartaglia et al. 2018) or by the amateur astronomer Koichi Itagaki. Our close collaboration with DLT40 and Koichi Itagaki enabled the most interesting observations presented here due to their high-cadence nearby-galaxy-targeted searches, which are optimally suited to discover young and interesting SNe. We also monitor alert streams from the Asteroid Terrestrial-impact Last Alert System (ATLAS; Tonry et al. 2018) and the Zwicky Transient Facility (ZTF, the data source for Chapter 4; Bellm et al. 2019), which collectively have discovered more than 25000 astronomical transients[1].

[1]See https://www.wis-tns.org/stats-maps for the current discovery counts.

Figure 1.1: Las Cumbres Observatory color composite of the Type Ia SN 2011fe hosted in the Pinwheel Galaxy (M101). Image courtesy of BJ Fulton.

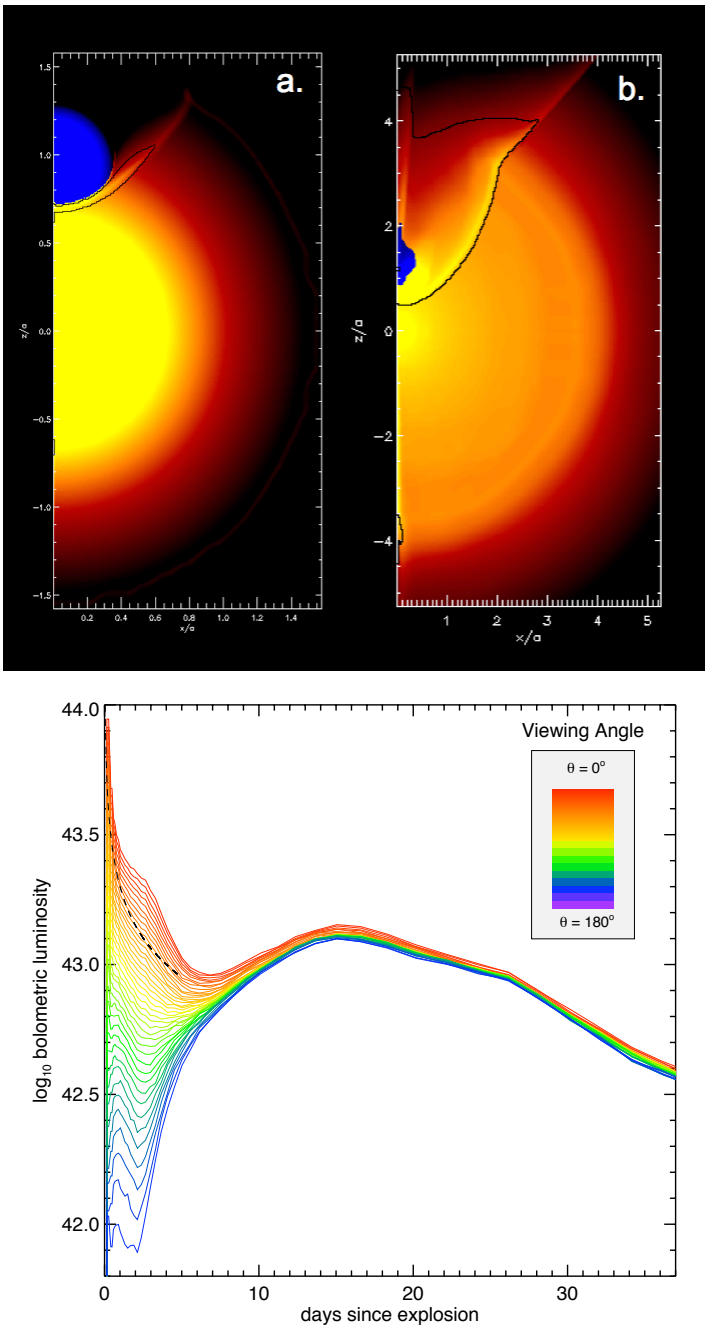

Figure 1.2: Figures reproduced from Kasen (2010). *Top:* A diagram of the SN ejecta (in red) colliding with a red giant companion (in blue), seen at two time snapshots (time progressing from the left to the right panel). The black contour in the right panel shows where the ejecta has been shock-heated to $> 10^5$ K. *Bottom:* The observed strength of the early excess is highly dependent on viewing angle. The dashed black line represents the analytic formulation used throughout Chapters 2, 3, and 4.

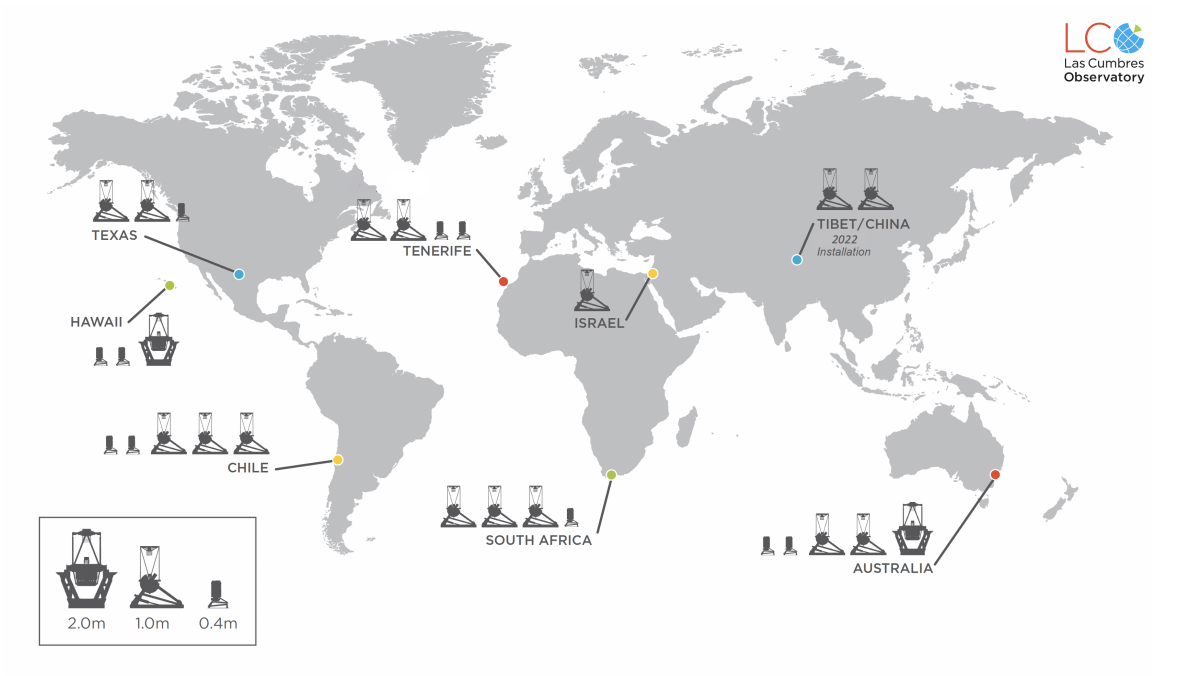

Figure 1.3: A map of Las Cumbres Observatory's global telescope network with twenty-five robotic 2 m, 1 m, and 0.4 m telescopes, as of September 2022. Two additional two 1 m telescopes in Tibet are expected to be installed within the next year. The growing global telescope network allows unprecedented time coverage of astronomical transients.

Chapter 2

A Bright Ultraviolet Excess in the Transitional 02es-like Type Ia Supernova 2019yvq

This chapter is reproduced from Burke et al. (2021) by permission of the American Astronomical Society. I would like to thank my coauthors, without whom this work would not have been possible: D. Andrew Howell, Sumit K. Sarbadhicary, David J. Sand, Rachael C. Amaro, Daichi Hiramatsu, Curtis McCully, Craig Pellegrino, Jennifer E. Andrews, Peter J. Brown, Koichi Itagaki, Melissa Shahbandeh, K. Azalee Bostroem, Laura Chomiuk, Eric Y. Hsiao, Nathan Smith, and Stefano Valenti.

2.1 Introduction

Despite the fact that Type Ia supernovae (SNe) were used as standardizable candles to discover the accelerating expansion of the universe and constrain its energy content (Riess et al. 1998; Perlmutter et al. 1999), open questions remain about their progenitor systems. The SNe themselves are understood to be the thermonuclear explosions of carbon/oxygen white dwarfs (WDs) (Hoyle & Fowler 1960), but beyond that there are large uncertainties about both the progenitor system(s) and explosion mechanism(s).

Many possible progenitor systems have been theorized. The two broad classes are the single-degenerate channel (Whelan & Iben 1973), where the WD accretes matter slowly from a nondegenerate companion, and the double-degenerate channel (Iben & Tutukov 1984), where the source of the extra matter needed to ignite the WD is a second WD. Within these two broad channels exist many specific and sometimes exotic scenarios, e.g. dynamically driven double-degenerate double-detonation systems (Shen et al. 2018) or rotating super-Chandrasekhar mass WD progenitors (Yoon & Langer 2005). For reviews, see Howell (2011), Wang & Han (2012), and Maoz et al. (2014).

Kasen (2010) predicted an observational signature that could distinguish between the single- and double-degenerate cases. If the donor star were nondegenerate then the SN ejecta will run into it and get shock-heated. The shock-heated ejecta would then emit an excess of UV/blue light which could be detected in the SN's early-time lightcurve. The strength of this signature is dependent on the companion's size and separation, the velocity of the ejecta, and the viewing angle of the event. Kasen (2010) predicted that the viewing angle effect alone would make this early blue excess visible in only 10% of SNe Ia which explode through this single-degenerate channel.

Following the publication of Kasen (2010), many rolling supernova searches were examined for evidence of the effect in the optical and UV (Hayden et al. 2010; Bianco et al. 2011; Ganeshalingam et al. 2011; Tucker 2011). These found no evidence for the predicted shock with a red giant companion. Brown et al. (2012a) also excluded red giant companions from a smaller sample of SNe Ia with constraining UV data. The early optical observations of SN 2011fe were additionally able to place extremely tight constraints on optical and UV shock emission from the companion (Nugent et al. 2011; Brown et al. 2012b).

Early blue excesses have since been seen in a small number of SNe, most notably SN 2012cg (Marion et al. 2016), iPTF14atg (Cao et al. 2015), iPTF16abc (Miller et al. 2018),

and SN 2017cbv (Hosseinzadeh et al. 2017). The proliferation of transient surveys has allowed for much more consistent and thorough followup of young SNe (e.g. Yao et al. 2019). This in turn has revealed a wide range of early behaviors including varying early color evolution (Bulla et al. 2020; Stritzinger et al. 2018; Brown et al. 2017, 2018) and a range of (sometimes broken) power laws which describe their rising lightcurves (Olling et al. 2015; Miller et al. 2018, 2020b). The object SN 2018oh (Li et al. 2019), with its exquisitely sampled lightcurve from the *Kepler* space telescope, shows the clearest broken power law rise yet observed in an SN Ia. Although this object did not have multiwavelength followup until after the early excess (and thus it was not a definitively *blue* early excess), the *Kepler* lightcurve was the subject of intensive modeling (Shappee et al. 2019; Dimitriadis et al. 2019a) in an attempt to understand the progenitor system. SN 2018oh was a more typical SN Ia ($M_B = -19.47$) than SN 2019yvq ($M_B = -18.43$), but we include some of the same models used in the above papers to analyze the dataset of SN 2019yvq.

In addition to the Kasen (2010) companion shocking models, a number of other progenitor scenarios can reproduce some range of the observed properties of SNe Ia. This includes explosions which vary the degree of nickel mixing in the exploding WD (Piro & Morozova 2016) leading to a range of early colors, and models of sub-Chandrasekhar mass WDs detonated by the ignition of a surface layer of He (Polin et al. 2019) leading to a wide range of absolute magnitudes and colors.

In this paper we present early-time photometry and spectroscopy of the Type Ia SN 2019yvq, a SN discovered in late 2019 which displays a rare, and unusually strong, blue bump at early times. The object displays other unusual behavior, including extremely broad and high-velocity Si II at peak and strong nebular [Fe II] and [Ca II]. Its unique combination of characteristics make it an excellent stress-test for several models of SNe Ia. Multiple papers have already been written about this object (Miller et al. 2020a;

Siebert et al. 2020; Tucker et al. 2021), which we reference throughout, as this work agrees with prior findings in some respects and disagrees in others.

In Section 2.2 we describe the object's discovery by Itagaki (2019b) and its subsequent observational followup by Las Cumbres Observatory, which obtained data presented here for the first time, and the *Swift* space telescope. In Section 2.3 we discuss interesting features of the dataset, and we compare specifically to 02es-like SNe Ia in Section 2.4. In Section 2.5 we compare our UV, optical, and radio data to a range of models, and discuss the difficulty of finding a single model that reproduces all features of our dataset. We discuss implications of the event and its properties in Section 2.6. We conclude in Section 2.7.

2.2 Discovery & Observations

2.2.1 Discovery

SN 2019yvq was discovered by Koichi Itagaki (Itagaki 2019b) on 2019 December 28.74 UT using a Celestron 14 inch telescope at an unfiltered magnitude of 16.7. A nondetection of the same field, using an identical setup, was found the night before (2019 December 27.72 UT), with a limiting unfiltered magnitude of ∼18.2. This nondetection is approximately 0.3 days after the nondetection reported by ASAS-SN in Tucker et al. (2021), and places an even more stringent limit on the rise-time and early lightcurve. Following the initial discovery, both the ZTF (Bellm et al. 2019) and ATLAS (Tonry et al. 2018) surveys reported detections of SN 2019yvq. An initial classification spectrum using HOWPol on the 1.5-m Kanata telescope on 2020 January 01.84 suggested that SN 2019yvq was a Type Ib/c supernova (Kawabata 2020), although a subsequent spectrum (taken on 2020 January 4.07) with the SPRAT spectrograph on the Liverpool

telescope clearly showed that SN2019yvq was a SN Ia before maximum light. A spectrum from the SED Machine on the Palomar 60-in telescope taken on 2020 January 12.36 further confirmed that SN 2019yvq is a SN Ia. We have downloaded these spectra from the Transient Name Server (TNS)[1] and incorporated them into our analysis.

SN 2019yvq is located at right ascension $12^{\rm h}\,27^{\rm m}\,21\overset{\rm s}{.}85$ and declination $+64^{\circ}\,47'\,59\overset{''}{.}8$ (J2000) (Hodgkin et al. 2020), and lies 12.9 arcsec to the southeast of the host galaxy NGC 4441, which has a redshift of z=0.00908 (Rothberg & Joseph 2006 retrieved via NED[2]). NGC 4441 is an SAB0-type galaxy, and is clearly undergoing a merger event as can be seen in deep images from the DESI Legacy Imaging Survey[3] (Dey et al. 2019). A surface brightness fluctuation (SBF) distance to NGC 4441 suggests D≈20 Mpc (Tonry et al. 2001), although the disturbed nature of the host likely affects this measurement. The Hubble-flow distance is D≈40 Mpc, which is in agreement with the distance modulus calculated in Miller et al. (2020a). Both to be consistent with Siebert et al. (2020) and Tucker et al. (2021), and because using the SBF distance value would further decrease the object's already low luminosity, we adopt the distance modulus from Miller et al. (2020a) throughout this work ($\mu = 33.14 \pm 0.11$, $D = 42.5 \pm 2.2$ Mpc). We also adopt a Milky Way extinction value of $E(B-V) = 0.017$ mag using the Schlafly & Finkbeiner (2011) calibration of the Schlegel et al. (1998) dust maps.

2.2.2 Photometry

Figure 2.1 displays our full photometric dataset.

An intense *UBVgri* follow-up campaign was undertaken using the 1-m telescopes of Las Cumbres Observatory (LCO; Brown et al. 2013). Data were reduced using `lcogtsnpipe` (Valenti et al. 2016) by performing PSF-fitting photometry. Zeropoints

[1] https://wis-tns.weizmann.ac.il/
[2] http://ned.ipac.caltech.edu/
[3] http://legacysurvey.org/viewer

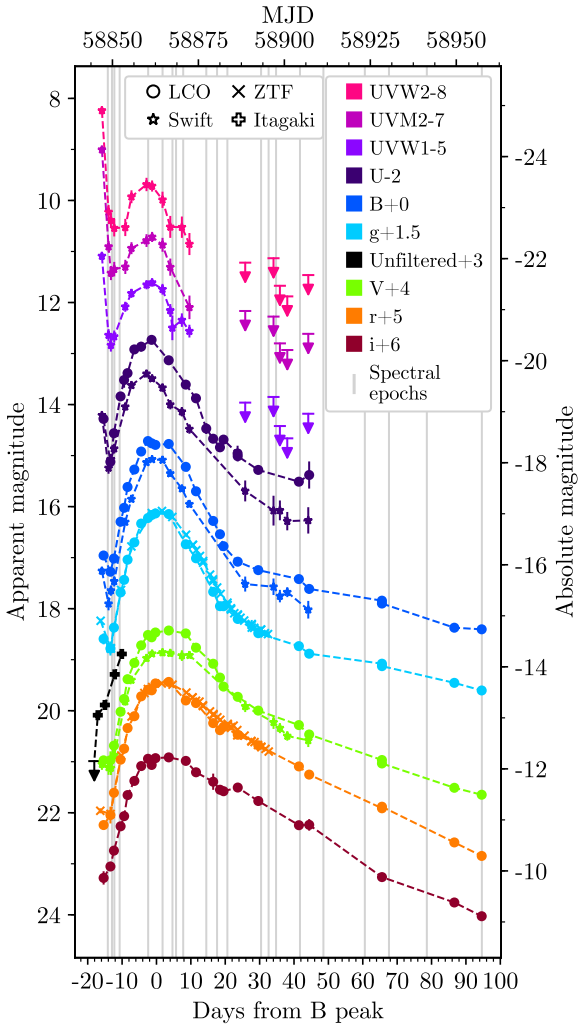

Figure 2.1: UV and optical extinction-corrected photometry of SN 2019yvq. As discussed in Section 2.3.1 we adopt $E(B-V)_{\rm host} = 0.052$ throughout our analysis, in addition to $E(B-V)_{\rm Milky\ Way} = 0.017$. The first epoch shows an extremely strong blue/UV excess. The lines connecting the points are simple linear interpolations to guide the eye, especially to the strength of the early UV excess, and do not represent models. The epochs of the spectra shown in Figure 2.2 are included as vertical grey lines.

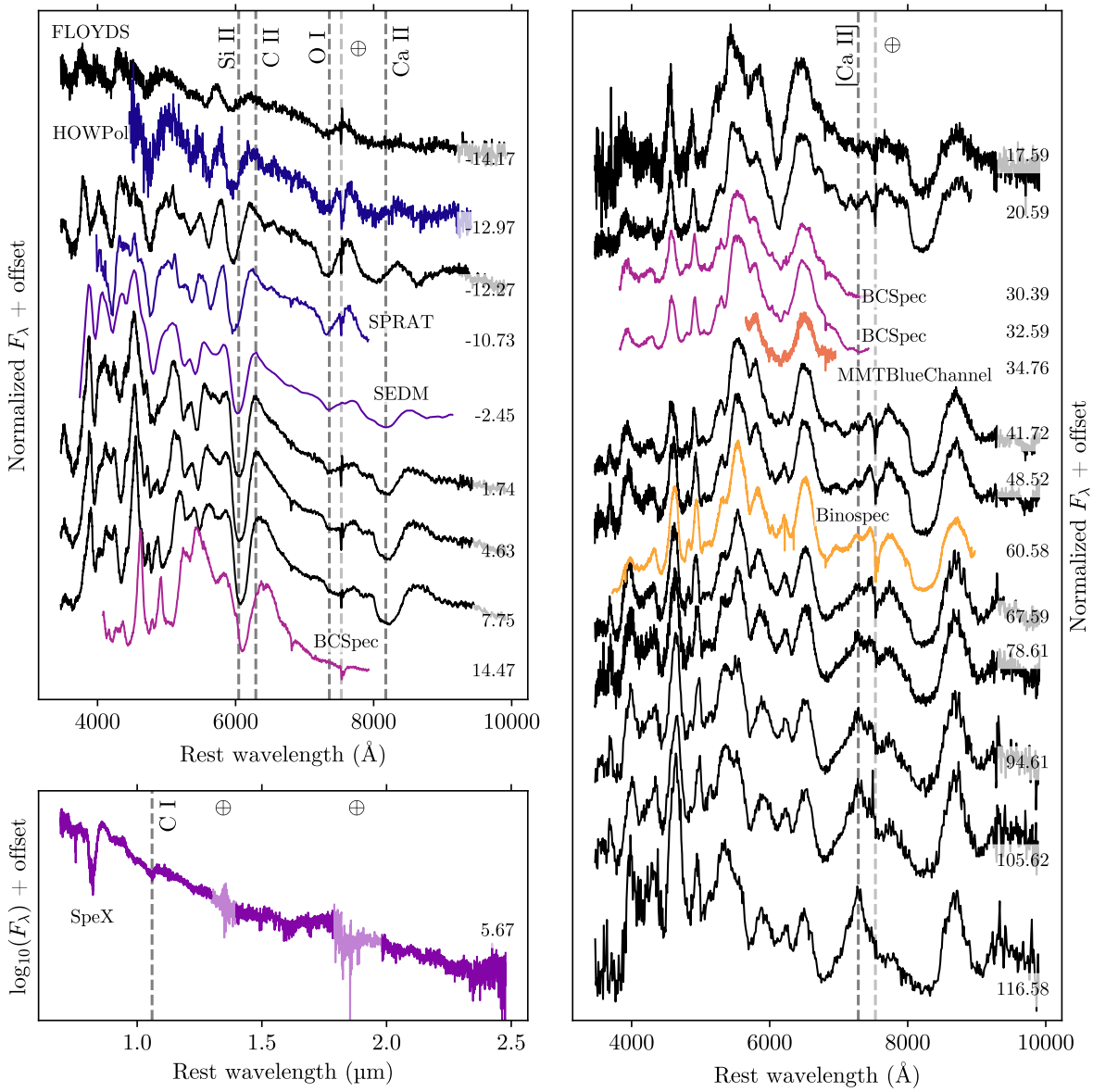

Figure 2.2: The top left and right-hand panels indicate the optical spectral evolution of SN 2019yvq, separated into panels purely for readability. The bottom left panel shows the IR spectrum at ∼6 days taken with SpeX on the IRTF (Section 2.2.3). Epochs (in days) with respect to B-band maximum are included as labels on each spectrum. The wavelengths of spectral features are marked with dashed lines, corresponding to their approximate velocity which they have at maximum light to guide the eye in tracking their velocity evolution. Telluric features are marked with ⊕. The primary source for spectra was the FLOYDS instrument at Las Cumbres (black spectra), but a number of other spectra (detailed in Sections 2.2.1 and 2.2.3) are included as well. The final three spectra have been binned by a factor of 5, for clarity.

for images in the *UBV* filters were calculated from Landolt standard fields (Landolt 1992) taken on the same night by the same telescope. Likewise, zeropoints for images in the *gri* filter set were calculated by using Sloan magnitudes of stars in the same field as the object (SDSS Collaboration et al. 2017).

Observations from the *Neil Gehrels Swift Observatory* (*Swift*; Gehrels et al. 2004) and the Ultra-Violet Optical Telescope (UVOT; Roming et al. 2005) were obtained under GI Program 1518168 and reduced using the pipeline associated with the *Swift* Optical Ultraviolet Supernovae Archive (SOUSA; Brown et al. 2014) and the zeropoints of Breeveld et al. (2010). The temporal sensitivity changes were corrected for using the 20200925 CALDB[4]. Template observations from 2012 were used to subtract the host galaxy count rates from the *UVW2*, *UVM2*, and *UVW1* filters.

In addition to the Las Cumbres and *Swift* photometric data, we have also obtained unfiltered photometry taken with the Itagaki Astronomical Observatory's Celestron 14-inch telescope in the days after discovery, including the nondetection taken the day prior to SN 2019yvq's discovery.

We gather g and r band data from the public ZTF data stream using the `MARS` transient broker[5], and present the near-peak data in Figure 2.1 as comparison.

2.2.3 Spectroscopy

Figure 2.2 displays our full spectroscopic dataset.

A sequence of optical spectra were taken primarily with the FLOYDS spectrograph mounted on Las Cumbres Observatory's 2-m telescope on Haleakalā, HI, and were reduced as described in Valenti et al. (2014).

[4] https://heasarc.gsfc.nasa.gov/docs/heasarc/caldb/swift/docs/uvot/uvotcaldb_throughput_06.pdf

[5] https://mars.lco.global/

Additional optical spectroscopy was obtained with the 2.3-m Bok telescope and the B&C spectrograph using both the 300 line/mm grating and a higher resolution 1200/mm line grating. We also obtained an MMT medium resolution (1200 l/mm) spectrum on 2020-02-18 11:27 UTC using the Blue Channel spectrograph (Schmidt et al. 1989). These data were reduced using standard IRAF tasks. We use the Na ID doublet in the high resolution data as one method of estimating host galaxy extinction from cold gas as discussed in Section 2.3.2.

Finally, a near-infrared spectrum of SN 2019yvq was taken on 2020 Jan 20 (UT) with SpeX (Rayner et al. 2003) on the NASA Infrared Telescope Facility in cross-dispersed 'SXD' mode, providing wavelength coverage from ∼0.8–2.4 μm; these data were reduced in a standard way, as described in Hsiao et al. (2019).

All new data are made publicly available on the Weizmann Interactive Supernova Repository[6](Yaron & Gal-Yam 2012).

2.3 Data Analysis

2.3.1 Lightcurve and Color Evolution Analysis

The lightcurve of SN 2019yvq is presented in Figure 2.1. The most striking feature of this lightcurve is the strong wavelength-dependent excess of the first epoch, seen in data from Las Cumbres, ZTF, and *Swift*. We note especially the excess in the mid-UV *Swift* filters, where the magnitude during the initial bump is brighter than the "peak" magnitude. This is even more extreme than other objects with an observed mid-UV excess at early times such as SN 2012cg (Marion et al. 2016) and iPTF14atg (Cao et al. 2015). We also note that SN 2017cbv (Hosseinzadeh et al. 2017), the SN Ia with the

[6] https://wiserep.weizmann.ac.il/

Method	$E(B-V)$	$\sigma_{E(B-V)}$	M_B
Na ID	0.052	$^{+0.053}_{-0.025}$	-18.43
Lira Law	0.268	0.043	-19.31
`SNooPy`	0.342	0.031 ± 0.060 (sys)	-19.62
`SNooPy` (no i)	0.445	0.049 ± 0.060 (sys)	-20.04
SALT2	0.347	0.015	-19.64
SALT2 (no i)	0.631	0.019	-20.80
MLCS2k2	0.252	0.0036	-19.25
MLCS2k2 (no i)	0.279	0.0038	-19.36

Table 2.1: Range of extinction values and peak absolute magnitudes computed using different methods and SN Ia fitting programs. SALT2 and MLCS2k2 fits were done using the `sncosmo` package and Lira Law fits were done with a fixed slope, as discussed in the text. We adopt the Na ID extinction value throughout our analysis.

most clearly resolved early optical blue bump, displayed only a moderate excess in the *UVW1*, *UVM2*, or *UVW2* bands compared to what is expected from companion shock interaction models (as shown in Figure 3 of that paper), although its UV colors are still quite blue compared to other normal SNe Ia (Brown et al. 2017).

Different methods of estimating the extinction due to the host galaxy of SN 2019yvq yielded significantly different results, as summarized in Table 2.1. For all fits we fixed $R_{V,\text{host}} = 3.1$.

One method of calculating extinction in SNe Ia is the "Lira Law." As shown in Figure 1 of Phillips et al. (1999), the $B-V$ color evolution of many SNe Ia is similar between 30 and 90 days after V maximum, and can be fit with a line described by Equation 1 of that paper. That expected linear color evolution is shown in pink in Figure 2.3. $E(B-V)$ can then be measured by fitting a line with the same slope to the color data, and finding the linear offset needed to deredden the fit to the expected Lira Law values. Using this method we measure $E(B-V) = 0.268 \pm 0.043$ for SN 2019yvq. However, the $B-V$ color evolution of SN 2019yvq has a best-fit slope 2.9σ away from the slope predicted by the Lira Law. The shallower slope of SN 2019yvq is not unprecedented (see e.g. Förster

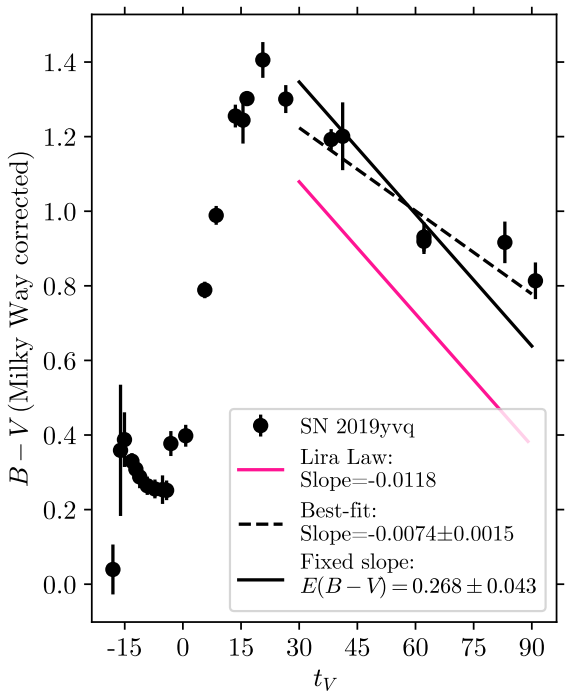

Figure 2.3: Comparisons of the $B-V$ color evolution of SN 2019yvq (black) to the Lira Law (pink). The best-fit line (dashed) to the appropriate SN 2019yvq data has a slope 2.9σ away from the expected slope. Fixing the slope (solid line) is one method of measuring the host extinction, reported in Table 2.1. Following the convention of Phillips et al. (1999), data are plotted relative to t_V (days from V-band maximum).

et al. 2013), but does cast doubt on the $E(B-V)$ value obtained from the Lira Law comparison.

We also attempted to fit the $BVgri$ data from Las Cumbres using the `SNooPy` software package (Burns et al. 2011). We obtained the extinction value by comparing to `EBV_model`, which required a high extinction value (0.342) to match the data. similar to the findings in Miller et al. (2020a). The fits start at a phase of -10 days with respect to maximum light, and thus the early excess should not bias the results. We found that the fits strongly overpredicted the secondary i maximum, so we also performed fits which excluded those data.

In contrast to normal SNe Ia, even other objects with similar relatively high decline

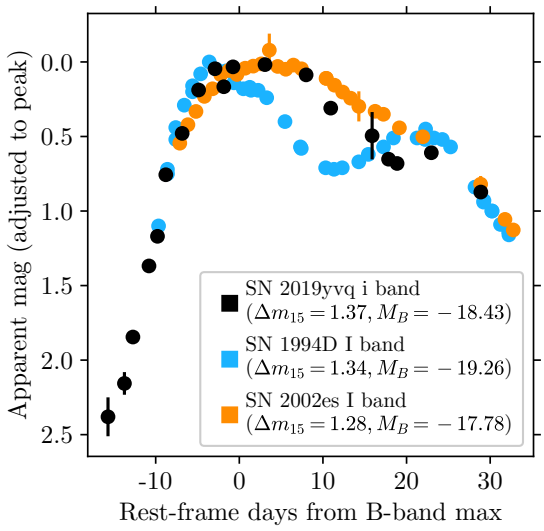

Figure 2.4: NIR lightcurve comparison of SN 2019yvq (black), the normal SN Ia 1994D (pink, chosen for its similar Δm_{15}), and SN 2002es (orange, see Section 2.4). The weak secondary IR maximum of SN 2019yvq is a key piece of evidence that it is intrinsically cool, and therefore red and underluminous. SN 1994D Δm_{15} value from Prieto et al. (2006), M_B from Patat et al. (1996), and data from Richmond et al. (1995). SN 2002es values and data from Ganeshalingam et al. (2012). SNe 1994D and 2002es data accessed via the Open Supernova Catalog.

rates, SN 2019yvq lacks a strong secondary NIR peak, although Tucker et al. (2021) do find evidence of a weak secondary NIR maximum in both the ZTF i-band data and the TESS lightcurve. Figure 2.4 shows the NIR lightcurve of SN 2019yvq compared with both a normal SN Ia with similar Δm_{15} and with SN 2002es, to show that the strength of its secondary NIR maximum is one of several properties which is intermediate between normal SNe Ia and 02es-likes (see Section 2.4). Kasen (2006) argues that secondary NIR maxima in SNe Ia is due to an ionization evolution of iron group elements as the ejecta expands and cools. In light of this, we take the weak secondary NIR maximum of SN 2019yvq as one of several pieces of evidence that the object is intrinsically cool, and therefore red and underluminous compared to normal SNe Ia (Section 2.4). We repeated this process on the $UBVgri$ Las Cumbres data using the SALT2 (Guy et al. 2007) and

Filter	$\mathrm{MJD}_{\mathrm{max}}$	m_{max}	M_{max}	Δm_{15}
U	$58861.042^{+0.548}_{-0.502}$	$15.008^{+0.083}_{-0.082}$	$-18.47^{+0.19}_{-0.29}$	$1.579^{+0.150}_{-0.147}$
B	$58862.805^{+0.310}_{-0.305}$	$14.996^{+0.026}_{-0.025}$	$-18.43^{+0.15}_{-0.24}$	$1.374^{+0.081}_{-0.078}$
g	$58863.105^{+0.251}_{-0.259}$	14.880 ± 0.017	$-18.52^{+0.15}_{-0.23}$	1.430 ± 0.060
V	$58864.840^{+0.521}_{-0.576}$	$14.622^{+0.033}_{-0.032}$	$-18.73^{+0.14}_{-0.20}$	$0.803^{+0.103}_{-0.109}$
r	$58864.137^{+0.519}_{-0.530}$	14.626 ± 0.037	$-18.69^{+0.13}_{-0.18}$	$0.806^{+0.071}_{-0.073}$
i	$58863.274^{+0.851}_{-0.818}$	15.028 ± 0.039	$-18.24^{+0.13}_{-0.15}$	$0.434^{+0.119}_{-0.125}$

Table 2.2: Lightcurve parameters of SN 2019yvq, modeled after Table 4 of Ganeshalingam et al. (2012). Absolute magnitudes have been dereddened, apparent magnitudes have not.

MLCS2k2 (Jha et al. 2007) fitting packages, accessed through SNCosmo (Barbary et al. 2016) with an added `CCM89Dust` component to measure $E(B-V)$. We exclude the first three epochs of data, to reduce biases from attempting to fit the early blue excess. The fits were generally poor: in order to achieve a $\chi^2_{\mathrm{reduced}}$ of less than 2 on the best fits (MLCS2k2, no i band), we required a systematic error of more than three times the average flux error to be added in quadrature at each point. In general the fits again overpredicted the secondary i-band peak. Values for the `SNooPy` and SNCosmo fits are reported in Table 2.1.

The fact that different methods of estimating $E(B-V)$ led to such a wide range of extinction values, and the fact that methods which relied on fitting to SN Ia templates resulted in generally poor fits, led us to conclude that SN 2019yvq is an inherently peculiar SN Ia. We therefore adopt the extinction value obtained from fitting the Na ID lines, $E(B-V) = 0.052^{+0.053}_{-0.025}$ (see Section 2.3.2 for methodology). This value, while significantly lower than other possible values, results in an underluminous peak absolute magnitude, which is consistent with SN 2019yvq's weak secondary IR maximum and high lightcurve decline rate. Additionally, it is consistent with the value calculated in Miller et al. (2020a) ($E(B-V)_{\mathrm{host}} \approx 0.032$), which they derive using the same method, but a different spectrum. Siebert et al. (2020) and Tucker et al. (2021) adopt this value

from Miller et al. (2020a), so our extinction value is also consistent with all previously published work on SN 2019yvq.

We fit a fourth-order polynomial to the near-peak (-10 to $+20$ days) data to obtain standard lightcurve parameters. These parameters are summarized in Table 2.2. We note that the value of $\Delta m_{15}(B)$ is lower than the value inferred by Miller et al. (2020a) from the g lightcurve and used in Siebert et al. (2020) ($\Delta m_{15}(B) \gtrsim 1.6$).

The color evolution of SN 2019yvq is presented in Figure 2.5. The *Swift* data for all objects were extinction-corrected using the method of Brown et al. (2010) (Table 1). We note that SN 2019yvq becomes rapidly redder in all optical colors (besides $r-i$) over the first five days. In $(B-V)$ and $(g-r)$ especially, it is much redder than typical SNe Ia such as SN 2011fe (data from Zhang et al. 2016) and more closely mirrors the evolution of iPTF14atg. iPTF14atg was also an underluminous SN Ia with a strong early UV excess (Cao et al. 2015), and belonged to the 02es-like subclass, whose namesake is described in Ganeshalingam et al. (2012). As discussed in Section 2.4, we classify SN 2019yvq as a transitional 02es-like.

In terms of *Swift* UV colors, SN 2019yvq stands out even more compared to typical SNe Ia, and is $\gtrsim$1 magnitude bluer than SN 2017cbv in $(UVW1-U)$ at $\sim$5 days after the estimated explosion time. This extreme UV color and subsequent evolution is again most similar to iPTF14atg within ten days of explosion.

Based on the lightcurve parameters, we can begin to put SN 2019yvq in context with other SNe Ia, especially those with early light curve data as well. In the left panel of Figure 2.6, we show the M_B versus $\Delta m_{15}(B)$ relation of Phillips (1993), populated with a large sample of nearby SNe Ia (see Figure 14 from Parrent et al. 2014, with original data from Blondin et al. 2012; Folatelli et al. 2012; Pakmor et al. 2013). When we include the "blue" and "red" sample of early SN Ia of Stritzinger et al. (2018) (hereafter S18), we see the tendency of early blue objects to be slower declining and slightly brighter than the

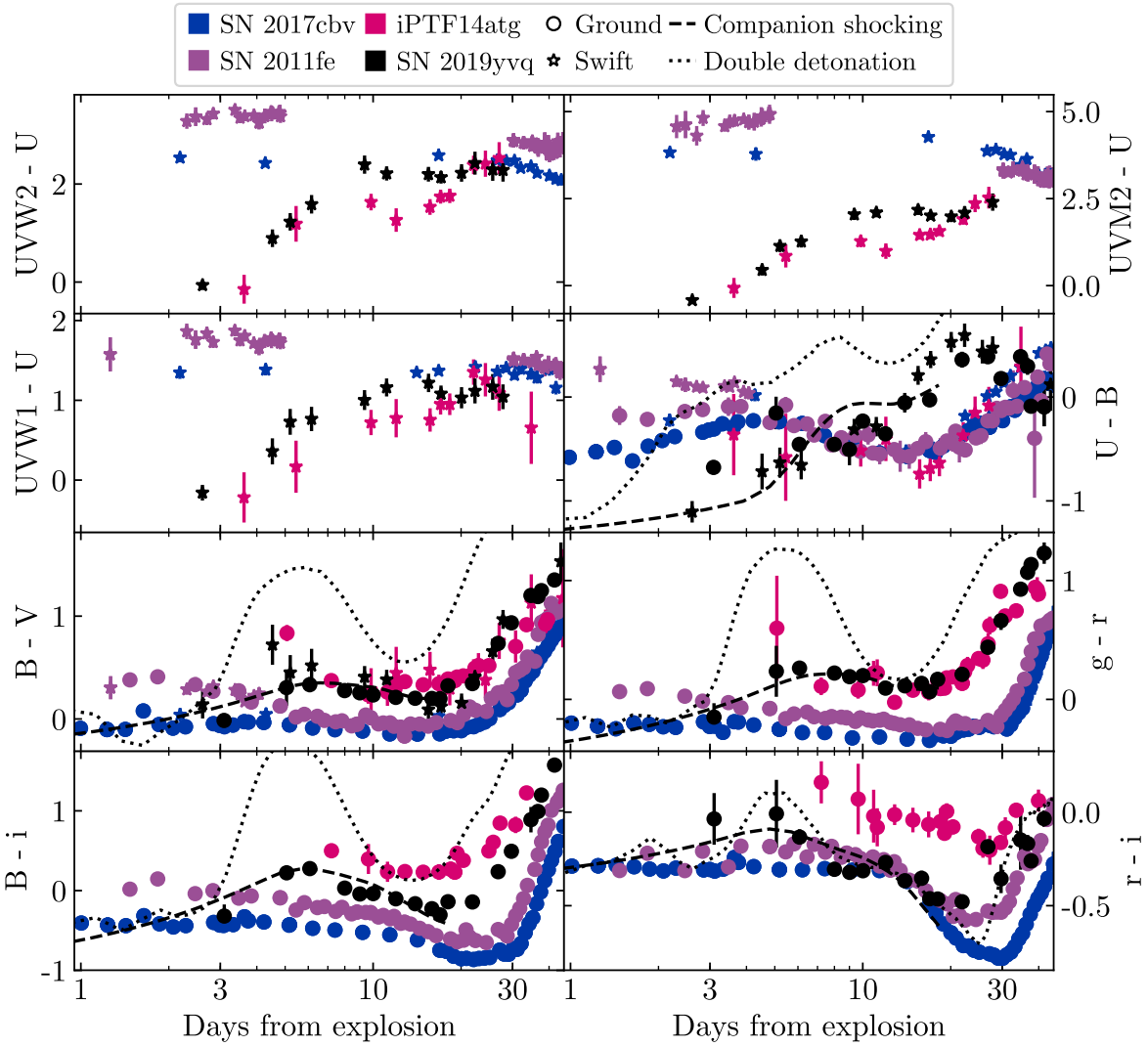

Figure 2.5: Color evolution of SN 2019yvq (black) compared with other SNe Ia. SN 2011fe (purple) is included to represent typical SNe Ia color evolution, and demonstrates that SN 2019yvq was both blue at early times (especially in UV colors) and red at peak (especially in $B-V$ and $g-r$) compared to normal SNe Ia. We assume an explosion epoch of SN 2019yvq derived from the best-fit companion shocking model, and the two sets of model colors plotted are the best-fit models described in Section 2.5.

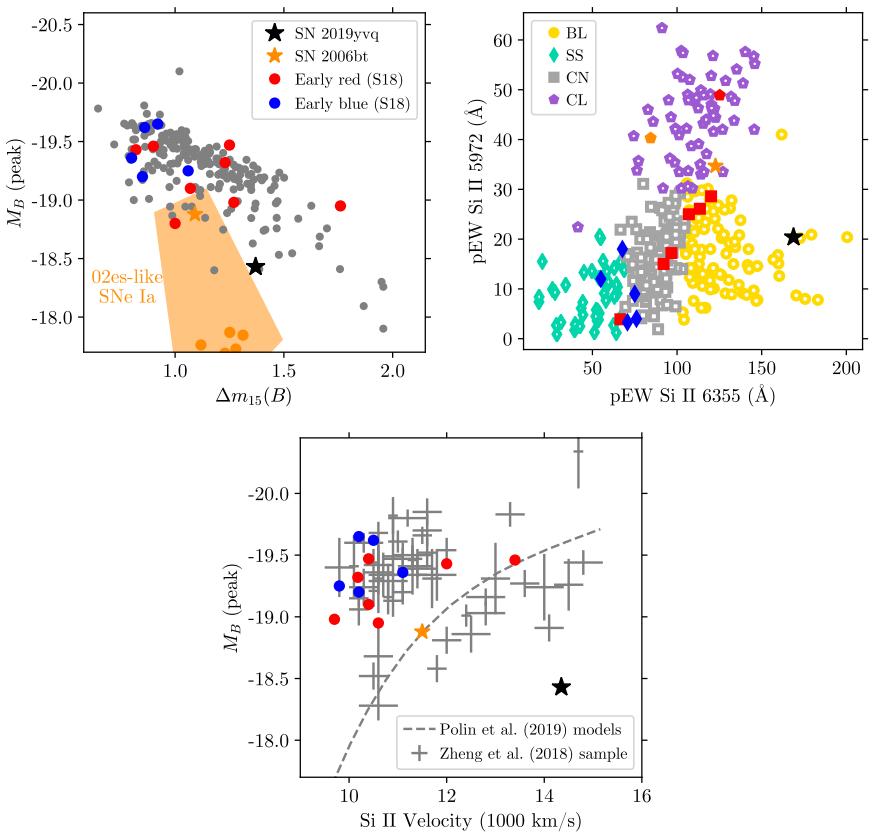

Figure 2.6: Demographic properties of SN 2019yvq (black star in each plot). We note that SN 2019yvq is at the edge of normal parameter space in several respects, and is well-separated from the early blue objects of S18. It is instead closer to (although still substantially different from) the transitional 02es-like SN 2006bt (orange star in each plot). *Left*: Luminosity decline rate relation for SNe Ia, with the gray background points coming from the union of samples presented by several groups (Blondin et al. 2012; Folatelli et al. 2012). The orange polygon and data points replicate the sample of 02es-like SNe Ia in Taubenberger (2017), with the transitional SN 2006bt represented by the orange star in each plot. In blue and red we show the early SN Ia sample presented by S18, split by their early light curve colors. Out of the S18 sample, we have adjusted the absolute magnitude of SN 2017cbv to match the distance of $D = 12.3$ Mpc found in Sand et al. (2018). *Center*: The location of SN 2019yvq (black star) in the Branch diagram (Branch et al. 2006), which groups SNe Ia as broad line (BL), shallow silicon (SS), core normal (CN), or cool (CL) based on the pseudo-equivalent widths of two Si II features. The background sample is the same as the left panel, and the only other 02es-like (in orange) in Blondin et al. (2012) is SN 2002es itself. *Right*: A replica of the plot from Polin et al. (2019) comparing 0.01 $M_\odot$ He shell double detonation models to a sample of SNe Ia from Zheng et al. (2018), with velocities measured at peak. The prototype object SN 2002es has a Si II velocity which is too low (5890 km s^{-1}) to fit in the axis range of these plots.

red sample. SN 2019yvq notably stands out from the "early-blue" sample with its much higher decline-rate. In this parameter space it is closer to another transitional 02es-like, SN 2006bt (the orange star in Figure 2.6), although still well-separated from that object.

2.3.2 Spectral Analysis

We show the spectral evolution of SN 2019yvq in Figure 2.2, from roughly −14 to +117 days with respect to B-band maximum. Using the Supernova IDentification software package (`SNID`; Blondin & Tonry 2007) on the FLOYDS spectrum taken at +1.8 d with respect to B-band maximum we find that all reasonable matches correspond to normal SN Ia. In particular, the spectrum is well matched to SN 2002bo near maximum light except in the region of ∼4000–4500 Å, which we attribute to weak Ti II absorption and discuss further in Section 2.4. We note that the initial spectrum of SN 2019yvq shows faint Hβ, Hα, and [N II] emission; upon investigation, we believe this emission is from the host galaxy due to slight mis-centering of the SN within the slit.

Velocities and Spectral Classification

We measure a Si II λ6355 velocity of 14,400 km s^{-1} near maximum light, as well as pseudo-equivalent width (peW) values of 169 Å and 20 Å for the Si II λ6355 and λ5972 features, respectively, from the +1.8d FLOYDS spectrum (these measurements, and those that follow, are in broad agreement with those of Miller et al. 2020a). Here SN 2019yvq is clearly a high-velocity (HV) object in the Wang et al. (2009) classification scheme (e.g. objects with Si II λ6355 $\gtrsim$11,800 km s^{-1} near max). To put SN 2019yvq in the context of the standard Branch classification scheme (Branch et al. 2006), we plot it along with a larger sample of SNe Ia (Blondin et al. 2012) in the center panel of Figure 2.6. Here SN 2019yvq is clearly a Broad Lined (BL) SN Ia, with a very deep

and broad Si II λ6355 feature. This is consistent with its match to SN 2002bo, which was another BL event. We also plot the blue and red sample from S18 on the Branch diagram, and note that SN 2019yvq again stands alone among the early blue objects as a broad lined event, as most of the others are Shallow Silicon or Core Normals, and instead it is closer to the transitional 02es-like SN 2006bt.

To explore the demographic place of SN 2019yvq further, we plot the Si II λ6355 velocity near maximum light versus the absolute B-band magnitude in the right panel of Figure 2.6. This plot is largely a reproduction of Figure 11 in Polin et al. (2019), with the grey data points originating from the SNe Ia sample of Zheng et al. (2018); the blue and red sample of S18 and SN 2006bt are plotted as well. As discussed by Polin et al. (2019), two groups of SNe Ia are apparent in the plot: one that is tightly clumped at $v \approx 10,500$ km s^{-1} and $M_B \approx -19.4$ and is attributed to Chandrasekhar mass explosions, and a second group that follows a relationship between luminosity and velocity, roughly tracking expectations from the sub-Chandrasekhar class of explosions, as illustrated by the dashed line which depicts a set of 0.01 $M_\odot$ He shell double detonation models. It is clear that SN 2019yvq is not well-matched by either population, and a model with different He shell mass is needed to replicate its position, as is found in Section 2.5.2.

Search for Unburned Carbon

The presence of unburned carbon in SN Ia spectra is potentially a powerful discriminant between explosion models. Chandrasekhar-mass delayed detonation explosions predict complete carbon burning for normal-bright SNe Ia (e.g. Kasen et al. 2009), and increasing amounts of unburned carbon for fainter SNe Ia (e.g. Höflich et al. 2002). In the explosions of sub-Chandrasekhar mass white dwarfs, on the other hand, the initial surface detonation may leave little or no detectable carbon (e.g. Fink et al. 2010; Polin et al. 2019).

The most commonly searched for carbon feature is C II λ6580Å, which can be difficult to detect both because it fades quickly after explosion and is near the strong Si II λ6355Å absorption line. Large spectroscopic samples have found that ∼20-30% of early time SNe Ia data have C II signatures, with the chances of detection increasing the earlier the data were taken (Thomas et al. 2011; Parrent et al. 2011; Folatelli et al. 2012; Silverman & Filippenko 2012; Wyatt et al. 2021). Interestingly, several of the SN Ia with early light curve excesses have also displayed strong early carbon, including SN 2017cbv (Hosseinzadeh et al. 2017), iPTF16abc (Miller et al. 2018) and SN2018oh (Li et al. 2019).

We have closely inspected all of our SN 2019yvq optical spectra through maximum light at the expected position of C II λ6580 Å, near the red shoulder of the Si II λ6355 Å absorption line. No C II feature is apparent, and our earliest data do not show the strong carbon absorption seen in SN 2017cbv and iPTF16abc, although the signal to noise of our early data is not good enough to make definitive claims on any weak C II feature. We have further inspected our IRTF spectrum taken at +6 d with respect to B-band maximum, as it has been suggested that the C I λ1.0693 μm line is a good tracer of unburned carbon. No C I line is apparent, but this spectrum is later than ideal since this feature is most visible around maximum light (e.g. Hsiao et al. 2013, 2019). Detailed modeling is necessary to completely rule out any subtle carbon feature, but this is beyond the scope of the current work.

In conclusion, we can make no definitive claim about the presence of either C II λ6580 Å or C I λ1.0693 μm, partially due to low signal to noise data, although we can rule out the strong carbon seen in previous SNe Ia with blue light curve excesses. This lack of strong carbon is in broad agreement with expectations from sub-Chandrasekhar helium shell detonation models (e.g. Polin et al. 2019), which we explore further in our model comparisons below.

Medium Resolution Spectra and Na ID

The Na ID doublet is often used to estimate host galaxy extinction in nearby SNe (e.g. Poznanski et al. 2012), although the correlation between host extinction and Na ID equivalent width has a large scatter (e.g. Galbany et al. 2019). Although the diffuse interstellar band at 5780Å has been shown to be a superior tracer of host extinction (Phillips et al. 2013), we do not detect the line in our medium resolution Bok spectrum. The Na ID doublet at the redshift of SN2019yvq's host (z=0.00908) is clearly visible in our medium resolution Bok B&C spectrum (R≈3400) taken on 2020 January 29 UT (a medium resolution MMT Blue Channel spectrum taken on 2020 February 18 does not have sufficient signal to detect the doublet), and we measure 0.28Å and 0.18Å for the equivalent width of the D1 and D2 lines, respectively. Using the correlation found by Poznanski et al. (2012), this translates to an expected host extinction of $E(B-V)_{\text{host, Na ID}} = 0.052^{+0.053}_{-0.025}$ mag. As discussed in Section 2.3.1, this is the host extinction value we use throughout the paper.

Nebular spectra of SN 2019yvq

The nebular spectra of SNe Ia can provide an independent way to differentiate between progenitor systems, since different progenitors and explosion channels should have different nebular signatures.

The violent merger of two WDs should result in nebular [O I] due to its ejection at low velocities (Pakmor et al. 2012), although this has only been seen in the nebular spectra of the 02es-like SN 2010lp (Taubenberger et al. 2013) and is not present in the nebular spectra of SN 2019yvq.

The double-detonation scenario should only partially burn the core, leaving strong Ca signatures (Polin et al. 2021). SN 2019yvq does display nebular [Ca II] which is

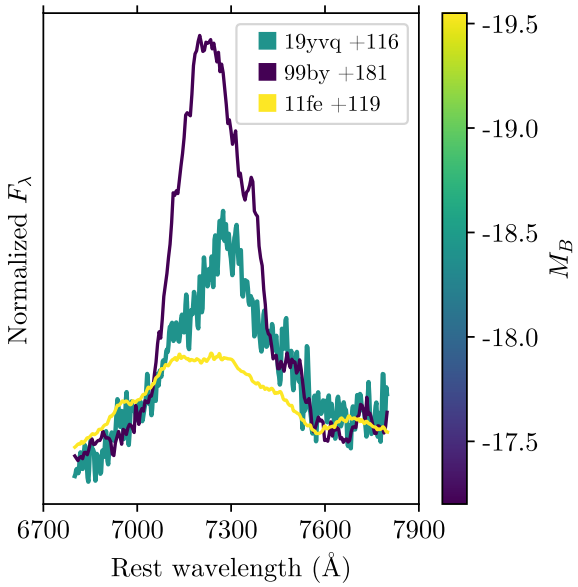

Figure 2.7: Nebular spectra of SNe Ia focusing on the [Ca II], [Fe II], [Ni II] line complex. This feature is strongest in the nebular spectra of underluminous SNe Ia, and is the subject of thorough modeling in Siebert et al. (2020) for a +153d Keck spectrum of SN 2019yvq. The legend displays the shortened SN name (e.g. SN2019yvq $\rightarrow$ 19yvq) and the epoch in days after B maximum. Spectra have been normalized to have identical mean fluxes over their full wavelength range ($\sim$3500–10000 Å). SN 2019yvq lies in between normal SNe Ia (represented by SN 2011fe) and low-luminosity SNe Ia (represented by the 91bg-like SN 1999by).

intermediate in strength between typical- and low-luminosity SNe Ia, as shown in Figure 2.7.

Lastly, the companion interaction scenario should produce H and He emission from the swept-up material (Botyánszki et al. 2018; Dessart et al. 2020), although this is seen in an extremely limited number of cases (Kollmeier et al. 2019; Prieto et al. 2020). We use the nebular spectra of SN 2019yvq to measure limits on the luminosity and mass of swept-up H and He, following the methodology of Sand et al. (2019) and references therein. To briefly summarize, we first smooth the spectrum on a scale much larger than the expected width of an Hα feature. We then subtract off the smoothed spectrum and search for any excess flux in the residuals, assuming an expected width of FWHM $\approx$ 1000 km s^{-1} (22 Å) for the line width and a potential offset from the rest wavelength of up to $\sim$1000 km s^{-1} as well. Following Equation 1 from Botyánszki et al. (2018), we then estimate the mass of the stripped material, after predicting the luminosity of SN 2019yvq at +200 days. For the nebular spectrum taken +106 days past maximum, $M_{\rm H} < 1.6 \times 10^{-3} {\rm M}_{\odot}$ and $M_{\rm He} < 2.0 \times 10^{-2} {\rm M}_{\odot}$ (using the He I λ6678 line). Using an additional nebular spectrum taken +117 days past maximum, $M_{\rm H} < 1.7 \times 10^{-3} {\rm M}_{\odot}$ and $M_{\rm He} < 2.1 \times 10^{-2} {\rm M}_{\odot}$. With access to a higher signal-to-noise spectrum, Siebert et al. (2020) place even stricter limits on the amount of swept-up He and He: $M_{\rm H} < 2.8 \times 10^{-4} {\rm M}_{\odot}$ and $M_{\rm He} < 2.4 \times 10^{-4} {\rm M}_{\odot}$.

The combination of the presence of [Ca II] and a lack of narrow hydrogen emission is consistent with a double-detonation progenitor system, which is what is inferred by Siebert et al. (2020). Despite these limits, we cannot unequivocally claim that SN 2019yvq is a double detonation event due to discrepancies in best-fit models of photospheric photometry and nebular spectroscopy. Our conclusion in this regard is in agreement with Tucker et al. (2021) and Miller et al. (2020a), and is discussed in more detail in Section 2.5.2.

Parameter	02es-like SNe Ia	SN 2019yvq	SN Ia-norm
M_B	-17.6 – -18.1	-18.43	-18.5 – -19.7[1]
$\Delta m_{15}(B)$	1.1 – 1.3	1.37	0.8 – 1.4[1]
Rise time (days)	19 – 20	18.7	17.1 – 20.7[2]
$(B-V)_{\rm max}$	0.2 – 0.5	0.22	-0.1 – 0.1[1]
Secondary IR maximum	Weak	Weak	Yes
$v_{\rm Si\ II}$ (km s^{-1})	6000 – 10000	14400	10000 – 12600[3]
Ti II at peak	Yes	Intermediate	No[4]
nebular [Fe II] and [Ca II]	Yes	Intermediate	Weak[5]

Table 2.3: Comparisons between SN 2019yvq and 02es-like SNe Ia. Parameter ranges for 02es-like SNe Ia are taken from Taubenberger (2017) and are intended to be approximate, reflecting the small sample size and diversity of this subclass. Sources for SN Ia-norm values: 1: Table 4 of Ashall et al. (2016); 2: Table 4 of Miller et al. (2020b); 3: Calculated from the Zheng et al. (2018) sample; 4: Nugent et al. (1995); 5: Siebert et al. (2020).

2.4 Comparisons to SN 2002es

SN 2019yvq shares some characteristics with 02es-like SNe Ia, and could be considered an 02es-like depending on how broad a definition of that subclass is taken. We classify it as a transitional 02es-like. Although this term has not previously been used in the literature to describe any objects, it accurately reflects the nature of SN 2019yvq. Table 2.3 summarizes various photometric and spectroscopic signatures of both 02es-like SNe Ia, taken from Taubenberger (2017), and normal SNe Ia, (see caption for sources). See Ganeshalingam et al. (2012) for a study of the eponymous SN 2002es, and Taubenberger (2017) and White et al. (2015) for reviews of this subclass.

SN 2019yvq is at the edge of what could be considered 02es-like in several respects. Its peak brightness and lightcurve width are on the edge of the class, as seen in the left panel of Figure 2.6. Like 02es-like SNe Ia, SN 2019yvq also displays an almost nonexistent secondary IR maximum and red colors after its initial blue excess (see Figure 2.5 and its similarity to the 02es-like iPTF14atg).

Spectroscopically there are both similarities and obvious differences, as highlighted

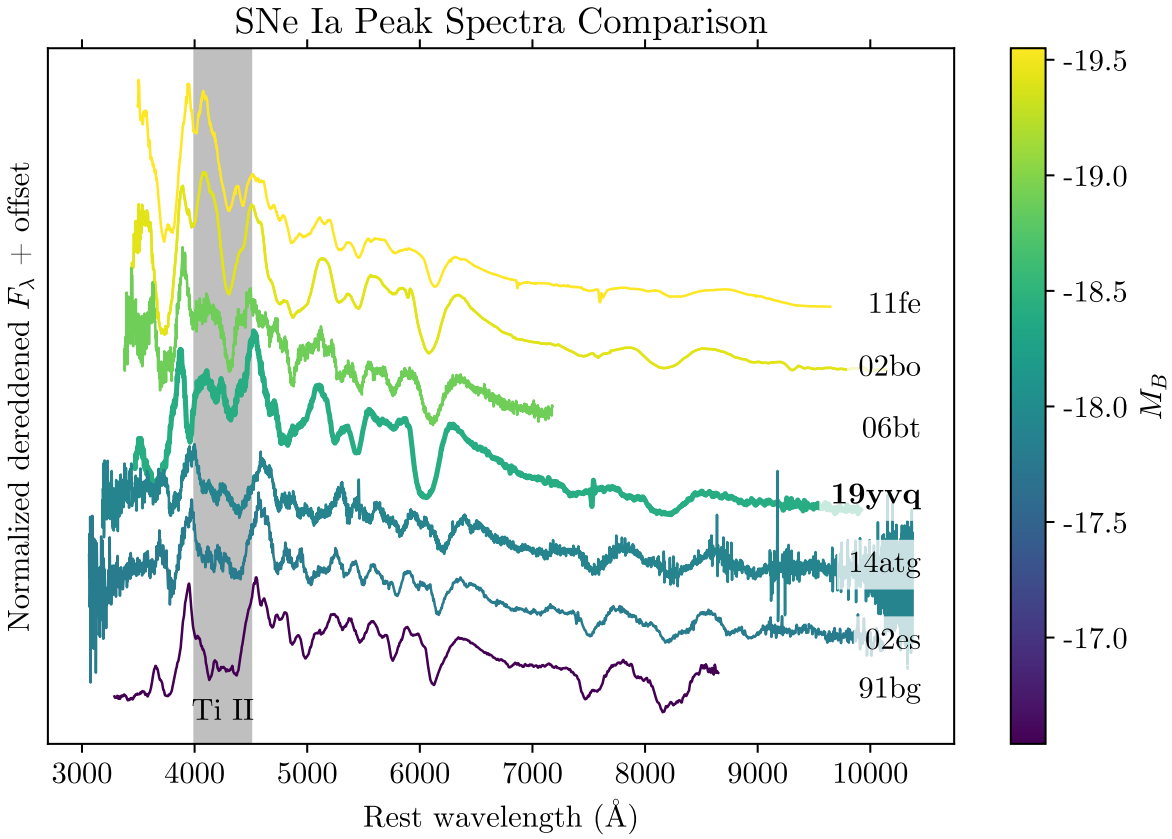

Figure 2.8: Comparisons of SNe Ia peak spectra over a wide range of luminosities. Although the spectrum of SN 2019yvq is quite similar to SN 2002bo (a more typical luminosity SN Ia), its primary difference is in the ∼4000–4500 Å region. This coincides with the "titanium trough" present in lower luminosity SNe Ia, and SN 2019yvq's extra absorption in this wavelength region supports the interpretation of it as an underluminous SN Ia despite obvious differences when comparing to the spectrum of SN 2002es. The combination of low temperature and luminosity with broad high-velocity Si II is rarely seen in SNe Ia and is difficult to reproduce in models.

in Figure 2.8. The peak spectrum of SN 2019yvq is most similar to SN 2002bo, which also displayed deep Si II 6355 and had a similar Si II line ratio. SN 2002bo had a more typical peak luminosity for SNe Ia ($M_B = -19.41$, Benetti et al. 2004). SN 2019yvq's Si II velocity and line ratio make it an outlier compared to other 02es-like SNe Ia, since these spectral features would normally indicate an energetic and luminous event. Figure 2.8 also includes for comparison SN 2006bt, which displayed Si II 6355 which

was higher-velocity and broader than typical SNe Ia, but weaker and lower-velocity than SN 2019yvq. We would also classify SN 2006bt as a transitional 02es-like (in agreement with Taubenberger 2017), and we refer to Foley et al. (2010) for a thorough study of this unusual object.

02es-like SNe Ia are also characterized by Ti II at peak, which is seen in lower luminosity SNe Ia like SN 1991bg (see Figure 2.8). We note that the spectra of SN 2019yvq and SN 2002bo are quite dissimilar bluewards of ∼4500 Å, which is precisely at one end of the Ti II "trough". Ti II and V II are efficient at suppressing blue flux in SNe Ia, and we refer to Figure 11 of Cartier et al. (2017) to demonstrate their effects on SNe Ia spectra. In the wavelength regime of the Ti trough, SN 2019yvq is again intermediate between typical-luminosity SNe Ia (SN 2011fe, SN 2002bo) and low-luminosity SNe Ia (SN 2002es, SN 1991bg). We take SN 2019yvq's suppressed blue flux as tentative evidence for it having Ti, albeit weaker than the more extreme case of SN 1991bg.

Strong [Ca II] and [Fe II] emission is also seen in the nebular spectra of sub-luminous SNe Ia, such as the 02es-like SN 2010lp (Taubenberger et al. 2013). As already discussed in Section 2.3.2 and shown in Figure 2.7, SN 2019yvq displays nebular [Ca II] emission which is intermediate between low-luminosity and normal-luminosity SNe Ia, again placing it in a transitional region of parameter space.

To summarize, SN 2019yvq displays a surprising mix of attributes. Its red peak color and weak secondary IR maximum are in line with what is expected of 02es-like SNe Ia. Its peak brightness and decline rate are unusual for normal SN Ia, and, while not identical to other 02es-likes, fit the general paradigm of underluminous and moderately quickly declining. Specific spectral features (peak Ti II, nebular [Fe II] and [Ca II]) are intermediate between normal and 02es-like SNe Ia. Lastly, its Si II velocity sets it well apart from 02es-likes, and is unusually high even for normal SNe Ia. Due to this mix of attributes, with some matching 02es-like values, some (its velocity) being outliers for the

02es-like SN	Host type	Earliest epoch (days)	Filter	Early excess?
SN 2019yvq[1]	SAB0	-15.8	Swift	Yes
iPTF14atg[2]	E-S0	-15.5	Swift	Yes
iPTF14dpk[3]	Starburst	-16.3	R	Maybe
PTF10acdh[4]	···	-14.5	R	Unknown
PTF10ujn[4]	···	-10.7	R	Unknown
PTF10bvr[4]	E	??	R	Unknown
SN 2002es[5]	S0	-7.3	B	Unknown
SN 1999bh[6]	Sb	0.6	B	Unknown
SN 2006bt[6,7]	S0/a	-2.6	B	Unknown
PTF10ops[6,8]	SAa?	-6.6	B	Unknown
SN 2010lp[6]	SAb	-7	B	Unknown

Table 2.4: A literature sample of known 02es-like SNe Ia. iPTF14atg is the only other 02es-like observed in blue filters as early as SN 2019yvq, and it also displays a UV excess. iPTF14dpk displayed a sharp rise from its last non-detection, and its first detection is high relative to a power law rise. PTF10ops is either ∼148 kpc offset from the spiral galaxy SDSS J214737.86+055309.3, or in a very faint satellite galaxy of it. Sources: 1: this work; 2: Cao et al. (2015); 3: Cao et al. (2016); 4: White et al. (2015); 5: Ganeshalingam et al. (2012); 6: Taubenberger (2017); 7: Foley et al. (2010); 8: Maguire et al. (2011).

subclass, and many others in between 02es-like and normal SNe Ia, we classify it as a "transitional" 02es-like SN Ia.

To be explicit, we are using the word "transitional" in a strictly phenomenological sense, and not claiming any specific "transition" between the physics or progenitor systems of normal and 02es-like SNe Ia. As discussed in Section 2.1 there is considerable uncertainty about the progenitor systems of all SNe Ia, which would make any such claim difficult to quantitatively substantiate.

Table 2.4 lists all known 02es-like SNe Ia, including SN 2019yvq. The three SNe which were detected the earliest all display unusual lightcurve properties. iPTF14atg (Cao et al. 2015) has already been discussed as a prime example of an early UV excess. The early lightcurve of iPTF14dpk (Cao et al. 2016) differed from iPTF14atg, as it rose

more than 1.8 magnitudes/day between its last non-detection and earliest detection (in R, the only observed band at that epoch). Cao et al. (2016) take this as evidence of a dark phase, a time period after the explosion where the energy generated by radioactive decay has not yet reached the photosphere (i.e. the explosion has occurred but is not yet visible). The lightcurve also declined between the first and second epochs, although Cao et al. (2016) attribute this to scatter consistent with the errors and not a physical dimming. The paper concludes that the lightcurve of iPTF14dpk is consistent with the ejecta-companion interaction scenario but seen from an unfavorable viewing angle.

The fact that the three 02es-like SNe Ia which have the earliest observations all display extremely unusual, but consistent, lightcurve properties could be evidence that they all arise from identical progenitor systems, but the sample of such well-observed events will need to be expanded beyond its current limited numbers to make this statement with statistical confidence. But even with the small sample size we can say that the companion-ejecta interaction models, which predict a strong UV excess $\sim$10% of the time due to viewing angle constraints, are unlikely to be the source of 02es-like SNe Ia if two of the three SNe observed at the right epochs display such an excess with certainty, and the third displays a potential weak excess. We discuss these implications more in Section 2.6.

2.5 Model Comparisons

We compare our UV and optical data of SN 2019yvq to two main classes of models which are capable of producing early blue bumps: companion shocking models from Kasen (2010) and double detonation sub-Chandrasekhar mass models from Polin et al. (2019). Our best-fit models in these two categories are included in Figure 2.9. We also discuss comparisons to models with varying Ni distributions, and we use radio upper

limits to place further constraints on circumstellar interaction in the progenitor system. No one model reproduces all features of the dataset, so we discuss their benefits and shortcomings.

2.5.1 Companion Shocking

As discussed in the introduction, Kasen (2010) predicted that an early blue/UV excess could be seen in the lightcurves of SNe Ia when the ejecta collide with a nondegenerate companion and gets shock-heated. This excess arising from companion shocking would only be visible within a few days of the explosion, and would only be seen for ∼10% of SNe Ia due to viewing angle effects.

Hosseinzadeh et al. (2017) previously used these models to fit the lightcurve of SN 2017cbv. As described in that paper, they require a total of eight parameters to generate fits: (1) the explosion epoch t_0, (2) the companion separation a, (3) a factor involving the ejecta mass and speed ($x \propto Mv^7$), (4) the time of maximum $t_{\rm max}$, (5) the lightcurve stretch s, (6) and (7) factors on the r and i flux of the SiFTO template (Conley et al. 2008) r_r and r_i, and (8) a factor on the U shock flux r_U.

We make use of `lightcurve_fitting` (Hosseinzadeh 2019) to fit these models, which uses a Markov Chain Monte Carlo routine based on the `emcee` package (Foreman-Mackey et al. 2013) to generate fits. The models consist of two components: a blackbody flux component and a SiFTO template which can be stretched and scaled. We extend the blackbody component of the model to include the early *UVW2*, *UVM2*, and *UVW1 Swift* data, since the first two epochs were taken in a regime where the SN flux was dominated by the early excess.

Fits struggled to converge until the following steps were taken: (1) we put a tight prior on the explosion epoch and enforced adherence to the non-detection from Itagaki

	SN 2019yvq	SN 2017cbv
t_0 (MJD)	58844.3±0.1	57821.9
a ($R_\odot$)	52^{+6}_{-4}	56
$\frac{M}{M_{Ch}}\left(\frac{v}{10000\ \mathrm{km\ s^{-1}}}\right)^7$	0.099 ± 0.03	3.84 ± 0.19
t_{max} (MJD)	58863.14 ± 0.08	57840.2
s	0.878 ± 0.007	1.04
r_r	0.920 ± 0.006	0.95
r_i	$0.736^{+0.006}_{-0.007}$	0.85
r_U	1.27 ± 0.04	0.61

Table 2.5: Comparisons between the best-fit parameters of the Kasen (2010) companion shocking models for SN 2019yvq (this work) and SN 2017cbv (Hosseinzadeh et al. 2017). Parameters: time of explosion (t_0), companion separation (a), a parameter involving the ejecta mass and velocity ($\propto Mv^7$), time of peak (t_{max}), lightcurve stretch (s), factors on the r and i flux in the SiFTO template (r_r, r_i), and a flux factor on the U though $UVW2$ shock flux (r_U).

Astronomical Observatory, and (2) we extended the multiplicative factor on the U shock flux to include *Swift* data due to the strength of the excess in those bands as well. The parameters for our best-fit model are listed in Table 2.5, along with the corresponding best-fit model for SN 2017cbv from Hosseinzadeh et al. (2017).

The most significant of these is the r_U factor: Hosseinzadeh et al. (2017) find that the U shock flux for models describing SN 2017cbv must be scaled by a factor of 0.61. There are several possible explanations for this, including assumptions of spherical symmetry and blackbody SEDs, or the effects of line blanketing from iron group elements (IGEs) causing the UV/blue flux to be overestimated.

However, we do *not* find that the U (and $UVW1$, $UVM2$, $UVW2$) shock flux needs to be scaled down to match the data. Instead the best-fit model has a UV flux enhancement of about 27%. An increase of this amount is unsurprising: the analytic expressions for the blackbody luminosity used in `lightcurve_fitting` and derived from Kasen (2010) replicate the numerical models of companion-ejecta interaction seen at a viewing angle of approximately 30° (see Figure 2 of that paper). Explosions with smaller viewing angles

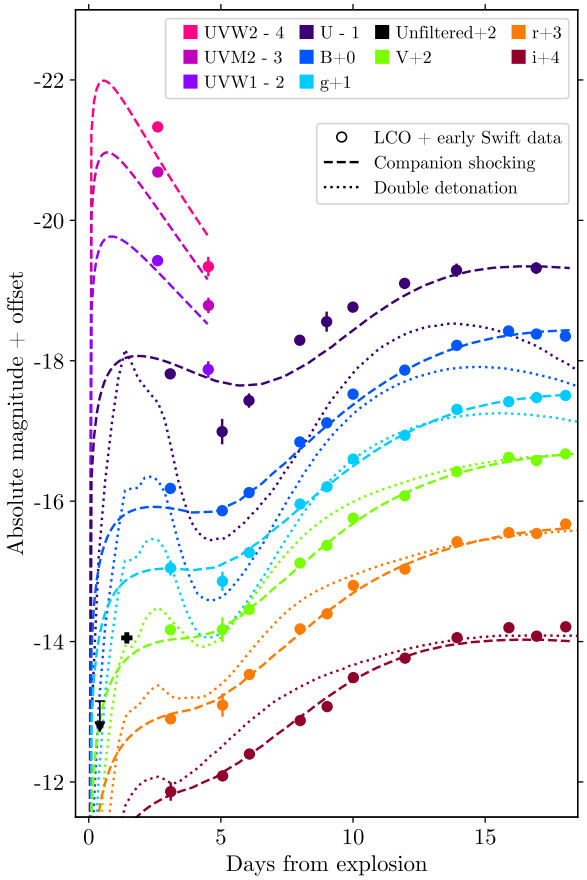

Figure 2.9: Comparisons between the Las Cumbres and early *Swift* data for SN 2019yvq and two different models. The non-detection and first detection from Itagaki are included in black. Shown in the dashed line is the best-fit companion shocking model from Kasen (2010). The parameters for this model are in Table 2.5 (see Section 2.5.1 for more detail). The SN template used to generate the companion shocking model did not extend into the mid-UV, so only the blackbody flux component is shown for the *Swift* filters. The dotted line is the best-fit double detonation model from Polin et al. (2019): a 0.95 $M_{\odot}$ WD progenitor with 0.055 $M_{\odot}$ of He (see Section 2.5.2 for more detail).

result in higher observed luminosities, up to about 0.25 dex (a factor of 1.8) brighter for a perfectly aligned scenario. Although our model does not include the viewing angle as a parameter, better-aligned explosions can generate the required shock flux enhancement.

The other notably discrepant parameter between the two fits is the parameter involving mass and velocity. It is worth noting that the relevant velocity is not exactly the ejecta velocity, rather it is the transition velocity between different power laws in the density profile for the modeled ejecta. Assuming M_{Ch} of ejecta, the value of this parameter for SN 2017cbv corresponds to a velocity of about 12000 km s^{-1}. Using the same assumption, the value for SN 2019yvq corresponds to a transition velocity of about 7000 km s^{-1}.

The best-fit companion separation (52 $R_\odot$) lies towards the extreme of the expected distribution for main sequence donor stars, based on binary population synthesis models (Liu et al. 2015). Assuming Roche lobe overflow (Eggleton 1983), this separation implies a companion radius of $\sim$20 $R_\odot$. This stellar radius excludes most main sequence stars but not more evolved stars, which can also donate additional mass via their high winds (in some cases higher than $10^{-5} M_\odot$ yr^{-1}; Beasor et al. 2020).

Miller et al. (2020a) also use the Kasen (2010) models to fit their data, although with a different methodology. They fit only shock-dominated data (within $\sim$3.5 days of explosion) and use a slightly different analytical form for the shock flux. They find a best-fit companion separation of 13 ± 1 $R_\odot$ and an explosion date of 58845.82 ± 0.04 (MJD). This companion separation is several times smaller than our best-fit value (Table 2.5), and the explosion date is more than 1.5 days after ours. Since their explosion date is in fact almost two hours after the initial detection from Itagaki, we are unsurprised by the disagreement in companion separations.

As a final remark on the best-fit parameters in Table 2.5, we note that SN 2019yvq and SN 2017cbv have similar rise times (18.7 days and 18.2 days, respectively). These

values are quite typical for SNe Ia – Firth et al. (2015) find an average rise time of 18.98 ± 0.54 days in a sample of 18 well-sampled objects.

Although `lightcurve_fitting` generates model lightcurves and not spectra, we reproduce the spectral effects of this model by taking a spectrum of SN 2011fe at a similar epoch to our earliest spectrum and diluting it with a blackbody of the predicted size and temperature. The effects of this blackbody dilution are shown in Figure 2.10, where it can be seen that they do a qualitatively good job replicating the early spectrum of SN 2019yvq (in black), with its blue continuum and weak features. Further, quantitatively fitting for the best-fit temperature needed to reproduce the strength of spectral features (keeping the radius the same as predicted by the fits) results in a temperature only about 350 K higher than predicted by the models. These two temperatures being consistent with each other provides independent confirmation of the validity of the companion shocking models.

Companion shocking models can produce a wide range of early blue bumps depending on the companion separation, size, and viewing angle (see Figures 2 and 3 of Kasen 2010). While the fits for SN 2019yvq are not perfect, notably underpredicting the strength of the decline to the second epoch of *Swift* data, they both closely reproduce the wavelength-dependent behavior of the early excess and predict a temperature closely aligned with what is expected by diluting an early spectrum with blackbody flux.

2.5.2 Double Detonation

As described in detail in Polin et al. (2019), the explosion mechanism of these models consists of the ignition of a surface layer of He which then detonates the underlying C/O WD. We compared observations of SN 2019yvq with double-detonation models which had WD masses between 0.6 and 1.3 $M_\odot$ and He shell masses between 0.01 and 0.1 $M_\odot$.

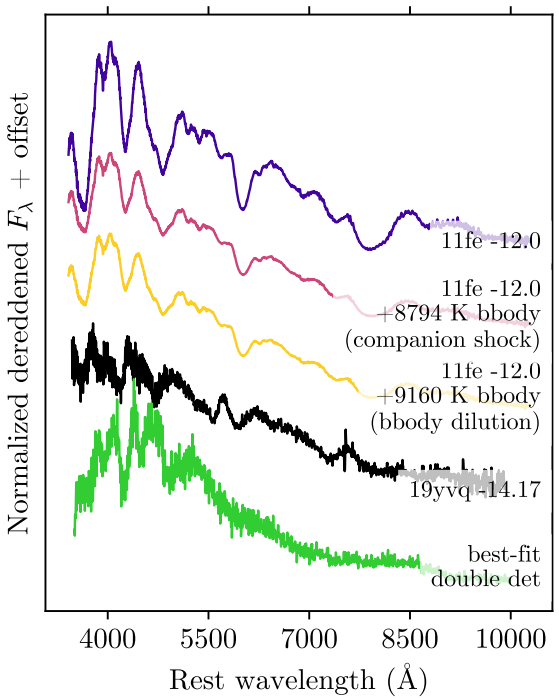

Figure 2.10: Our earliest spectrum of SN 2019yvq (black line) compared to a spectrum of SN 2011fe at a comparable epoch. Epochs listed with respect to days from B-band maximum. The magenta line represents the SN 2011fe spectrum diluted by a 8794 K blackbody, the temperature predicted at that epoch by our best-fit companion shocking models. Allowing the temperature of the blackbody to vary and comparing to the the SN 2019yvq with a χ^2_ν test, we obtain a best-fit temperature of about 350 K higher (yellow line). The green line represents the spectrum at the same epoch (measured from explosion) from the best-fit double detonation model.

We measure the overall best-fit model in our grid by doing a simple reduced χ^2 comparison between each model and the $UBVgri$ photometry. We fix the explosion epoch to be the same used in the best-fit companion shocking model, as described in Section 2.5.1. Normally one would infer an explosion epoch from a power-law fit to the rising data (e.g. Ganeshalingam et al. 2011; Firth et al. 2015) however in this case these fits were very poorly constrained. This was primarily due to a limited number of epochs available for fitting, as there were only four left after ignoring the obviously non-power-law first epoch.

The best-fit model in our grid has a 0.95 $M_\odot$ WD with a 0.055 $M_\odot$ layer of He. This model is shown as the dotted line in the photometry of Figure 2.9 and the color evolution of Figure 2.5, and the spectrum from this model matching the epoch of our earliest SN 2019yvq spectrum is shown in Figure 2.10. Although most of this spectrum is a blue continuum with weak features, in general agreement with the observations, we find that it predicts much stronger features in the ∼4000–5000 Å range and a stronger downturn blueward of ∼4000 Å than are observed.

This model does have a strong excess at the correct epochs (i.e. up to ∼4 days after the explosion), however it dramatically underpredicts most of the U data. The drop after the early excess is also stronger in all bands than is seen in the data, and the models predict a "red bump" which is not seen in the data (see Figure 2.5). Additionally, all reasonably well-fitting models in the grid predict a U decline that is steeper than observed. In the case of the best-fit model, it is steeper than the observed decline-rate by more than a factor of two (in magnitudes per day).

There are also several advantages to double detonation models which match the observed data: a lack of C in the spectra, a weak secondary IR maximum, and a blue/UV excess at roughly the right epochs are some points of agreement.

Both Miller et al. (2020a) and Siebert et al. (2020) use the models from Polin et al. (2019) to fit different aspects of SN 2019yvq's dataset. Fitting to the *gri* ZTF photometry in addition to some *Swift* data over approximately the same epochs shown here, Miller et al. (2020a) find a best-fit model consisting of a 0.92 $M_\odot$ WD with a 0.04 $M_\odot$ He shell. Their results are similar to what is presented here: general agreement on some counts (early blue excess), and diagreement on others (difficulty fitting bluer filters).

Siebert et al. (2020) extend the best-fit model of Miller et al. (2020a) into the nebular phase, and show that the best-fit model based on photospheric photometry is a poor match for nebular spectroscopy, overpredicting the strength of the [Ca II] and [Fe II]

feature by a factor of several. Instead, to match the nebular spectra they find a best-fit model consisting of a 1.1 $M_\odot$ WD with a 0.05 $M_\odot$ He shell. This nebular model is in turn a poor match to the photospheric photometry, overpredicting the bluer bands by more than a magnitude and greatly underpredicting the strength of the early excess in optical bands.

We find it difficult to reconcile this discrepancy, and cannot definitively claim that SN 2019yvq is the result of a double-detonation, despite the several points in favor of these models as listed above.

2.5.3 Nickel Distributions

Photometry

Variations in Ni distributions in the WD progenitor are also known to produce a range of SN Ia behavior (e.g. Piro & Morozova 2016; Magee et al. 2020).

Using the same methodology described in Section 2.5.2, we look for best-fit models from the grid of 255 models provided by Magee et al. (2020). These models make use of the radiative transfer code `TURTLS` (Magee et al. 2018) and vary the density profiles, Ni masses, kinetic energy, and degree of Ni mixing to produce a range of lightcurves up to +25 days from the explosion.

Fitting the *UBVgri* Las Cumbres lightcurve, we find the best-fit model is `EXP_Ni0.4_KE0.50_P3`. This has an exponential density profile, 0.4 $M_\odot$ of Ni, and a kinetic energy of 0.50 foe. The last element of the model name (`P3`) describes the scaling parameter which determines the Ni distribution, and represents the class of model where the Ni is most completely mixed throughout the ejecta.

However, while this model does as well as the other two classes of models we have discussed at fitting the rise time and peak absolute magnitude, it contains no early excess.

The authors note in Magee et al. (2020) that although they can fit a majority of SNe in their sample, the remaining objects have an early excess which the models cannot replicate. Since we consider the early UV excess to be the most unique feature of this SN, the most difficult and interesting aspect to model, and potentially the biggest clue to what the progenitor system is, we do not include this best-fit model in Figure 2.9.

The same authors also released a set of models using a similar methodology capable of reproducing early excesses due to clumps of ^{56}Ni in the outer ejecta (Magee & Maguire 2020). However, since these models were based on SN 2017cbv and SN 2018oh data and both these SNe had typical peak luminosities unlike the underluminous SN 2019yvq, we do not include them as comparisons. Additionally, these models display early red bumps similar to those seen in the double detonation models, which are not seen in our data (see Figure 2.5).

Spectroscopy

In addition to the above photometric modeling, we also utilize TARDIS (Kerzendorf & Sim 2014) to examine the spectroscopic effects of varying Ni distributions and photospheric velocities. A full exploration of these effects are outside the scope of this paper, but we report initial observations here.

We start with a base model, which consists of an early SN 2011fe spectrum identical to the one used in Heringer et al. (2017) at an epoch of +5.9 days from the explosion, similar to the epoch of our earliest spectrum. The `v_inner_boundary` (photospheric velocity) of this model is $12,400$ km/s. We then alter the Ni distribution and photospheric velocity of this model in an attempt to replicate the SN 2019yvq.

Our perturbations were unsuccessful at reproducing the earliest spectrum, but we note observable effects of altering the Ni distribution. Adopting a uniform Ni distribution for the outer ejecta with a mass fraction of 0.19 (replicating the most mixed model of Piro &

Morozova 2016), we note that the red wings of the Si II 6355 and O I 7774 lines become asymmetrically broader, and that the Ca NIR triplet drastically reduces in strength. Artificially introducing a mass of Ni in the outermost portions of the ejecta ($> 20,000$ km/s) weakens the Mg II complex and other features blueward of ∼4500 Å. As the density of this outer Ni mass is increased, other dramatic effects, such as the extreme broadening of the O I 7774 features are introduced, which are not seen in the early spectra of SN 2019yvq.

We also experiment with varying the photospheric velocity of the models, as our earliest spectrum has a Si II 6355 velocity of approximately $21,000$ km s^{-1}, which is significantly higher than the default value of $12,400$ km s^{-1}. Miller et al. (2020a) find velocities of as high as $25,000$ km s^{-1} are necessary to fit their earliest spectrum, but since the maximum velocity in the TARDIS model is $24,000$ km s^{-1} this is unreachable for us. We do note that at high photospheric velocities, such as $18,000$ to $20,000$ km s^{-1}, the strengths of most spectroscopic features begin to match the weak values of our earliest spectrum and the spectrum begins to be dominated by a blue continuum. However, as also pointed out by Miller et al. (2020a), TARDIS has a photospheric boundary which is not wavelength-dependent inside of which is a quasi-blackbody. Because our TARDIS models have a limited velocity range, increasing the model's photospheric velocity thus increases the percentage of the model's mass which acts as a blackbody and effectively dilutes the spectral features from the tenuous outer layers with a strong blackbody component. Blackbody dilution is also a signature of the companion shocking models, and is shown in Figure 2.10. The blackbody temperature predicted by the companion shocking models is also thousands of Kelvin hotter than the photospheric temperatures TARDIS calculates for this velocity range (between 6,000 and 7,000 K).

Miller et al. (2020a) use additional Ni distribution models based on Magee & Maguire (2020) and find that the predicted spectra have strong line blanketing blueward of ∼4400

Å, in addition to overpredicting the i-band flux.

Since unusual Ni distributions result in spectral features absent in the observed spectra, and since high photospheric velocities replicate the effects of the companion interaction scenario, we do not include these spectra in our comparisons.

2.5.4 Constraints on Circumstellar Interaction from Radio Observations

Radio emission is a sensitive probe of circumstellar medium (CSM) of the progenitor. The CSM is polluted by mass-loss from the progenitor in the pre-SN stage, and interaction of the SN ejecta with this CSM accelerates electrons to relativistic energies and amplifies the ambient magnetic field, producing synchrotron radio emission (Chevalier 1982, 1984, 1998). Simple models of radio emission have provided constraints on the CSM environment and progenitor properties for both core-collapse (e.g. Ryder et al. 2004; Soderberg et al. 2006; Chevalier & Fransson 2006; Weiler et al. 2007; Salas et al. 2013) and SNe Ia (Panagia et al. 2006; Chomiuk et al. 2016). Radio emission is yet to be detected from a SN Ia , but non-detections have provided stringent constraints on progenitor scenarios (Chomiuk et al. 2016), particularly for nearby events like SN 2011fe (Horesh et al. 2012; Chomiuk et al. 2012) and SN 2014J (Pérez-Torres et al. 2014).

Radio observation of SN 2019yvq was obtained with the Karl G. Jansky Very Large Array (VLA) on 2020 Jan 26, 11:39:53, which is within 29.77 days of t_0 (derived in Section 2.2.2). The observation block was 1-hr long, with 38.23 mins time-on-source for SN 2019yvq. Observations were taken in X-band (8–12 GHz) in the D-configuration of the VLA (DDT: 19B-346, PI: S. Sarbadhicary). The observations were obtained in wide-band continuum mode, yielding 4 GHz of bandwidth sampled by 32 spectral windows, each 128 MHz wide sampled by 1 MHz-wide channels with two polarizations. We used 3C286

as our flux and bandpass calibrator, and J1313+6735 as our phase calibrator. Data were calibrated with the VLA CASA calibration pipeline (version 5.6.2-2) [7]. The pipeline consists of a collection of algorithms that automatically loads the raw data into a CASA measurement set (MS) format, flags corrupted data (e.g. due to antenna shadowing, channel edges, radio frequency interference or RFI), applies various corrections (e.g. antenna position, atmospheric opacity) and derives delay, flux-scale, bandpass and phase calibrations which are applied to the data.

We imaged the calibrated visibility dataset with `tclean` in CASA. We used multi-term, multi-frequency synthesis as our deconvolution algorithm (set with `deconvolver='mtmfs'` in `tclean`), which performs deconvolution on a Taylor-series expansion of the wide-band spectral data in order to minimize frequency-dependent artifacts (Rau & Cornwell 2011). We set `nterms=2` which uses the first two Taylor terms to create images of intensity (Stokes-I) and spectral index. The SN is offset $\sim 13''$ from the bright central radio nucleus of the galaxy, and as a result the emission at the SN site is dominated by sidelobes from the nucleus for the typical resolution $\sim 7.2''$ expected in X-band images in D-configuration. For this reason, we only imaged the 10-12 GHz bandwidth with `tclean`, excluded visibility data from baselines shorter than 6 kλ, and applied Briggs-weighting on the remaining visibility data with the parameter `robust=0`. This provided just enough angular resolution and source sensitivity at the SN site to determine if any radio emission separate from the nucleus is associated with the SN site.

No radio source was detected at the site of SN 2019yvq in the cleaned, deconvolved 11-GHz image with a synthesized beam of $5.5'' \times 4.2''$. The flux at the exact location of the SN is -25μJy. Using the AIPS task `IMEAN`, we obtain an RMS of 11.7μJy per beam, which translates to a 3σ 11-GHz luminosity limit of 7.6×10^{25} ergs/s/Hz, assuming a distance of 42.5 Mpc.

[7] https://science.nrao.edu/facilities/vla/data-processing/pipeline

The 3σ upper limit can shed some light on the CSM around 2019yvq similar to the methodology in Chomiuk et al. (2012) and Chomiuk et al. (2016). Using the Chevalier (1982) model of a CSM characterized by $\rho = \dot{M}/4\pi r^2 v_w$ (where ρ is density in gm/cm^3, $\dot{M}$ is the mass-loss rate from the progenitor, r is the distance from progenitor and v_w is wind velocity), we obtain an upper limit of $(4.5\text{—}20) \times 10^{-8}$ M$_\odot$/yr on the mass-loss rate from a symbiotic progenitor (involving a red-giant companion, assuming v_w=10 km/s). The range of mass-loss rates reflect the uncertainty in the parameter ϵ_b, the fraction of shock energy shared by the amplified magnetic field, with typical values in the range 0.01-0.1 for SNe (Chomiuk et al. 2012). These limits are shown in Figure 2.11. Chomiuk et al. (2016) measured the mean mass-loss rate in symbiotic progenitors in the Milky Way to be $\log_{10}(\dot{M}) = -6.41 \pm 1.03$ M$_\odot$/yr (asssuming $v_w = 100$ km/s), so our measurement does not exclude the possibility of a red-giant companion. Scenarios involving accretion from a main-sequence companion accompanied by steady nuclear burning are also not excluded by our limit (Chomiuk et al. 2012).

2.6 Discussion

SN 2019yvq is an unusual event in many respects. It has: a strong early UV flash; red colors besides the early flash; relatively faint peak luminosity, a moderately high decline rate, and a weak secondary IR maximum; broad, high-velocity Si II 6355 paired with both weak Si II 5972 and Ti II at peak; and nebular [Ca II] and [Fe II]. These paint a conflicting picture, with some aspects pointing to a low-energy explosion (low luminosity, weak secondary IR maximum, nebular [Ca II], peak Ti II) and others pointing to a high-energy event (Si II velocity and line ratio). Due to several characteristics it shares, or almost shares, with low-luminosity 02es-like SNe Ia, we classify it as a transitional member of that subclass (see Table 2.3 and the rest of Section 2.4).

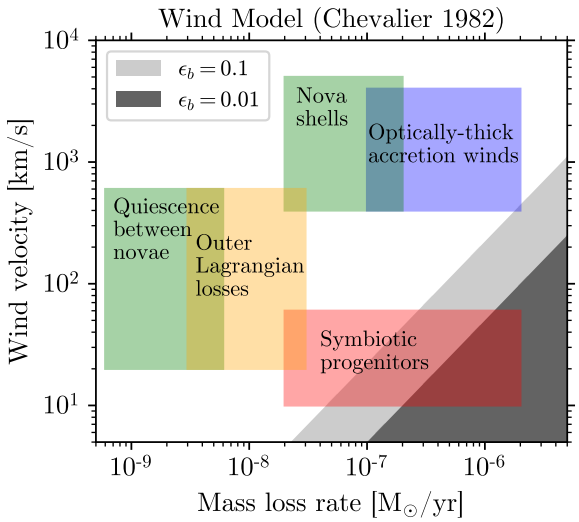

Figure 2.11: Limits (in gray) for the mass loss rate of the progenitor of SN 2019yvq from its VLA observations, following the model of Chevalier (1982), shown for typical range of values of ϵ_b which parameterizes the fraction of shock energy in the amplified post-shock magnetic field in radio light curve models. These observations can rule out some symbiotic progenitor systems, but they do not exclude red giant companions or other methods of mass loss.

This object being a transitional 02es-like has two major implications.

The first is the confirmation that transitional 02es-like SNe Ia can exist. This has precedent in the object SN 2006bt (Foley et al. 2010; Ganeshalingam et al. 2010), which can be considered a transitional member of this class (Taubenberger 2017) despite its high velocities (12,500 km s^{-1} at 3 days before maximum) and relatively bright luminosity ($M_{B,\mathrm{peak}} \sim -19$, with uncertain reddening correction). This object is included in both Figure 2.6 (orange star) and Figure 2.8 for comparison. However, SN 2019yvq is by no means a clone of SN 2006bt as it lies in extremely sparsely populated regions of parameter space in several respects (see Figure 2.6, also Figure 2 of Tucker et al. 2021). On the Phillips relation SN 2019yvq has similar parameters to SN 2012Z, but on the Branch diagram SN 2019yvq is most similar to SN 2002bo. SNe 2002bo and 2012Z are substantially different SNe. A transitional 02es-like SN that not only shares character-

istics with both these SNe but is also distinct from another transitional member of its subclass supports evidence that there is a continuum of events between normal SNe Ia and 02es-likes. Assuming a continuum of events instead of discrete subclasses, this also suggests that 02es-like SNe do not arise from progenitor systems which are distinct from the systems of normal SNe Ia.

The second major implication comes from the fact that the three 02es-like SNe Ia with very early data (SN 2019yvq, iPTF14atg, and iPTF14dpk) all display unusual early-time lightcurves (see Section 2.4 and Table 2.4). Of these, the two with *Swift* data at these early epochs display the two strongest early UV flashes in SNe Ia. iPTF14dpk unfortunately only has R-band photometry, and while at first glance its first data point appears indicative of an early excess, Cao et al. (2016) say that this would require an extreme explosion energy and would lead to higher velocities than are observed. The lack of multi-band photometry makes us hesitant to accept that conclusion incontrovertibly. According to Kasen (2010), if such early excesses are due to companion–ejecta shock interaction they should only be seen in $\sim$10% of events with such early data. Instead, for 02es-like SNe Ia, they are seen in two (or three) of the three early events. This is unlikely – even with the current small sample size, the odds of so many early excesses are somewhere between 1 in 100 and 1 in 1000. And as discussed in Section 2.5.2, the discrepancies between photospheric and nebular best-fit models make us hesitant to claim that SN 2019yvq is a double detonation event either, even though those models can produce early UV excesses. We are left considering progenitor scenarios which could produce an early excess which is both fit relatively successfully by shock interaction models but is not viewing angle-dependent.

In addition to models which have already been discussed (double detonations and varied Ni distributions, see Sections 2.5.2 and 2.5.3), there are a few possibilities for progenitor systems configured in such a way to produce more isotropic shocks. One option

lies in the accretion disks which form as the (primary) WD accretes matter. Levanon & Soker (2019) model the exquisitely sampled early bump seen in the K2 data of SN 2018oh as the interaction of the SN ejecta with what they refer to as "Disk-Originated Matter," since accretion disks could also give rise to bipolar jets. The addition of an accretion disk and jets would more easily account for the ubiquity of early excesses since these components can be seen more isotropically. Piro & Morozova (2016), in addition to modeling the degree of Ni mixing in WD progenitors, also investigate the effects of a more general distribution of CSM. These models can produce early excesses which occur on a range of timescales and intensities, depending on the total amount of external matter in the CSM and its density scaling. In particular they can produce early bumps which only last $\sim$2 days, which could explain the (potential) extremely brief excess seen in iPTF14dpk. These CSM models also get redder immediately after the explosion instead of bluer like the Ni mixing models. This early reddening more accurately reflects the color evolution of SN 2019yvq.

Cao et al. (2016) model the 02es-like SNe Ia iPTF14atg and iPTF14dpk as interacting with non-degenerate companions, but seen from different viewing angles. The addition of SN 2019yvq as another member of the rare 02es-like subclass, with a commensurate early UV excess, leads us to doubt that all three of these excesses arise from ejecta–companion shock interaction. Something about their progenitor systems must be more isotropic than is assumed in Kasen (2010) to explain the ubiquity of these early excesses in 02es-like SNe Ia.

2.7 Conclusions & Summary

We have discussed the discovery and follow-up observations of SN 2019yvq, a nearby SN Ia with a rare and unusually strong excess in its early lightcurve, in addition to several

other uncommon features. This early excess is most pronounced in the UV, where the object is brighter during the excess than during the epochs of its optical peak.

This object is one of a very limited number of SNe Ia with early UV/blue excess, and it demonstrates an even stronger excess than other objects in the sample. SN 2019yvq deviates significantly from SNe Ia that are blue at early times but otherwise normal. Instead it shares some, but not all, features of the 02es-like SN Ia subclass, including a low peak luminosity, red color, moderately high decline rate, Ti II at peak, and nebular [Ca II] and [Fe II]. We classify SN 2019yvq as a transitional member of the 02es-like subclass.

Although models which simulate WD double detonation and ejecta–companion shock interaction can create lightcurves with excess flux at early times, we find that no one model can accurately reproduce all unusual aspects of this object's dataset. This is in broad agreement with the conclusions drawn in Miller et al. (2020a) and Tucker et al. (2021), which include several pieces of data not present here (including i-band ZTF data, post-maximum TESS data, and a Keck NIRES spectrum) and, like us, are unable to satisfactorily explain every aspect of the SN 2019yvq dataset. As in Siebert et al. (2020) we also find strong [Ca II] and [Fe II] emissions in the nebular spectra of SN 2019yvq in addition to strong limits on the amount of swept-up H and He, but we do not take this as exclusive evidence of a double detonation explosion.

Two other 02es-like SNe Ia also display unusual early lightcurves (iPTF14atg and iPTF14dpk). The deviations from a power-law rise in all 02es-like SNe Ia with sufficiently early data makes us further doubt that the early UV excess seen in SN 2019yvq arises from ejecta–companion shock interaction, as viewing angle effects dictate that such excesses should only be seen in $\sim$10% of events with early data, not $\sim$100%. 02es-like SNe Ia must originate in progenitor systems capable of displaying early excesses nearly isotropically. The addition of CSM or accretion disks and jets could account for this needed isotropy.

This SN demonstrates the importance of prompt discovery, reporting, and follow-up of young SNe. In this case, the one day non-detection enabled rapid follow-up with multiple facilities around the world and in space. The synthesis of such high-cadence multiwavelength datasets is a powerful tool for understanding the origins of SNe Ia, or for providing even more observational peculiarities which accurate models must account for.

Chapter 3

Early Lightcurves of Type Ia Supernovae are Consistent with Nondegenerate Progenitor Companions

This chapter is reproduced from Burke et al. (2022b) by permission of the American Astronomical Society. I would like to thank my coauthors, without whom this work would not have been possible: D. A. Howell, D. J. Sand, R. C. Amaro, P. J. Brown, I. Arcavi, J. E. Andrews, K. A. Bostroem, Y. Dong, J. Haislip, D. Hiramatsu, G. Hosseinzadeh, V. Kouprianov, M. J. Lundquist, C. McCully, C. Pellegrino, D. Reichart, L. Tartaglia, S. Valenti, S. Wyatt, and S. Yang.

3.1 Introduction

Despite the fact that type Ia supernovae (SNe) were used as standardizable candles to discover the accelerating expansion of the universe and constrain its energy content (Riess et al. 1998; Perlmutter et al. 1999), many open questions remain about their progenitor systems. The supernovae themselves are understood to be the thermonuclear explosions of carbon/oxygen white dwarfs (WDs) (Hoyle & Fowler 1960), but the channels by which

these explosions occur are poorly constrained.

A large body of literature exists modeling the progenitor systems and explosion mechanisms of SNe Ia. The two most commonly invoked progenitor systems are the single-degenerate case (Whelan & Iben 1973), where the WD accretes matter slowly from a nondegenerate companion, and the double-degenerate case (Iben & Tutukov 1984), where the source of the extra matter needed to ignite the WD is a second WD. Several varieties of explosion mechanisms have also been modeled, for instance double-detonation models. These models have a surface layer of He which detonates, driving a thermonuclear shock into the WD causing the core to detonate (Sim et al. 2012; Polin et al. 2019). Some channels have been suggested which explicitly combine different progenitor systems and explosion mechanisms, such as the dynamically-driven double-degenerate double-detonation channel (Shen et al. 2018). For reviews, see Howell (2011), Wang & Han (2012), Maoz et al. (2014), and Jha et al. (2019).

There are several observational signatures that could distinguish between single- and double-degenerate progenitor systems. One such signature we focus on in this paper arises in the single-degenerate case: if the donor star were nondegenerate then the SN ejecta should run into it and get shock-heated. The shock-heated ejecta would then emit an excess of blue/UV light which could be detected in the SN's early lightcurve, as was predicted and modeled in Kasen (2010). The excess is expected to be only be detectable within $\sim$5 days of explosion – SNe Ia have a range of rise times, but this translates to earlier than $\sim$14 days before maximum light (Miller et al. 2020b). The strength of this signature is dependent on the companion's size and separation, the velocity of the ejecta, and the viewing angle of the event. The viewing angle effect alone means that only approximately 10% of SNe Ia arising from this single-degenerate channel would display a strong early excess, and even then, excellent early, multiwavelength, high-cadence datasets are necessary to identify these features.

Early excesses in SNe Ia were predicted to arise from this channel before any such features were observed. A small number of SNe Ia with early excesses have since been discovered and modeled: SN 2012cg (Marion et al. 2016), the 02es-like iPTF14atg (Cao et al. 2015), iPTF16abc (Miller et al. 2018), SN 2017cbv (Hosseinzadeh et al. 2017), SN 2018oh (Li et al. 2019; Dimitriadis et al. 2019a; Shappee et al. 2019), the transitional 02es-like SN 2019yvq (Miller et al. 2020a; Siebert et al. 2020; Tucker et al. 2021; Burke et al. 2021), and SN 2021aefx (Ashall et al. 2022; Hosseinzadeh et al. 2022). Other objects have unusual early data, such as SN 2018aoz, which showed extreme color evolution in the hours after explosion (Ni et al. 2022a). Some papers in the literature have noted objects with weaker early excesses without providing detailed models for any one event (Jiang et al. 2018; Deckers et al. 2022) , and other work has established some limits on the rates of early excesses based on non-detections in samples of SNe Ia (Bianco et al. 2011; Brown et al. 2012a; Olling et al. 2015; Fausnaugh et al. 2021).

In addition to companion shocking, other physical effects can also give rise to early lightcurve features. An early excess could instead arise from radioactive decay of matter in the outer ejecta, either from Ni mixed throughout the WD as it burns (Piro & Morozova 2016; Magee & Maguire 2020) or from a layer of accreted He on the surface of the WD (see the double-detonation models described above and in Polin et al. 2019). These double-detonation models originally needed large amounts of He ($\sim$0.2$M_\odot$) in order for the He detonation to disrupt the WD (Sim et al. 2012), but this amount of He results in spectra and color evolutions which significantly differ from observed SNe Ia (see Figures 5 and 7 of that paper). More recent double-detonation models (Polin et al. 2019) require significantly less He (down to 0.01$M_\odot$), although the models still have spectra and color evolutions which are atypical for most SNe Ia.

A complementary line of inquiry relies not on the early photometry, but on nebular spectroscopy. In single-degenerate progenitor systems one would expect the companion

star to be stripped to some degree and to leave signatures of H in the spectra which become visible in the nebular phase once the SN has faded (Marietta et al. 2000; Botyánszki et al. 2018; Dessart et al. 2020). This signature has not been observed for >100 SNe Ia with nebular spectra, often to very constraining limits of $M_{\text{stripped H}} < 10^{-3}\text{M}_{\odot}$ (for recent compilations see Maguire et al. 2016; Sand et al. 2019; Tucker et al. 2020). It has been observed in a handful of cases, namely SN 2016jae (Elias-Rosa et al. 2021), SN 2018cqj (Prieto et al. 2020), and SN 2018fhw (Kollmeier et al. 2019). Curiously, all three SNe are underluminous, with $M_{B,\text{peak}}$ fainter than -18, and no Hα has been observed for any objects with an early UV excess including for SN 2017cbv (Sand et al. 2018), SN 2018oh (Dimitriadis et al. 2019b; Tucker et al. 2019), or SN 2021aefx (Ashall et al. 2022; Hosseinzadeh et al. 2022). In addition to this paper focusing on early-time photometry, a companion paper (Sand et al. 2022, in prep.) will focus on the nebular spectra of objects in this sample, although no signatures of Hα are detected.

X-ray non-detection limits can also be used to probe the circumstellar environments of SN Ia progenitors. Non-detections throughout the literature are collected in Sand et al. (2021), which also presents stringent new limits for two objects: SNe 2017cbv (discussed here) and 2020nlb. The observations of these two objects are among the strongest X-ray limits for any SNe Ia, and effectively rule out a symbiotic giant star companion for their progenitor systems (see Figure 6 of that paper).

A sample of early SNe Ia lightcurves needs early, high-cadence, multiwavelength photometry to characterize any potential early excesses. Such a sample has become easier to build up in recent years due to the proliferation of time-domain surveys such as ASAS-SN (Shappee et al. 2014; Kochanek et al. 2017), ATLAS (Tonry et al. 2018), DLT40 (Tartaglia et al. 2018), and ZTF (Bellm et al. 2019). Combining discoveries from these surveys with followup from facilities like Las Cumbres Observatory (LCO; Brown et al. 2013) and the Neil Gehrels Swift Observatory (Swift; Gehrels et al. 2004) allows for

characterization of SNe Ia at early times across a wide range of UV, optical, and NIR wavelengths at daily or sub-day cadences.

We present an analysis of the early lightcurves of nine nearby SNe Ia, observed by LCO and Swift, and in most cases discovered by DLT40, a sub-day cadence SN survey of nearby galaxies. In total we have 6,110 data points, beginning an average of 16.0 days before maximum light. Utilizing LCO allows for sub-day cadence observations from U-band through i-band: this high cadence multiwavelength followup is the ideal way to characterize early SNe Ia as it can probe observational signatures at short timescales and across the optical spectrum, even into the near-UV where companion interaction signatures are expected to dominate at early times. We search for signatures of companion interaction in our sample and find three such cases, including in the data of SN 2018yu, published here for the first time. We compare to separate model grids in an effort to distinguish between different progenitor systems and explosion mechanisms, although ultimately we favor companion interaction models. We also measure rise times and colors to compare to literature values.

This paper is organized as follows. In Section 3.2 we detail the different data sources and reduction methods. In Section 3.3 we analyze the lightcurves, measuring standard parameters such as stretch and peak magnitudes. Using those parameters we fit our data with different models and characterize early excesses in Section 3.4, and in Section 3.5 we compare the color evolution of our sample to samples of SNe Ia from the literature. We discuss the pros and cons of our adopted companion interaction models in Section 3.6, before concluding in Section 3.7.

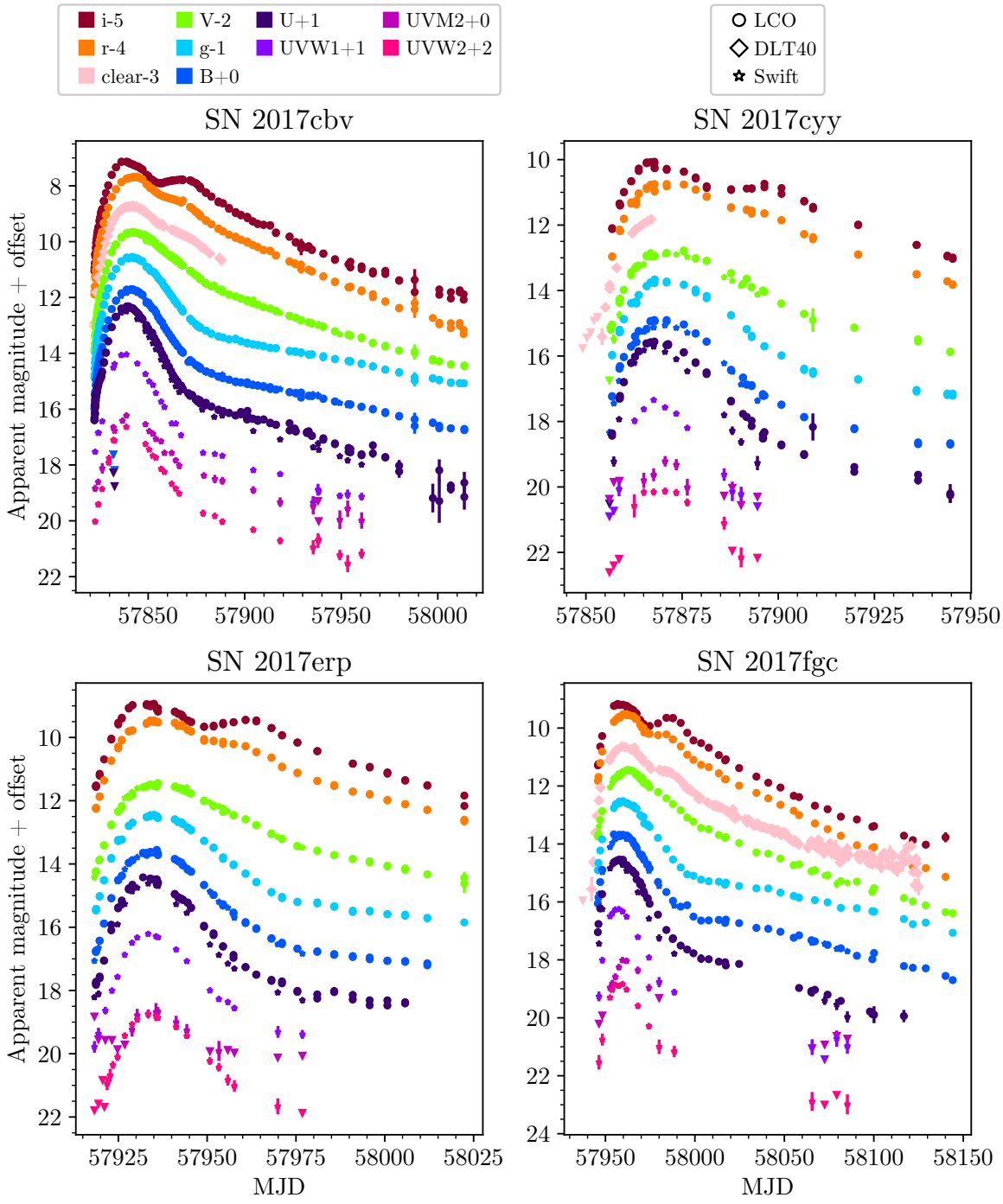

Figure 3.1: Full datasets (DLT40+LCO+Swift) for all objects in the sample. Lower limits are included as downward-pointing triangles.

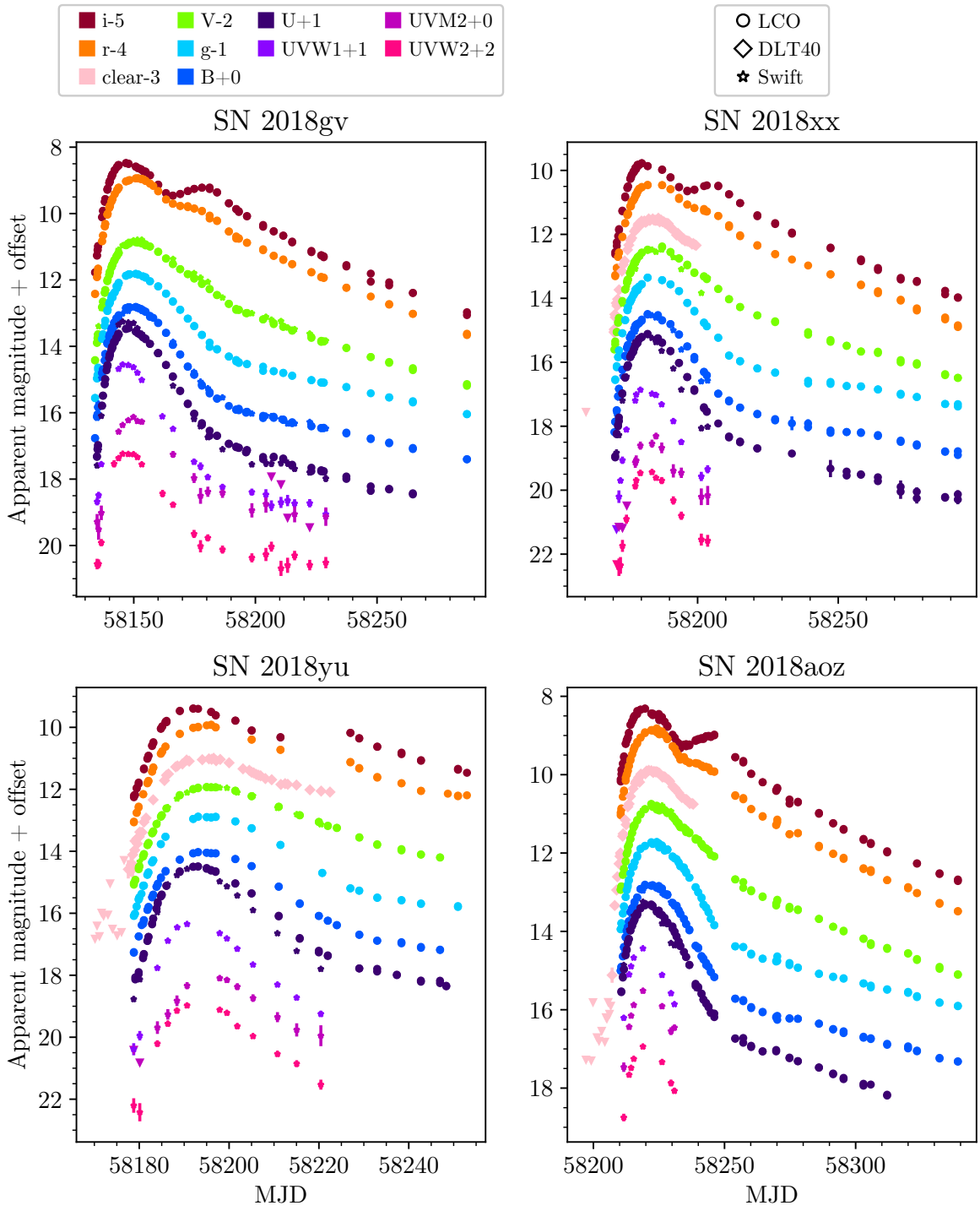

Figure 3.1: Continued.

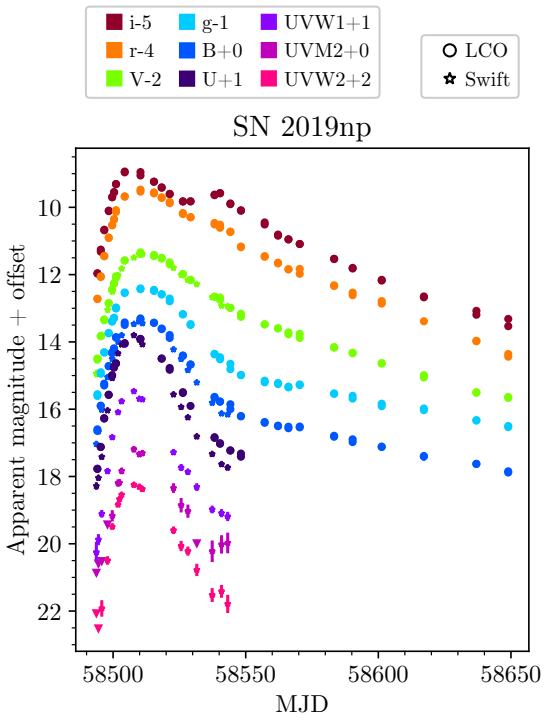

Figure 3.1: Continued.

3.2 Observations and Data Reduction

Of the nine objects in this sample, most were discovered by the DLT40 survey and all have high-cadence multiwavelength lightcurves from LCO, with additional UV photometry from Swift. Our full dataset is presented in Figure 3.1.

Although a focus of this paper is the modeling of early excesses (see Section 3.4.1), we did not select the sample based on objects with early excesses. We constructed this sample attempting to be as unbiased as possible, using the following criteria: we consider all nearby ($z < 0.01$) spectroscopically normal SNe Ia discovered between 2017 and 2019 (inclusive), which were thoroughly observed (>300 images) by the Global Supernova Project at LCO. These criteria yield a sample of 11 objects, and we impose two additional requirements: that the objects be discovered within a few days of explosion (this removes one object, SN 2017gah) and that the objects do not have excessive reddening ($A_V < 1 \Rightarrow E(B-V) < 0.322$), since accurate absolute magnitudes are needed to judge the strength or absence of any early excesses and since high extinction decreases the signal-to-noise in the crucial early blue data, making it more difficult to detect early blue bumps (this removes another object, SN 2017drh, which has $E(B-V) > 1$). These criteria result in a sample of nine SNe Ia. The sample is not perfectly unbiased (e.g. the Global Supernova Project only elects to follow a subset of nearby SNe Ia given finite observing time), but it represents the state of the art for samples of nearby SNe Ia with early, high-cadence, truly multiwavelength data. The sample should not be biased to skew towards objects with early bumps.

3.2.1 Discovery

The majority of SNe presented here (SN 2017cbv, SN 2017cyy, SN 2017fgc, SN 2018aoz, SN 2018xx, SN 2018yu) were discovered by the Distance Less Than 40 Mpc survey

(DLT40; Tartaglia et al. 2018). DLT40 is a ∼12-24 hr cadence search for nearby SNe, targeting galaxies within $D \lesssim 40$ Mpc, and designed with the goal of discovering ∼5–10 SNe per year within a day of first light. Initially DLT40 operated a single 0.4-m telescope at Cerro Tololo Inter-American Observatory (CTIO) in Chile, with a second telescope at Meckering Observatory (Western Australia) joining the search in 2017 December. Further technical details of this program are discussed elsewhere (Yang et al. 2019; Bostroem et al. 2020), and we utilize the full DLT40 lightcurves and detection limits here (seen as the pink points in Figure 3.1) to help provide useful constraints on the explosion epoch and rise times.

DLT40 photometry is taken in a "clear" (Meckering Observatory) or "open" (CTIO) filter, and is calibrated to r-band photometry of the AAVSO Photometry All-Sky Survey (APASS; Henden et al. 2009). For the purposes of this work, we will refer to this DLT40 light curve data as "clear" for convenience.

The three objects in this sample not discovered by DLT40 (i.e. SNe 2017erp, 2018gv, and 2019np) were all discovered by the amateur astronomer Koichi Itagaki (Itagaki 2017, 2018, 2019a).

3.2.2 Followup

After discovery, we performed intensive high-cadence multiwavelength followup with the telescopes of LCO in addition to UV–optical observations from Swift. Photometric reduction for the LCO images was accomplished using `lcogtsnpipe` (Valenti et al. 2016), a PyRAF-based pipeline. All SNe were bright enough and far enough separated from their host galaxies that their reductions did not require template image subtraction.

We report all UBV observations in Vega magnitudes. We calculate zeropoints for Landolt filters using same-night same-telescope observations of Landolt standard fields

(Stetson 2000). We report all *gri* observations in AB magnitudes. We calculate zeropoints for Sloan filters using using Sloan catalog stars in the fields of each SN where possible (SDSS Collaboration et al. 2017). If there are no Sloan catalog stars in the field, we used APASS catalog stars for zeropoint calibration (Henden et al. 2009).

Additionally, all SNe presented here have also been observed by Swift using the the Ultra-Violet Optical Telescope (UVOT; Roming et al. 2005). Observations were reduced using the pipeline associated with the Swift Optical Ultraviolet Supernovae Archive (SOUSA; Brown et al. 2014) and the zeropoints of Breeveld et al. (2010).

Our full dataset is presented in Figure 3.1.

3.3 Analysis

In this section we will discuss analysis done on the photometry to derive standard lightcurve parameters. Results are summarized in Table 3.1.

SN	$\mathrm{MJD}_{\mathrm{max}}$	m_B	DM	M_B	Δm_{15}	s
2017cbv	57840.29 ± 0.09	11.715 ± 0.008	30.657 ± 0.007	-19.55 ± 0.01	0.953 ± 0.009	$1.031^{+0.002}_{-0.002}$
2017cyy	57870.12 ± 0.04	14.89 ± 0.01	33.443 ± 0.009	-19.46 ± 0.03	1.067 ± 0.007	$0.927^{+0.007}_{-0.007}$
2017erp	57934.41 ± 0.04	13.60 ± 0.02	32.32 ± 0.02	-19.48 ± 0.03	0.987 ± 0.008	$0.939^{+0.007}_{-0.006}$
2017fgc	57959.47 ± 0.06	13.70 ± 0.02	32.06 ± 0.02	-19.46 ± 0.04	1.061 ± 0.005	$1.08^{+0.02}_{-0.02}$
2018gv	58149.64 ± 0.01	12.847 ± 0.006	32.125 ± 0.006	-19.48 ± 0.01	1.014 ± 0.005	$1.0381^{+0.0003}_{-0.0003}$
2018xx	58183.90 ± 0.02	14.58 ± 0.02	33.39 ± 0.02	-19.43 ± 0.03	1.159 ± 0.003	$0.847^{+0.002}_{-0.002}$
2018yu	58194.32 ± 0.04	14.002 ± 0.007	33.011 ± 0.007	-19.51 ± 0.01	0.952 ± 0.005	$1.043^{+0.004}_{-0.003}$
2018aoz	58222.18 ± 0.02	12.846 ± 0.004	31.623 ± 0.004	-19.12 ± 0.01	1.432 ± 0.002	$0.881^{+0.002}_{-0.002}$
2019np	58509.64 ± 0.06	13.37 ± 0.03	32.80 ± 0.03	-19.65 ± 0.06	0.98 ± 0.01	$1.05^{+0.03}_{-0.03}$

Table 3.1: Lightcurve parameters for objects in the sample, using the methodology detailed in Section 3.3. We measure the peak magnitude in B-band (m_B) by fitting to the observed lightcurve (i.e. not dereddened), whereas we have dereddened the peak absolute magnitude (M_B). The Δm_{15} is derived from `SNooPy`, and does not directly correspond to $\Delta m_{15}(B)$. $\mathrm{MJD}_{\mathrm{max}}$ is also specifically for B-band data. Objects are consistent with zero host extinction, besides SN 2017fgc ($E(B-V) = 0.231 \pm 0.006$), SN 2017erp ($E(B-V) = 0.098 \pm 0.006$), and SN 2018xx ($E(B-V) = 0.037 \pm 0.005$).

SN	z	Host name	Host type
2017cbv	0.003999	NGC5643	SABcd
2017cyy	0.009777	ESO091-015	SABm
2017erp	0.006174	NGC5861	SABc
2017fgc	0.007722	NGC474	SA0
2018gv	0.00527	NGC2525	SBc
2018xx	0.00999	NGC4767	E
2018yu	0.008112	NGC1888	SBc pec
2018aoz	0.005801	NGC3923	E4-5
2019np	0.00452	NGC3254	SABc

Table 3.2: Host information for objects in the sample.

3.3.1 `SNooPy`

We make use of the `SNooPy` package (Burns et al. 2011) to measure several lightcurve parameters, including the host extinction and distance modulus. Following Burke et al. (2021) we do exclude both U-band data (since `SNooPy` cannot fit that data) and i-band data (since the variation in secondary IR maxima leads to overfitting that feature, with worse overall fits; see Pessi et al. 2022 for an investigation of the variation in secondary i-band maxima and its effect on SN Ia parameter estimation).

We do fits using the default `EBV_model` and the `fitMCMC()` procedure, enforcing $R_{V,\mathrm{host}} = 3.1$. Multiple objects (SN 2017cbv, SN 2017cyy, SN 2018yu, SN 2018aoz) converge to small negative (and therefore unphysical) values of $E(B-V)$. This can also be seen when comparing the MW-dereddened $B-V$ colors to the "Lira Law" (see Equation 1 and Figure 1 of Phillips et al. 1999), as those objects are slightly bluer than the expected Lira Law template. As such, when doing the MCMC fit we impose a uniform prior on `EBVhost` ranging from 0 to 1. We visually inspect fits to ensure that they are reasonable.

Most objects converge to 0 host extinction, as expected from the fact that they are well-separated from their host galaxies. The two highest-reddening objects are

SN 2017erp ($E(B-V)_{\rm host} = 0.098 \pm 0.006$) and SN 2017fgc ($E(B-V)_{\rm host} = 0.231 \pm 0.006$). SN 2017erp was the subject of study in Brown et al. (2019), which found two possible fits to the host extinction: $E(B-V) = 0.10$ ($R_V = 3.1$), or $E(B-V) = 0.18$ ($R_V = 1.9$). Our value is consistent with the $R_V = 3.1$ value in that paper. SN 2017fgc has also been studied before, and our value is consistent with that found in Zeng et al. (2021) ($E(B-V) = 0.17 \pm 0.07$).

We convert each object's $E(B-V)$ to per-filter extinction values in two different ways, depending on the filter. For $UBVgri$ data, we use the Schlafly & Finkbeiner (2011) recalibration of the Schlegel et al. (1998) dust maps, accessed by the Python package `extinction` (Barbary 2016). For Swift filters we use the method described in Brown et al. (2010), specifically the red-corrected coefficients listed in Table 1 of that paper.

We also use `SNooPy` to measure the distance modulus for each object. Host information for the objects in the sample is listed in Table 3.2. Eight of the nine objects are in NGC galaxies, each of which has a variety of redshift-independent distance measurements cataloged on the NASA/IPAC Extragalactic Database (NED[1]). The measurements for a single object can have a wide range: the average standard deviation for host galaxies' distance moduli is 0.71 mags, with measurements for one object (NGC 1888) ranging from 27.98 (Bottinelli et al. 1985) to 33.06 (Terry et al. 2002). In an effort to use a uniform methodology for measuring distance we adopt the values inferred by `SNooPy`, which are consistent with the range of values listed on NED for each host.

Lastly, we measure the peak brightness in B-band using the `get_max` method in `SNooPy`. The absolute magnitudes range from -19.12 ± 0.01 for the faintest object (SN 2018aoz) to -19.65 ± 0.06 for the brightest (SN 2019np) – this distribution conforms to the range expected for normal SNe Ia (see e.g. Figure 7 of Ashall et al. 2016 where the

[1] https://ned.ipac.caltech.edu/

majority of their sample has $-20 < M_B < -19$).

The time of maximum (for B-band), peak apparent magnitude, and dereddened peak absolute magnitude, in addition to the distance modulus and Δm_{15}, are all reported in Table 3.1.

3.3.2 Stretch

Stretch (s) is a single parameter useful in modeling SNe Ia (Perlmutter et al. 1997, 1999; Goldhaber et al. 2001), measured by taking a flux-normalized SN Ia lightcurve and stretching it temporally to maximize overlap with a template. Although relations exist to convert Δm_{15} to s (e.g. Ganeshalingam et al. 2011), we independently measure s for the objects in our sample.

We make use of the MCMC framework of the `lightcurve_fitting` package (Hosseinzadeh 2019), which utilizes the `emcee` package (Foreman-Mackey et al. 2013). We create a simplified version of the `CompanionShocking` model that eliminates the actual companion shocking calculation, but keeps the stretch-correction to an $s = 1$ SiFTO template (Conley et al. 2008).

We limit the data to around peak (-10 to +30 days), and we additionally limit to only B-band data as done in Goldhaber et al. (2001). We monitor MCMC walkers to ensure successful burn-in and convergence. Stretches are reported in Table 3.1.

The measured stretch values also confirm that the sample consists of normal SNe Ia: the average stretch of the sample is 1.03 ± 0.04 (consistent with the expected value of 1 for samples of normal SNe Ia). The object most discrepant from $s = 1$ is SN 2018xx ($s = 0.847 \pm 0.002$), still above the cutoff of $s > 0.8$ typically used for differentiating fast-declining/subluminous SNe Ia (González-Gaitán et al. 2011).

3.4 Model Fits and Early Excesses

In this section we use the parameters measured in the above section, notably the distance modulus and the host extinction from which we derive absolute magnitudes, to compare to a variety of early SN Ia models.

3.4.1 The Search for Blue Bumps

Description of companion shocking models

We fit the early LCO+DLT40 data of our objects (to $t_{\rm max}$+5 days) with models similar to those described in Hosseinzadeh et al. (2017), Burke et al. (2021), and Hosseinzadeh et al. (2022), making use of the `lightcurve_fitting` package (Hosseinzadeh 2019). The models consist of two components: a template lightcurve representing a $s = 1$ SN Ia from `SiFTO` (as described in Section 3.3.2), to which is added excess flux arising from a companion shocking interaction, which can dominate at early times.

For the `SiFTO` template, we refer to Conley et al. (2008) for the full details of its construction. But for the earliest epochs, the per-filter templates are extrapolated to zero flux with a power law of the form $f = a(t - t_{\rm exp})^2 + b(t - t_{\rm exp})^3$, where $t_{\rm exp}$ is the date of zero flux. This approximately matches the so-called "expanding fireball" model of early SN Ia flux from Arnett (1982), which predicted a parabolic rise, and which was experimentally verified by the earliest data of SN 2011fe (Nugent et al. 2011). Our `SiFTO` templates only cover $UBVgri$ data, so we cannot use Swift data bluer than U. However, these near-UV data are often severely overpredicted by our analytic model with its grey opacity and lack of UV-reprocessing in the ejecta (see e.g. Hosseinzadeh et al. 2017, 2022), so we would most likely exclude those data even if we could them.

The companion shocking component is used in the form of the corrected analytic approximations from Kasen (2010) (Equations 22 and 25) included in Hosseinzadeh et al.

(2017) (Equations 1 and 2), reproduced here:

$$R_{\rm phot} = (2700\ {\rm R}_\odot) x^{1/9} \kappa^{1/9} t^{7/9} \tag{3.1}$$

$$T_{eff} = (25000\ {\rm K}) a^{1/4} x^{1/144} \kappa^{-35/144} t^{-37/72} \tag{3.2}$$

where a is the binary separation (in units of 10^{13} cm $\approx$ 144 $\rm R_\odot$), κ is the opacity (in units of the electron scattering opacity, we set $\kappa = 1$), t is the time since explosions (in days), and x is a quantity consisting of the ejecta mass and speed:

$$x \equiv \left(\frac{M}{\rm M_{Ch}}\right)\left(\frac{v}{10000\ {\rm km\ s^{-1}}}\right)^7 \tag{3.3}$$

where M is the ejecta mass, $\rm M_{Ch}$ is the Chandrasekhar mass, and v represents a transition velocity in the original model's ejecta between inner (high-density) and outer (low-density) ejecta.

The above radius and temperature are combined to form a blackbody luminosity component representing the companion-shocked ejecta. As Kasen (2010) showed, this luminosity is highly dependent on viewing angle due to the inherently asymmetric conditions of the ejecta–companion collision. Following the semi-analytic form of Brown et al. (2012a), we include a multiplicative factor on the luminosity of the companion interaction component of the form

$$f = (0.5\cos\theta + 0.5) \times \left(0.14\theta^2 - 0.4\theta + 1\right) \tag{3.4}$$

where θ is the viewing angle in radians. This factor is bound between 1 ($\theta = 0$, perfectly aligned observer and shock) and 0 ($\theta = \pi$, perfectly misaligned).

Because the x parameter influences the temperature extremely weakly (i.e. primarily only affects the luminosity of the shock component, and therefore is highly covariant with

viewing angle) and because the relevant velocity is not an easily measured physical value, we set x to its fiducial value of 1 (in order-of-magnitude agreement with the best-fit value in e.g. Hosseinzadeh et al. 2017). This results in a total of 8 parameters:

1. a, the companion separation of the shock component
2. $t_{\max}$, the time of B-band maximum light for the stretch component
3. s, the stretch applied to the stretch component
4. r_r, a factor on the r-band flux of the stretch component
5. r_i, a factor on the i-band flux of the stretch component
6. Δt_U, a shift on the time of U-band maximum for the stretch component
7. θ, the viewing angle (which determines a multiplicative factor on the shock component as shown in Equation 3.4)
8. σ, a multiplicative factor on the errors of the data to account for error underestimation.

As described in Hosseinzadeh et al. (2017), the r_r and r_i factors are included because the combination of luminosity decrease and temperature decrease of the shock component results in a non-negligible amount of shock flux in redder filters even out to peak brightness, even though the primary signature of companion interaction is an early UV excess. As in Hosseinzadeh et al. (2022), which used similar models to fit the data of SN 2021aefx (another SN Ia with an early excess), we find that fits are improved by temporally shifting the U-band component of the stretch template, which could reflect the fact that SNe Ia are less homogeneous in the UV (see e.g. Milne et al. 2013). The Δt_U parameter is reported as the shift (in days) applied to the U-band component.

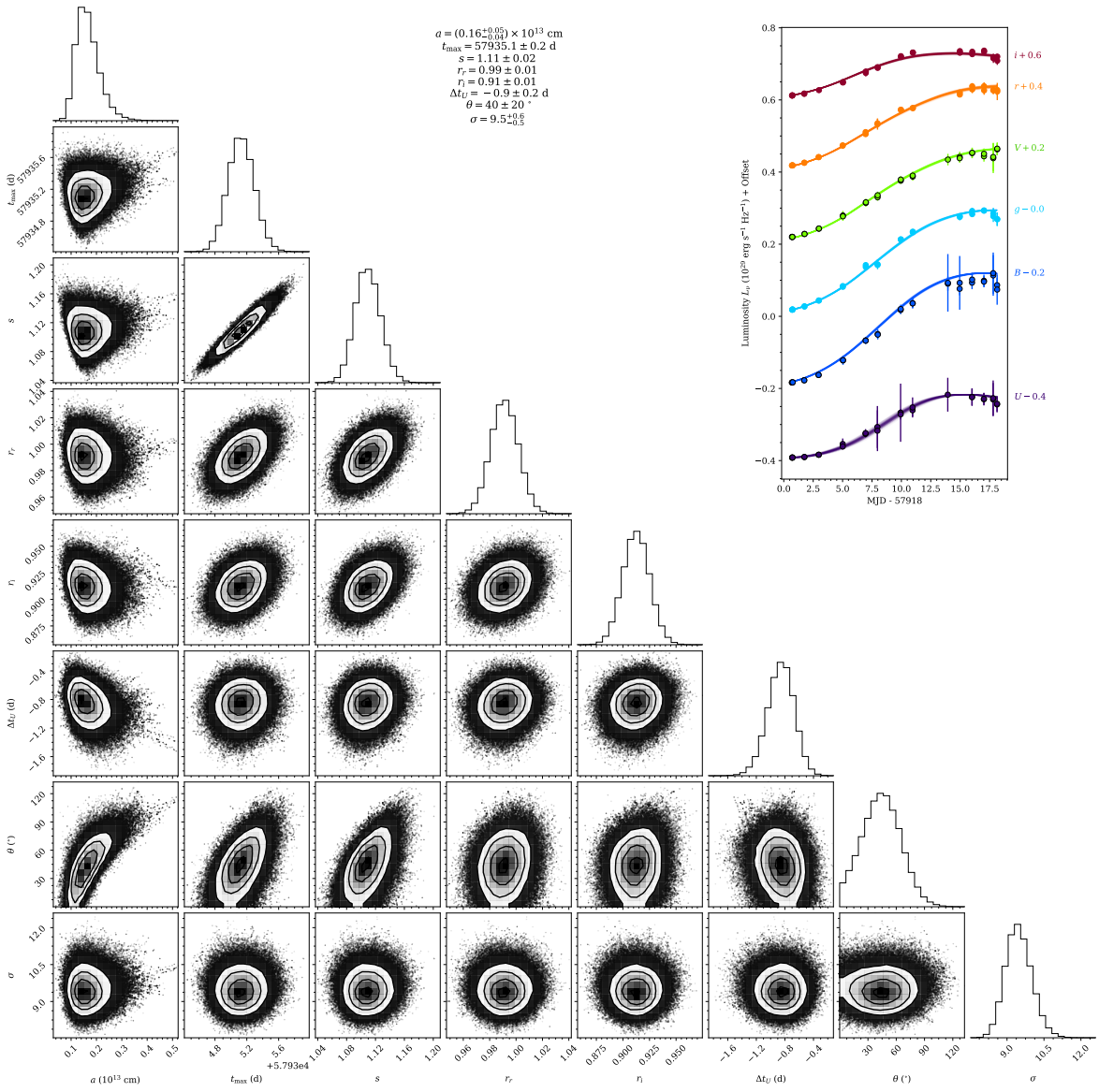

Figure 3.2: Corner plot of the model described in Section 3.4.1 for SN 2017erp. Errors in the inset lightcurve have been multiplied by the best-fit value of the σ parameter.

Additionally, the model implicitly measures the rise times of the objects. Since the rise time of the template (from time of first light to B-band maximum) is 17.19 days, the rise time of an object fit by this model is simply that value multiplied by its measured stretch.

Different versions of this model have been used to fit objects with obvious early excesses (e.g. SN 2017cbv in Hosseinzadeh et al. 2017; SN 2018oh in Dimitriadis et al. 2019a; SN 2019yvq in Burke et al. 2021 and Miller et al. 2020a; SN 2021aefx in Hosseinzadeh et al. 2022), but including the viewing angle as a parameter allows us to self-consistently fit all objects, regardless of whether or not they have an early excess (since those without an excess will converge to high viewing angles). Figure 3.2 shows the corner plot of the fit for SN 2017erp, an object that has been previously noticed to have a weak early excess (Jiang et al. 2018). As expected, due to the weak excess the model converges to a slightly off-axis shock ($\theta = 40 \pm 20°$).

SN	a ($R_\odot$)	t_{max} (MJD)	s	r_r	r_i	Δt_U (days)	θ (°)	σ
2017cbv	$55.2^{+4.7}_{-4.2}$	$57840.32^{+0.10}_{-0.10}$	$1.077^{+0.006}_{-0.006}$	$0.952^{+0.011}_{-0.011}$	$0.866^{+0.012}_{-0.011}$	$-0.83^{+0.08}_{-0.08}$	34^{+5}_{-5}	$12.57^{+0.44}_{-0.42}$
2017cyy	98.2^{+67}_{-38}	$57870.99^{+0.20}_{-0.22}$	$1.044^{+0.021}_{-0.026}$	$1.029^{+0.019}_{-0.019}$	$0.857^{+0.024}_{-0.025}$	$-0.37^{+0.21}_{-0.22}$	94^{+24}_{-29}	$8.92^{+0.54}_{-0.48}$
2017erp	$23.1^{+7.3}_{-5.4}$	$57935.13^{+0.17}_{-0.16}$	$1.109^{+0.018}_{-0.017}$	$0.991^{+0.010}_{-0.010}$	$0.912^{+0.013}_{-0.013}$	$-0.85^{+0.18}_{-0.19}$	44^{+20}_{-21}	$9.45^{+0.56}_{-0.50}$
2017fgc	390^{+650}_{-350}	$57959.81^{+0.21}_{-0.21}$	$1.078^{+0.017}_{-0.017}$	$0.983^{+0.013}_{-0.014}$	$0.966^{+0.015}_{-0.015}$	$0.35^{+0.09}_{-0.09}$	176^{+3}_{-8}	$3.45^{+0.30}_{-0.26}$
2018gv	400^{+680}_{-390}	$58149.13^{+0.05}_{-0.05}$	$0.995^{+0.004}_{-0.004}$	$1.008^{+0.006}_{-0.006}$	$0.979^{+0.009}_{-0.009}$	$-0.26^{+0.03}_{-0.03}$	177^{+2}_{-8}	$7.00^{+0.29}_{-0.26}$
2018xx	140^{+690}_{-130}	$58183.78^{+0.06}_{-0.06}$	$0.904^{+0.005}_{-0.007}$	$1.074^{+0.008}_{-0.007}$	$0.949^{+0.008}_{-0.009}$	$-0.32^{+0.06}_{-0.06}$	171^{+7}_{-47}	$5.19^{+0.24}_{-0.23}$
2018yu	$28.9^{+8.6}_{-6.9}$	$58194.20^{+0.12}_{-0.11}$	$1.008^{+0.012}_{-0.012}$	$0.939^{+0.008}_{-0.008}$	$0.885^{+0.008}_{-0.008}$	$-0.78^{+0.05}_{-0.05}$	59^{+14}_{-15}	$4.36^{+0.21}_{-0.20}$
2018aoz	$8.18^{+4.7}_{-3.2}$	$58221.76^{+0.06}_{-0.06}$	$0.878^{+0.007}_{-0.007}$	$0.959^{+0.006}_{-0.006}$	$0.962^{+0.008}_{-0.008}$	$-0.05^{+0.04}_{-0.04}$	67^{+25}_{-30}	$3.52^{+0.16}_{-0.15}$
2019np	890^{+370}_{-410}	$58510.18^{+0.14}_{-0.16}$	$1.073^{+0.011}_{-0.015}$	$0.933^{+0.011}_{-0.012}$	$0.882^{+0.013}_{-0.014}$	$-1.32^{+0.24}_{-0.25}$	150^{+4}_{-7}	$5.78^{+0.42}_{-0.39}$

Table 3.3: Best-fit parameters for the models described in Section 3.4.1. We have bolded object names where we confidently identify an early excess arising from a companion shocking interaction. Due to the nature of the models, the rise times of these objects are directly related to the stretch: $t_{\rm rise} = s \times 17.19$ days (the rise time of the template). As noted in the text, the companion separations of objects with no detectable excesses (i.e. high viewing angles) are extremely poorly constrained and essentially just reflect our priors, so their best-fit values should not be taken as physical truth.

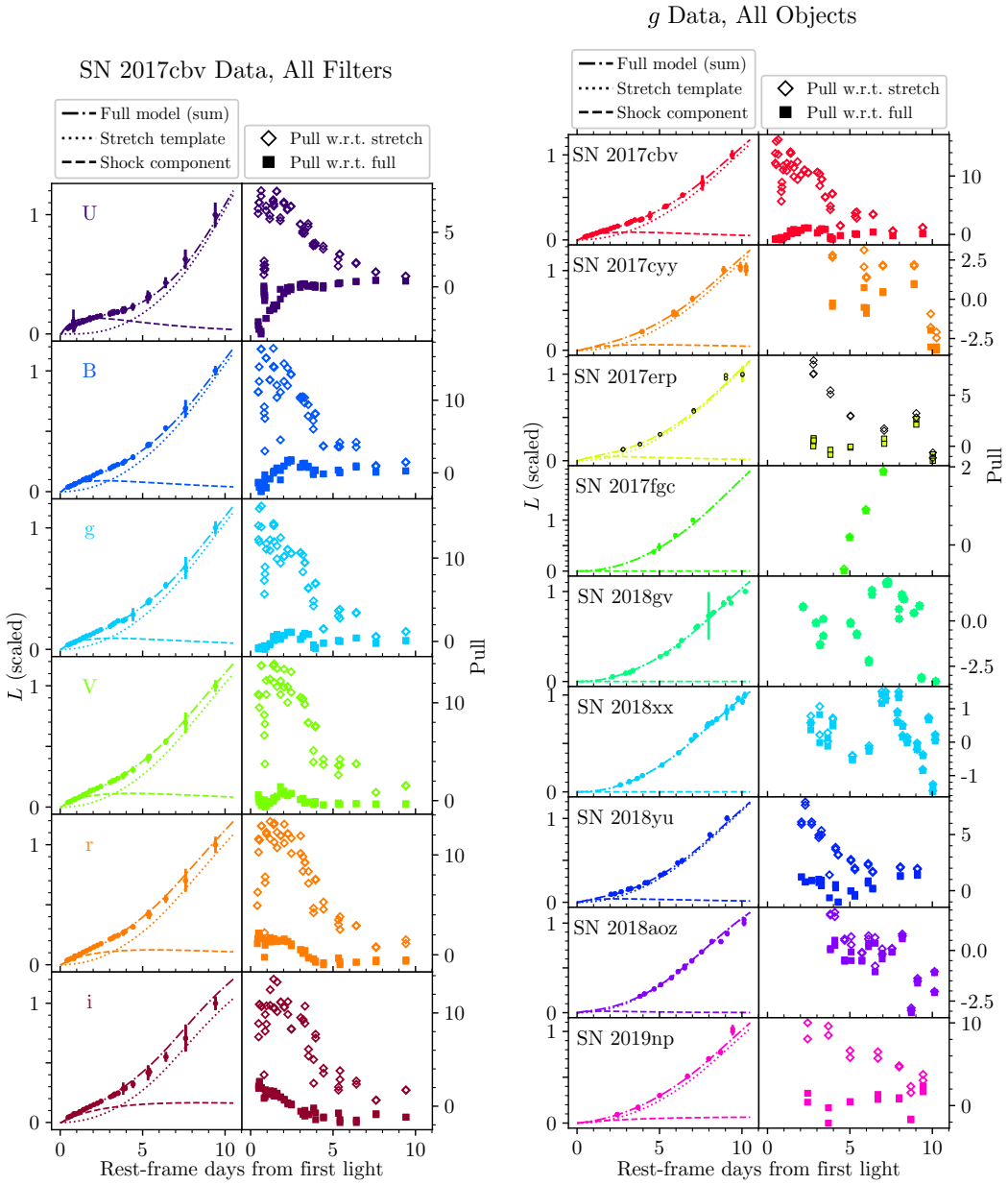

Figure 3.3: Fits and residuals for the models described in Section 3.4.1 The left panel shows all filters for one object, SN 2017cbv. The residuals are plotted both with respect to the full model (squares) and with respect to just the stretched template (diamonds), to visualize the strength of the early excess. Residuals are plotted as the normalized "pull," defined as $(L_{\rm data} - L_{\rm model})/(\sigma_{\rm data} \times \sigma)$ (i.e. number of corrected standard deviations away from the model, with σ being the best-fit value in Table 3.3). The right panel shows the same style of plot but looking in one filter (g) across all objects. The variety of early behavior is apparent in the strengths and durations of the discrepancy between the two sets of pulls.

Best-fit parameters

Table 3.3 lists the best-fit parameters for all objects in the sample. We identify objects as having an early excess based on three criteria: if we have data within five days of first light, the typical epochs for early excesses in Kasen (2010) (this criterion is necessary but does not exclude any objects in this sample); if the best-fit viewing angle is less than 90°; and if the g residuals with respect to the stretch template (see Figure 3.3) show a clear systematic, decreasing from $> 5\sigma$ at the earliest epochs to being consistent with the stretch template >10 days after explosion. We choose g for our main comparison because systematics in the residuals arising from a simplified temperature evolution (discussed in more detail soon) are minimized in this band, allowing the cleanest comparison with the model. We identify three objects (in bold) which have an early excess: SN 2017cbv (excess modeled in Hosseinzadeh et al. 2017), SN 2017erp (excess noted in Jiang et al. 2018 but modeled here for the first time), and SN 2018yu (excess modeled here for the first time). The other objects converge to viewing angles which are too high to confidently model the progenitor system (e.g. SNe 2017fgc and 2018gv, which have $\theta > 170°$, resulting in uncertainties on the companion separation of $>100 R_\odot$), or have residuals which do not show the systematic behavior expected from a fading shock component (SNe 2017cyy and 2018aoz).

SN 2018aoz is also the subject of study in Ni et al. (2022a), where data earlier than presented here show an early red bump, as opposed to the early blue bump expected from these models. Ni et al. (2022a) attribute this behavior to absorption from Fe-group elements in the outer ejecta, further proof that extremely early data (in this case within 12.4 hr of first light) can reveal key clues to the progenitor systems of SNe Ia. SN 2019np was also modeled in Sai et al. (2022), which noted unusual early behavior and attributed it to Ni mixing. The residuals of SN 2019np do show behavior partly consistent

with other early-bump objects, starting off with a $> 5\sigma$ discrepancy with respect to the stretch template at the earliest epochs and decreasing over time, but the timescale of this behavior is significantly longer than for the other three objects with early bumps, lasting $\sim$10 days instead of the more expected $\sim$5 days. The best-fit parameters of this object are unusual, with a highly off-axis explosion coupled with the largest best-fit companion separation in the sample. Due to its unusual place in parameter space we do not confidently claim it as having an early bump arising from companion interaction.

Figure 3.3 show the fits and residuals of these models. As stated earlier, the models consist of a stretched template (dotted lines) and the shock component (dashed lines). These are added together to the full model (dash-dotted lines). The left panels show the model and its components compared to the data. The right panels show the residuals of the model, both with respect to the full model (squares) and with respect to just the stretch component (diamonds). Ideally the squares should cluster around 0 and the diamonds should show the strength of any deviation from the stretched template.

The left half of Figure 3.3 shows the fits for a single object (SN 2017cbv, which has the clearest early excess) across all available filters. In most filters the early lightcurve shows a clear deviation of more than 10σ from the stretch template. Even though the Δt_U parameter is small (average value of -0.33 days across the sample), the fits show why it is necessary: without the temporal shift the stretch template overpredicts the data at most epochs even without an additional shock component. This is possibly explained by the fact that SNe Ia show more diversity in the UV than they do in the optical (Ellis et al. 2008; Milne et al. 2013; Foley et al. 2016; Brown et al. 2017), making the construction of an accurate and universal U-band $s = 1$ template more difficult. In fact no $s = 1$ template exists for the Swift filters bluer than U, which is why they are excluded from these fits. However, even including Δt_U the full model still displays systematics at the earliest times: the red bands start off overpredicted and slope to zero pull, while

the bluer bands start off underpredicted. This is indicative of inaccurate temperature evolution: immediately post-explosion the predicted temperature is too high, resulting in too much flux in the bluer bands. This can be explained by the fact that the models are an analytic approximation: note that in Equation 3.2, $T \propto t^{-37/72}$, i.e. $T(t = 0) = \infty$. This is clearly unphysical and results in the inaccurate temperature effects seen above, but still represents the start of the art for SN Ia companion shocking models more than a decade after the publication of Kasen (2010), which is the origin of these models. As discussed in Hosseinzadeh et al. (2017) these models make several simplifications, such as representing the shock flux as a pure blackbody component, with the spherically symmetric ejecta having a grey, non-time-varying opacity and a simplified density profile. We attempt to capture the clearly non-spherically-symmetric nature of the explosion with the viewing angle parameter from Brown et al. (2012a), although its semi-analytic formulation is a simplification as well. A more realistic model which includes the line-blanketing ejecta reprocessing the shock flux is needed to resolve the systematics which are present in Figure 3.3 and which will continue to be present in the future as more SNe Ia with early excesses are discovered. We strongly encourage the development of such models even though they will be more computationally expensive than the purely analytic formulation here.

The right half of Figure 3.3 shows the fits and residuals for all objects in a single filter (g). The residual plots show a variety of behavior, from SN 2017cbv's 15σ discrepancy between model components to SN 2017fgc showing effectively no excess at all. The residuals with respect to the stretch template for all objects are also plotted in Figure 3.4, for easier comparison.

For one last point of comparison with the best-fit parameters, the companion separations of SN Ia progenitor systems can be inferred for different types of systems, as was done in Liu et al. (2015). That paper used binary evolution models to estimate

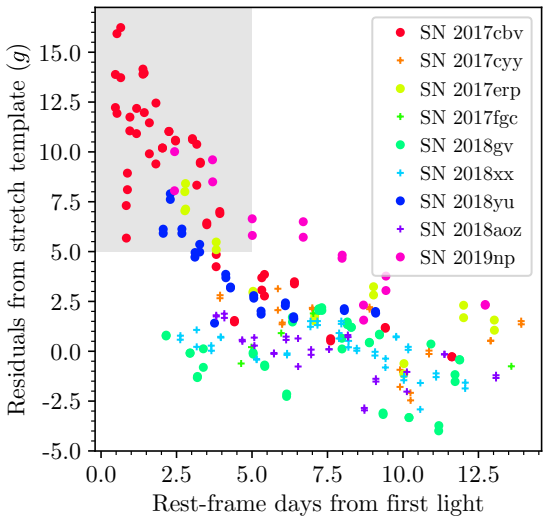

Figure 3.4: The same residuals (with respect to the stretch template, g-band) as in Figure 3.3, overplotted together to more easily compare between different objects. We identify objects with residuals in the grey box (earlier than 5 days from first light, stronger than 5σ) as having an early excess, except for SN 2019np for reasons discussed in the text.

companion separations for single-degenerate SN Ia progenitor systems in cases where the donor star is a He star, a main sequence (MS) star, or a red giant (RG). We compare their predictions with our best-fit companion separations in Figure 3.5, where we plot the posterior probability distributions for that parameter in the top panel. The maximum predicted separation in Liu et al. (2015) is 55.8 $R_\odot$, consistent with the best-fit value for SN 2017cbv ($55.2^{+4.7}_{-4.2}$ $R_\odot$). The difficulty in accurately modeling binary stellar evolution makes us question whether the upper limit in Liu et al. (2015) is a strict limit: Kasen (2010) used companion separations of 29 $R_\odot$ (2×10^{12}cm) for a 6 $M_\odot$ main sequence companion (a companion separation firmly in the red giant distribution of Liu et al. 2015) and a separation of 290 $R_\odot$ (2×10^{13}cm) for a red giant companion (well outside the red giant range plotted in Figure 3.5). The best-fit companion separations for the objects with early excesses are consistent with red giant companions (according to Liu et al. 2015), although SNe 2017erp and 2018yu do have values similar to the separation for a

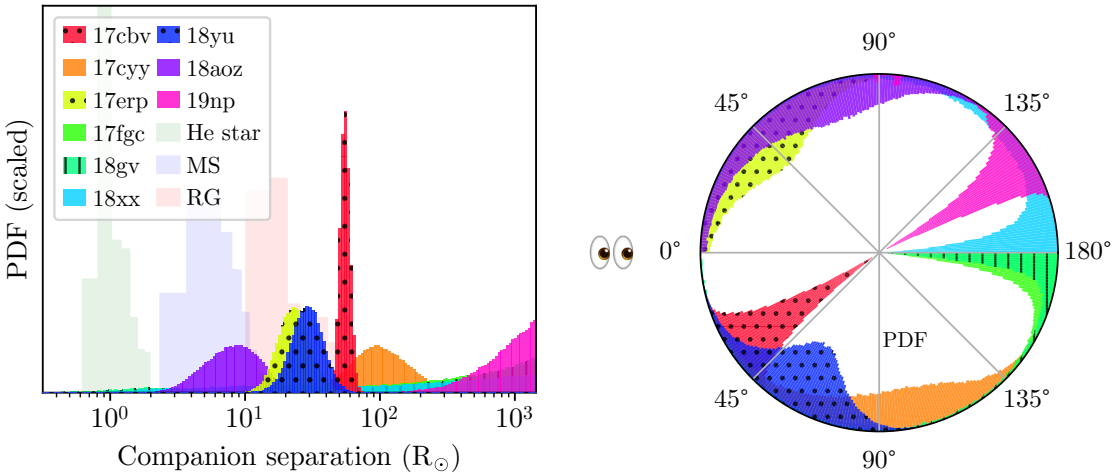

Figure 3.5: Posteriors for the a and θ parameters from the fits described in Section 3.4.1. The three objects with early excesses (SNe 2017cbv, 2017erp, and 2018yu) are emphasized with a dotted hatch. SN 2018gv also has a hatch, to distinguish itself from SN 2017fgc since the two have such similar posteriors. We have included predictions for the companion separations from different classes of donor stars (He star, main sequence, or red giant) from Liu et al. (2015). The top and bottom half of the viewing angle plot are equivalent, and objects are placed in different halves solely to minimize overlaps between posteriors.

main sequence companion used in Kasen (2010). For the objects which have converged to extremely off-axis systems, the posterior distributions for their companion separations are essentially flat in linear space. This means the prior has essentially not been modified, and the "best-fit" values listed in Table 3.3 only represent our priors and not physical parameters of the systems. The posteriors only appear peaked to high separation in Figure 3.5 because the bins are logarithmic to more easily distinguish objects.

We also include the posteriors for the viewing angle in the bottom panel of Figure 3.5. The plot is oriented to physically replicate the viewing angles with respect to the observer (represented by the eyes). Objects with no detectable excesses have converged to high viewing angles, with multiple objects having a maximum likelihood at $\theta = 180°$.

The cumulative distribution function (CDF) is plotted in Figure 3.6 and compared with the expected distribution (a sine function) if all SNe Ia arose from Roche-lobe-

overflowing single-degenerate systems. Comparing the two CDFs with a Kolmogorov-Smirnov test yields a p-value of 0.40. However, as is clear in Figures 3.5 and 3.6, objects with no detectable early excess have typically converged to a totally off-axis explosion, with multiple objects having $\theta = 180°$ as the maximum likelihood. The reason for this is clear when looking at Figure 3.7, which simply plots Equation 3.4 (the multiplicative factor on the shock flux as a function of viewing angle). The function is non-linear, making it extremely hard to distinguish between highly off-axis shocks: at $\theta = 135°$ the signal from the shock will be below the detection limit, and will be functionally indistinguishable from a perfectly misaligned system. Therefore we report two p-values on Figure 3.6: the formal p-value across the whole distribution, and also the p-value calculated using $0° < \theta < 90°$, i.e. the viewing angle range which we can reasonably hope to distinguish given the quality of our data. Using this second p-value (i.e. using the value calculated from parameter ranges which we believe are meaningful since they result in detectable and distinguishable signals), the two distributions are consistent at the $p = 0.94$ level. We find no statistical evidence for a preferred viewing angle, which might indicate a contribution from a different model for the early excess. There is not enough evidence to reject the null hypothesis, which is that SNe Ia predominantly arise in single-degenerate systems. This claim will be tested more robustly with larger samples of SNe Ia.

Despite the fact that we only find three early excesses in our sample, we fit all objects with the same set of models for the sake of consistency. Across the literature there is a wide variety of methodologies used in fitting the rising lightcurves of SNe Ia, which we will address in a future work (Burke et al. 2022, in prep.).

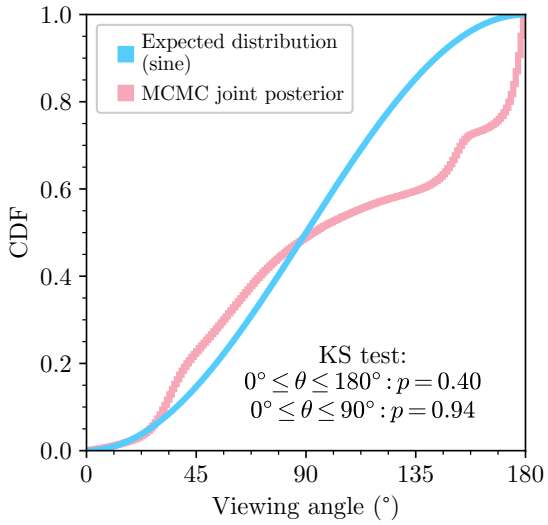

Figure 3.6: The CDF of viewing angle posteriors compared with the expected distribution. There is not enough evidence to reject the null hypothesis that SNe Ia predominantly arise in single-degenerate systems.

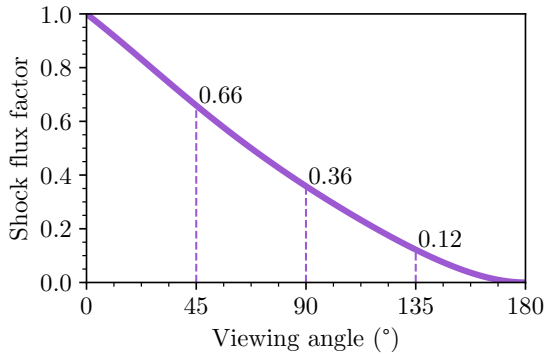

Figure 3.7: The multiplicative factor on the companion interaction shock flux, i.e. Equation 3.4, originally from Brown et al. (2012a). Shock flux is extremely diminished for $\theta > 135°$, which could explain why multiple objects converge to $\theta = 180°$ when no obvious excess is detected (see Figure 3.5), leading to the largest discrepancy between the expected and measured distributions (see Figure 3.6).

Early excess rate

Three of the objects in our sample display an early excess. Assuming simple Poissonian errors, this corresponds to an early excess rate of $33 \pm 19\%$. Our data for all objects

in this sample are early enough that we believe we would recover excesses for any object that had one which lasted on the timescale of ≈5 days, as expected from Kasen (2010).

Our value is consistent with other estimates for the rate of early excesses in SNe Ia, such as Deckers et al. (2022) (early excess rate of $18 \pm 11\%$) and Magee et al. (2020) (rate of ∼22%, 5 out of 23 SNe), even though these studies do not adopt the same null hypothesis as we do (single-degenerate systems with companion interaction). Jiang et al. (2018) find a rate of 100% in 91T-like/99aa-like SNe Ia, based on six out of six overluminous SNe Ia with early excesses. Due to a lack of 91T-like SNe Ia in our sample we cannot confirm this claim, although out of the four brightest objects in our sample three of them have an early excess. It is possible that early excesses preferentially occur in bright SNe Ia, but larger samples including 91T-like SNe Ia are needed to thoroughly test that claim.

Rise times

The models described above can also be used to measure rise times for the objects in our sample. We extrapolate the models to the time of first light, defined as the time when photons can first diffuse out of the SN ejecta (i.e. when the SN is first visible, which is not necessarily identical to when it exploded, see Piro & Nakar 2013). The time of first light is directly related to the inferred stretch: since the stretch template has a rise time of 17.19 days, the rise time is simply $t_{\rm rise} = s \times 17.19$ days. Combining this with the $t_{\rm max}$ parameter results in the MJD of first light.

The average rise time of our sample is 16.81 ± 1.26 days. Stretch-correcting this (i.e. using the stretch for the full lightcurve, listed in Table 3.1, not the stretch inferred from the rising lightcurve) yields a consistent value with smaller variance: 17.17 ± 0.86 days. These values are consistent with some recent measurements from the literature: González-Gaitán et al. (2012) find an average rise time of $17.02^{+0.18}_{-0.28}$ days and Papadogiannakis et al.

(2019) find an average of $16.8^{+0.6}_{-0.5}$ days. However these values are mildly inconsistent with other reported average rise times, such as those from Firth et al. (2015) (average of 18.98 ± 0.54 days) or Miller et al. (2020b) (average of 18.9 days, although with a range for individual obejcts from 15 to 22 days).

We again note a wide range of methodologies used to measure the rise times of SNe Ia, which we will discuss in more detail in a later work (Burke et al. 2022, in prep.).

Early spectra

As a final point of comparison for these models, early spectra can be used to test their predictions. The models directly predict that, for SNe Ia with early excesses, their early flux should be dominated by a blackbody shock component. Although it is beyond the scope of this paper, this prediction has been tested for some objects with early excesses, where it does appear that their early spectra are diluted with a blackbody component. So far this has been rigorously tested for SN 2012cg (Marion et al. 2016) and SN 2019yvq (Burke et al. 2021), and it was also implied (although not strictly modeled) for SN 2017cbv Hosseinzadeh et al. (2017).

3.4.2 Model Grids

We also compare our lightcurves to two different model grids: the double detonation models of Polin et al. (2019) and the Ni distribution models of Magee et al. (2020). We use the same epoch range as in Section 3.4.1, i.e. all data earlier than $t_{\rm max} + 5$ days. This tests if the models can reproduce the rise time and peak magnitudes across multiple filters, while still weighting the earlier data more than if we included the full lightcurve.

Double detonation

In the Polin et al. (2019) models, the explosion mechanism is as follows: a layer of He is built up on the surface of a sub-Chandrasekhar mass WD (mass range 0.6–1.3 $M_\odot$). This shell is then detonated at a range of masses (0.01–0.1 $M_\odot$). As the He shell detonates this drives a shock into the WD which causes it to detonate. This can produce SNe Ia at a range of absolute magnitudes, from dimmer than -15 to brighter than -19, and also with a range of potentially bumpy behavior at early times.

The model grid consists of 43 models, with the parameter ranges described above. For each SN in our sample we correct the data to the distance modulus, extinction, and time of first light detailed in Sections 3.3 and 3.4.1. We compare the lightcurve of each object to each model across all available filters ($UBVgri$), using a simple reduced χ^2 metric to score each comparison. Best-fit models are listed in Table 3.4.

As seen in the table, many of our objects converge to a narrow range of best-fit parameters, (the most massive WDs with the least massive He shell, which are representative of the most "normal" models in the grid). Indeed multiple objects converge to the exact same model. We attribute this partially to the coarseness of the model grid: although one benefit of this model grid is that it provides a uniform scenario which can generate a wide range of SNe Ia behavior with only two parameters (WD mass and He shell mass), a downside is that in the parameter space describing normal SNe Ia it is not finely sampled enough to discriminate between objects in this sample.

The best-fit double-detonation model for SN 2017cbv is plotted alongside its data in Figure 3.8 as the dashed line. This object is again chosen because it displays the strongest early excess in the sample, and thus makes a good test for the model grids' flexibility. In magnitude space, the model does indeed have a bump of similar strength and duration to the one seen in SN 2017cbv, and it provides a close match to i-band data throughout.

SN	Double-det	Ni mixing
2017cbv	1.1, 0.05	EXP_Ni0.8_KE2.18_P3
2017cyy	1.1, 0.01	DPL_Ni0.8_KE1.81_P3
2017erp	1.2, 0.01	DPL_Ni0.8_KE1.68_P3
2017fgc	1.1, 0.01	DPL_Ni0.8_KE0.65_P3
2018gv	1.1, 0.01	DPL_Ni0.8_KE1.68_P3
2018xx	1.1, 0.01	DPL_Ni0.8_KE1.81_P3
2018yu	1.2, 0.01	DPL_Ni0.8_KE1.68_P3
2018aoz	1.1, 0.01	DPL_Ni0.8_KE1.68_P3
2019np	1.1, 0.01	DPL_Ni0.8_KE1.68_P3

Table 3.4: Best-fit models in the two model grids described in Section 3.4.2. For the double-detonation models we report the best-fit models as a tuple of WD mass in $M_\odot$, He layer mass in $M_\odot$. We use the same shorthand as Magee et al. (2020) for the Ni mixing models: exponential (EXP) or double power law (DPL) density profile, Ni mass in $M_\odot$ (0.4 – 0.8), KE in foe (0.50 – 2.18), and a parameter which determines the degree of mixing, ranging from 3 (most mixed) to 100 (least mixed).

The main discrepancy is that the bluer bands rise too quickly after the early excess, and extending the model out to later times shows a decline in the bluer bands which is much faster than observed in the data. This behavior is generally representative across the sample, with the bluer filters (especially U) of best-fit models peaking earlier than the data by multiple days. This could partially be alleviated by introducing a Δt_U parameter as we did for the companion shocking models, but the average shift for the sample there was 0.33 days, a small recalibration compared to the systematic shift of multiple days required for these models. The fit was done in magnitude space, but looking at the color evolution of the model in Figure 3.8, the color during the excess is closely matched (although with more evolution than is seen in the data), but past the excess the model is systematically redder than the data, with the discrepancy increasing over time.

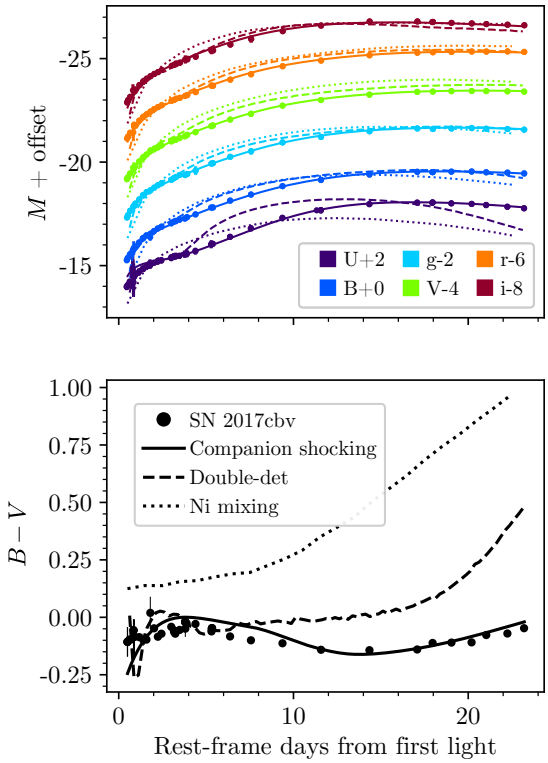

Figure 3.8: LCO data of SN 2017cbv compared with the best-fit models described in Sections 3.4.1 and 3.4.2 and listed in Tables 3.3 and 3.4. All fits were done in magnitude space (top panel), but we show them in color space ($B-V$, bottom panel) as well. The companion shocking models fit better in both cases, although the model's earliest $B-V$ colors evolve more than they are observed to do (probably due to oversimplified temperature evolution, as discussed in the text).

Ni mixing

We also look for best-fit models from the grid of 255 models provided by Magee et al. (2020). These models make use of the radiative transfer code `TURTLS` (Magee et al. 2018) and vary the density profiles, Ni masses, kinetic energy, and degree of Ni mixing to produce a range of lightcurves up to +25 days from the explosion.

Rather than finding the best-fit model with a direct χ^2 search we marginalize over parameters following the methodology of Hiramatsu et al. (2021) (see Section 4.3 and Figure 7 of that paper). As above, we do the fits in absolute magnitude space using the

parameters from Sections 3.3 and 3.4.1, and we report the results in Table 3.4. There is a similar problem to the double-detonation grid, i.e. that multiple objects converge to the same fits, in this case those with the highest Ni mass which is mixed most completely.

Again the best-fit Ni mixing model for SN 2017cbv is plotted alongside the data in Figure 3.8, as the dotted lines. As noted in Magee et al. (2020), models in this grid struggle to reproduce any early excess. A separate paper was published specifically modeling SNe 2017cbv and 2018oh (Magee & Maguire 2020), and clumps of Ni (0.02 – 0.04 $M_\odot$) in the outer ejecta were required to replicate the excesses. Indeed the best-fit model here cannot replicate the early excess, and misses the data on other counts as well (e.g. U-band peak magnitude and time of maximum are both underpredicted, V-band is systematically overpredicted, all bands rise too quickly after the epochs of the excess). In color space the model is systematically redder than the data, with the difference increasing to a full magnitude at the latest phase shown in Figure 3.8.

The fact that this model grid does not contain any early excesses is a detriment for our purposes, as it makes it difficult to accurately parametrize objects with early excesses. On the other hand, it makes it a possible diagnostic of whether or not there is an early excess: when Miller et al. (2020b) fit general power laws to the rising lightcurves of a sample of 127 SNe Ia observed with ZTF, they found no instances of early excesses. But Deckers et al. (2022), reexamining 115 SNe Ia from that sample with the model grid here, were able to recover six instances of early excesses based on quantitative measures of whether all models produced poor fits to the earliest epochs. This also shows that the statement "this SN does/does not have an early excess" can be dependent on the methodology used to characterize these excesses. We believe this is why so few objects in the literature have reported early excesses: you both need high-cadence multiwavelength data ∼3 magnitudes fainter than peak (within ∼5 days of first light), and you need a methodology able to detect and characterize these excesses, except in the extreme cases

where they are detectable by eye as they were for e.g. iPTF14atg, SN 2017cbv, SN 2019yvq, and SN 2021aefx as discussed in Section 3.1.

3.5 Color Evolution

With the extinction values measured in Section 3.3.1, we present the color evolution of the sample in Figure 3.9. We use a logarithmic time axis (from one day after first light) to distinguish any early inhomogeneities. We also include the NUV-red and -blue regions defined in Milne et al. (2013) for the appropriate filter combinations.

As can be seen in the figure, the objects in the sample are all NUV-blue with the possible exception of SN 2017erp before peak brightness (see Brown et al. 2019 which also found that the object was both reddened and intrinsically red). This is unexpected: Milne et al. (2013) found that only about a third of their sample were NUV-blue. Even calling SN 2017erp NUV-red would mean that 8 of 9 objects in this sample are NUV-blue. The probability of this happening (according to the binomial distribution) is only 0.08%. Brown et al. (2017) noted that the exact way reddening is applied can easily shift objects between NUV color groups, and even a small amount of optical reddening ($E(B-V) = 0.2$) can drastically change the UV colors of an object. Our sample, which is largely consistent with $E(B-V) = 0$ (see Table 3.1), would only get bluer if reddening were underestimated (and it could not be overestimated). This could indicate that the sample of Milne et al. (2013) were incorrectly dereddened, and that SNe Ia are actually UV-bluer than previously thought. Additionally, not only are the objects not in the NUV-red group, but a significant portion of the data earlier than +10 days from first light is bluer than the bluest edge of the expected NUV-blue population: again, SNe Ia seem UV-bluer than previously thought.

In addition to the already-known >1 magnitude scatter in the NUV colors, we also

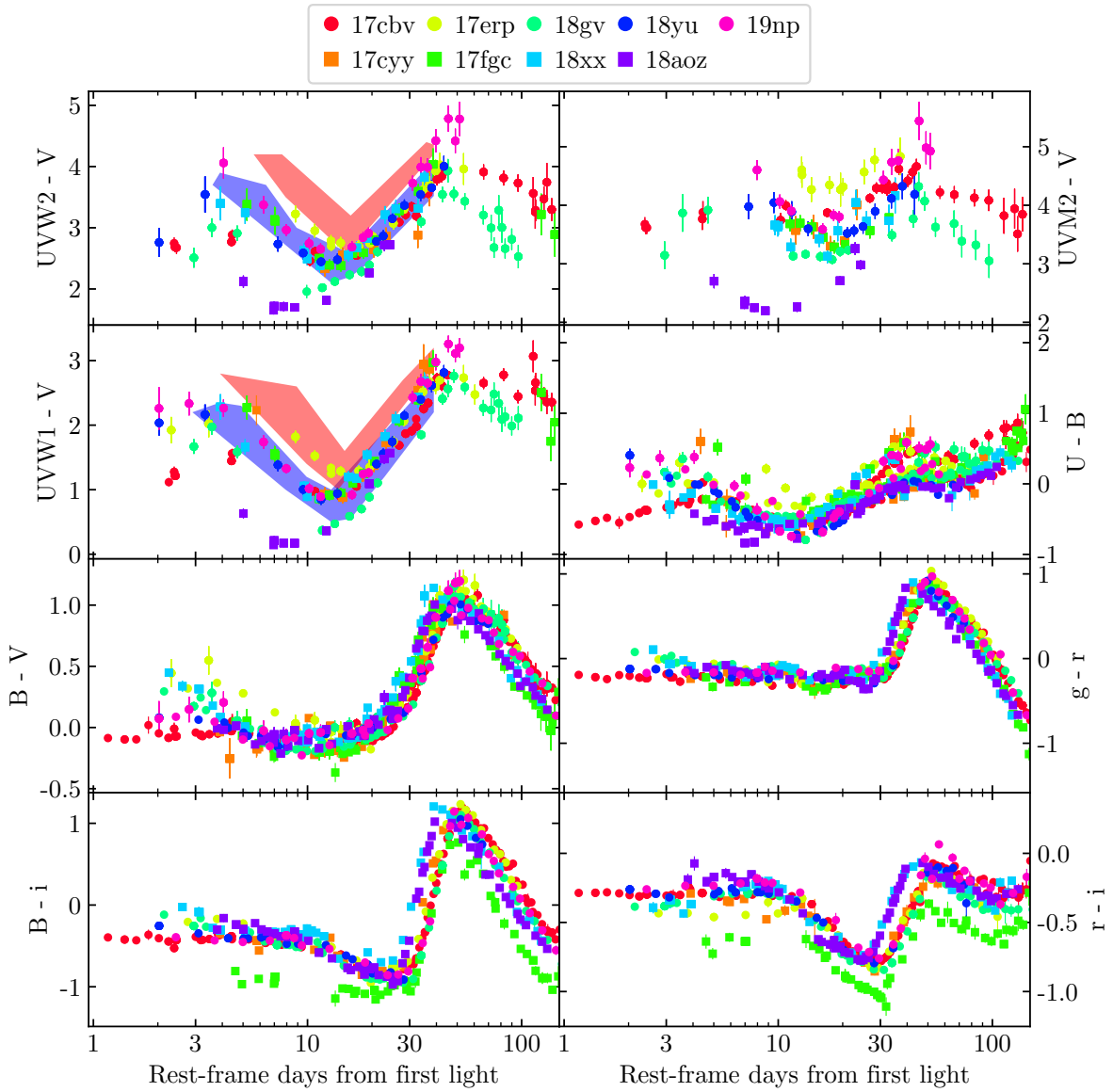

Figure 3.9: Color evolution of the sample in a number of filter combinations. Note the logarithmic scale of the time axis, to emphasize early heterogeneity while showing evolution into the nebular phase. NUV-red and -blue regions are shown for UVW2–V and UVW1–V (see Figure 4 of Milne et al. 2013), where it can be seen most objects in this sample are NUV-blue, in contrast with expectations from Milne et al. (2013).

note the range of $B - V$ colors in the first $\sim$5 days after first light. Here the object with the earliest data (SN 2017cbv) has a steady mostly unchanging blue color close to $B - V = -0.1$. This contrasts with the color evolution of the object with the next-

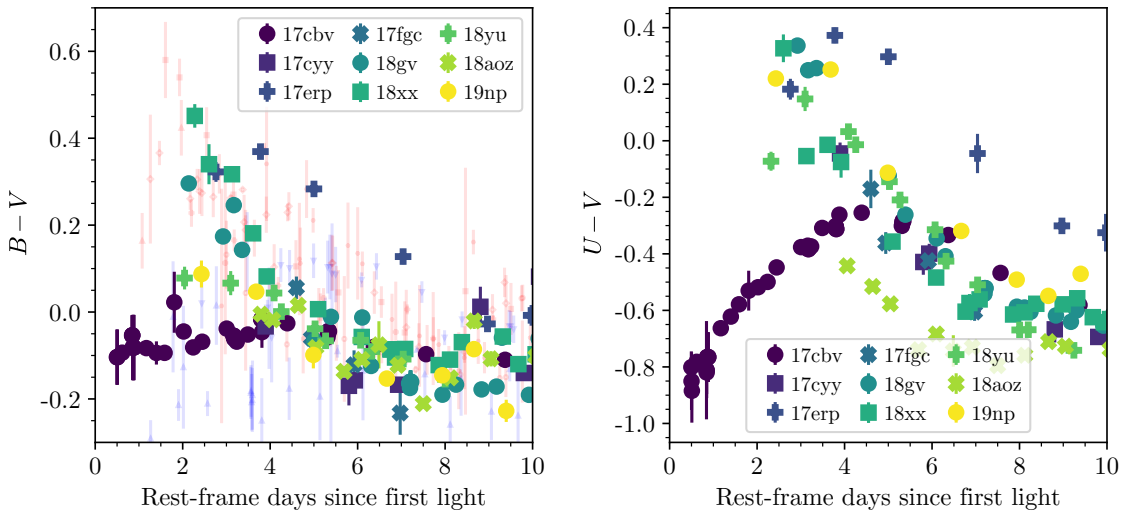

Figure 3.10: *Left:* Early $B-V$ color evolution of objects in the sample, with background red and blue data points from the objects in Stritzinger et al. (2018), colored according to their classification in Table 1 of that paper. *Right:* Early $U-V$ color evolution. Whereas most objects just show a blueward color evolution, the three objects with early excesses (SNe 2017cbv, 2017erp, and 2018yu) have an initial redward evolution from the rapid cooling of the shocked ejecta before becoming dominated by the usual blueward evolution.

earliest data (SN 2018yu), which at its earliest phase (+2.0 days) has a redder color ($B-V = 0.08 \pm 0.03$). Another object with especially good early data (SN 2018xx, +2.3 days) has significantly redder colors ($B-V = 0.45 \pm 0.03$).

The top panel of Figure 3.10 shows the early $B-V$ color evolution compared to the objects in Stritzinger et al. (2018), since that paper includes several other SNe Ia with early multiband data. Stritzinger et al. (2018) propose two distinct populations of SNe Ia given their color evolutions within ∼4 days of explosion, and we have kept this red/blue dichotomy when coloring the background points of the figure (to replicate their Figure 2). We choose a neutral colormap for our sample to avoid confirmation bias in seeing two distinct populations especially in the critical phase (earlier than 4 days after first light).

We find a range of early color behaviors, with SNe 2018yu and 2019np fitting in between the "early-blue" objects (such as SN 2017cbv) and the "early-red" objects, which

SN 2018xx matches with. Our small sample size makes it difficult for us to say with any statistical confidence whether there is a real continuum of behavior at the earliest phases, although Bulla et al. (2020) find no evidence for multiple distinct populations when examining the early $g-r$ color evolutions of a sample of 65 SNe Ia. (We refer especially to Figure 2 of that paper for comparison to the Stritzinger et al. (2018) sample, although the putative discrepant populations are more distinct in $B-V$ than in $g-r$.)

Figure 3.10 also shows the $U-V$ color evolution. We have kept the same neutral colormap to avoid confirmation bias, but most objects (e.g. SNe 2018gv, 2018aoz) show a direct blueward color evolution. SN 2017cbv shows a very clear and well-resolved initial redward color evolution before overlapping with the blueward evolution after $\approx$5 days. The other two objects with early excesses (SNe 2017erp and 2018yu) display similar redward turns between their first and second epochs, as does SN 2019np (discussed above and in Sai et al. 2022 although again we don't confidently claim it as having an early excess). These "kinks" in the color evolution are more obvious in $U-V$ than the range of early slopes in $B-V$, and presumably arise from the rapid cooling of the shocked ejecta in the early shock-dominated phase, before matching more typical color evolution in the later SN-flux–dominated regime.

We have already compared the color evolution of objects in our sample with our best-fit models in Figure 3.8 and the surrounding discussion. As stated there, we favor companion shocking models in color space in addition to magnitude space.

3.6 Discussion

As shown in the previous two sections, SNe Ia exhibit a continuum of behavior at early times. This is consistent with the single-degenerate scenario described in Kasen (2010), where this continuum is caused partly by seeing the progenitor system and its

briefly shocked ejecta at a range of viewing angles.

In general we favor the companion interaction scenario for several reasons:

1. With effectively only two physical parameters (companion separation and viewing angle) these models can reproduce a wide range of early lightcurve behavior seen in SNe Ia.

2. The number of early excesses and the distribution of their strengths (one SN with a strong excess, two SNe with weaker excesses, 6 SNe with no early excess) match their expected viewing-angle-dependent rate (see Figures 3.5 and 3.6).

3. Referring to Figure 3.5, for the three objects in our sample with early bumps the inferred companion separation lies close to the expected range from binary stellar evolution models.

4. The prediction that early spectra should appear to be diluted with a blackbody component is matched by observations (e.g. SN 2012cg in Marion et al. 2016, SN 2019yvq in Burke et al. 2021, and implied for SN 2017cbv in Hosseinzadeh et al. 2017).

5. Although not without systematic issues, companion interaction models reproduce both the magnitude and color evolution better than other classes of models (see Figures 3.8 and 3.3).

6. Lastly (and more philosophically) the models are true theoretical predictions, as this method of producing early excesses was formulated before the effect had ever been observed, meaning best-fit parameters lie close to a priori expected values without any fine-tuning needed to match observations.

As with any models there are of course imperfections:

1. These models are an analytic approximation to the full numerical grid of Kasen (2010) (including the semi-analytic viewing angle effect from Brown et al. 2012 a), and this results in certain oversimplifications such as an inaccurate temperature evolution as discussed in Section 3.4.1. The models also have a grey opacity, which means the SN ejecta do not reprocess the UV shock flux for off-axis explosions, leading to dramatic overestimates of the flux in Swift filters for multiple SNe (Hosseinzadeh et al. 2017, 2022).

2. The earliest and most interesting phase of the models relies on comparing to the $s = 1$ template at precisely the phase when it is most poorly constrained.

3. The fits for objects without early excesses (see Table 3.3 and Figure 3.5) tend to converge to perfectly misaligned systems, since the distinction between e.g. $\theta = 135°$ and $\theta = 180°$ is lost in the noise (see Figure 3.7). This limits the range of θ and thus the sample size where we can compare to the expected viewing angle distribution.

4. As discussed in Section 3.1, a nondegenerate companion is expected to leave traces of H in the nebular spectra of SNe Ia which originate from single-degenerate systems, and this signature is not detected in >100 SNe Ia (e.g. Sand et al. 2019; Tucker et al. 2020). This signature has only ever been observed in three low-luminosity SNe Ia, and notably has *not* been observed for objects with early excesses such as SN 2017cbv (Sand et al. 2018), SN 2018oh (Dimitriadis et al. 2019b; Tucker et al. 2019), SN 2021aefx (Ashall et al. 2022; Hosseinzadeh et al. 2022), or for any objects in this sample (Sand et al. 2022, in prep.). However, measuring a physical amount of stripped H ($M_{\rm H}$) relies on translating from a measured luminosity of Hα ($L_{\rm H\alpha}$), and this translation is extremely model-dependent: early models (Mattila et al. 2005) calculate a luminosity for a given $M_{\rm H}$ which is up to 10^3 times less than later

models (Botyánszki et al. 2018) calculated for the same $M_{\rm H}$. Even more recent models (Dessart et al. 2020) find variations of up to half a dex in $L_{\rm H\alpha}$ depending on the adopted model of the underlying SN ejecta, and the time-dependent nature of $L_{\rm H\alpha}$ can again cause the inferred $M_{\rm H}$ to differ by a full order of magnitude from the Botyánszki et al. (2018) models (see Sand et al. 2022, in prep.). The models of Botyánszki et al. (2018) are three-dimensional and do not assume local thermodynamic equilibrium (LTE), but make several approximations to optimize the radiative transfer calculations including using the Sobolev approximation and limiting the allowed recombination transitions; while Dessart et al. (2020) has more complete radiative transfer calculations, those models are limited to one dimension, with an "unphysical" treatment of how the stripped H is added. All this is to say: while the lack of Hα observed in the nebular spectra of most SNe Ia is seemingly in tension with our results that early excesses arise from companion interaction, the extreme range of highly model-dependent $L_{\rm H\alpha}$ predictions lessens this tension and we certainly do not take the lack of Hα as a reason to definitively reject the companion interaction scenario.

Regardless of these downsides, in the interest of having a consistent methodology for fitting the rising lightcurves of all SNe Ia regardless of whether they show signs of interaction, we have fit the objects in our sample with these companion interaction models. We generally favor them over other classes of models, especially in cases where objects show early excesses, and we find that our sample is holistically consistent with Roche-lobe-overflowing single-degenerate progenitor systems described by companion interaction models.

3.7 Conclusions

We have presented a sample of nine SNe Ia with exemplary early-time high-cadence multiwavelength followup from LCO and Swift. We have relied on other facilities for SN discovery, and the DLT40 survey with its nearby-galaxy-targeted approach enabled much of the earliest and most interesting observations presented here.

Out of the nine objects in the sample, one has a strong early excess (SN 2017cbv), two have weaker excesses (SNe 2017erp and 2018yu), and six show no excess at all. All objects are well-modeled by companion interaction models, which add an early viewing-angle-dependent shock component to a standard SN Ia template. Even for cases where these models are less successful at fitting the data (i.e. SN 2019np and the earliest data of SN 2018aoz, see Sai et al. 2022; Ni et al. 2022a), the discrepancies reveal an exciting diversity of early lightcurve behavior. The sample size is small, but the strengths of early excesses and the distribution of viewing angles are statistically consistent with SNe Ia predominantly arising from Roche-lobe-overflowing single-degenerate progenitor systems.

In addition to the companion interaction results, we also find that eight of the nine SNe are near-UV blue, in contrast to the expectation that only a third of SNe Ia are near-UV blue. We also find a seemingly continuous range of $B-V$ colors within the first five days from first light, again in contrast to earlier claims of two distinct populations based on early color evolution.

The data required to reveal unusual early lightcurve behavior and distinguish between models are extremely difficult to get: the data must be early, high cadence, and preferably multiwavelength. LCO is uniquely suited to obtain just this kind of dataset – no other ground-based optical observatory could have obtained the continuous 6-hr cadence coverage of SN 2017cbv's bump, and its rapid response allowed the most interesting data of SNe 2021aefx, 2018yu, 2017erp, and the other objects here. The uncertainties

surrounding the progenitor systems of SNe Ia will slowly decrease over time as samples such as the one presented here, with early high-cadence multiwavelength data, gradually expand, allowing for testing of the finer details and statistical predictions of a variety of models.

Chapter 4

Companion Shocking Fits to the 2018 ZTF Sample of SNe Ia Are Consistent with Single-Degenerate Progenitor Systems

This chapter is reproduced from Burke et al. (2022a) by permission of the American Astronomical Society. I would like to thank my coauthors, without whom this work would not have been possible: D. A. Howell, D. J. Sand, and G. Hosseinzadeh,

4.1 Introduction

Type Ia supernovae (SNe Ia) come from exploding white dwarfs (WDs). This statement is uncontroversial and has been understood for decades (Hoyle & Fowler 1960), but almost every detail of the progenitor system and explosion mechanism is the subject of active research. What mass are the WDs when they explode? Do they need to accrete mass up to the Chandrasekhar limit, or, as some models predict (e.g. Polin et al. 2019; Shen et al. 2021), can they explode at sub-Chandrasekhar masses? Where does the explosion start? Does it begin roughly at the center of the WD (Khokhlov 1991), or does it begin in a surface layer of accreted He which causes the underlying WD to detonate

(Polin et al. 2019)? How do the WDs gain enough mass to explode? Are they in a binary system with a Roche-lobe-overflowing nondegenerate stellar companion (referred to as the "single-degenerate" case; Hoyle & Fowler 1960), or does the primary WD tidally disrupt a less massive secondary WD (the "double-degenerate" case; Iben & Tutukov 1984)? These and many other questions have yet to be definitively answered.

SNe Ia have standardizable lightcurves, especially around peak (see e.g. Riess et al. 1998; Perlmutter et al. 1999; Phillips et al. 1999). But their early lightcurves, within a few days of explosion, are much less homogeneous and can contain observational signatures which reveal information about their progenitor systems. One such signature was predicted in Kasen (2010): in the single-degenerate case, as the SN ejecta collide with a nondegenerate companion they will get shock-heated, resulting in early UV excesses which should be observable for binaries with favorable viewing angles ($\sim$10% of events). After these early UV excesses were predicted they (or similar effects) have subsequently been observed in a small number of objects: SN 2012cg (Marion et al. 2016), iPTF14atg (Cao et al. 2015), SN 2016jhr (aka MUSSES1604D, Jiang et al. 2017), iPTF16abc (Miller et al. 2018), SN 2017cbv (Hosseinzadeh et al. 2017), SNe 2017erp and 2018yu (Burke et al. 2022b), SN 2019yvq (Miller et al. 2020a; Siebert et al. 2020; Tucker et al. 2021; Burke et al. 2021), and SN 2021aefx (Ashall et al. 2022; Hosseinzadeh et al. 2022). Some other objects have early excesses, but without the color information needed to determine their temperature, such as SN 2018oh (Li et al. 2019; Dimitriadis et al. 2019a; Shappee et al. 2019) and SN 2020hvf (Jiang et al. 2021), and still others (SN 2018aoz; Ni et al. 2022a, b) have early color evolution which can differ by more than a magnitude from a typical SN Ia.

Most of the above objects were modeled with companion interaction models, but there are other physical models which can produce early excesses. "Double-detonation" models, where the WD builds up a layer of He on its surface until the He detonates, driving a

shockwave into the WD causing it to detonate in turn, can also produce a range of early lightcurve behavior due to the presence of extra radioactive products in the outer ejecta (see Sim et al. 2012; Polin et al. 2019). Models which vary the distribution of ^{56}Ni, which powers SN Ia lightcurves (Pankey 1962), can also produce a range of early behavior, including early bumps (Magee et al. 2018; Magee & Maguire 2020; Magee et al. 2020). Both classes of models produce extra radioactive material in the outer ejecta, resulting in some similar effects (e.g. "red bumps" at early times), which makes them potentially difficult to distinguish for near-Chandrasekhar-mass WDs.

Recently, Burke et al. (2022b) examined a sample of 9 SNe Ia with exemplary high-cadence multiwavelength early data. Overall the paper favored companion interaction models to explain both objects which exhibit an early excess, and those that do not. The sample was constructed using a set of criteria to make it as unbiased as possible, and contained one object with a strong early excess and two others with weaker excesses. Based on the distributions of early excess strengths and best-fit viewing angles, that paper concluded that there was not enough evidence to disprove the null hypothesis, i.e. that all SNe Ia come from single-degenerate progenitor systems.

In this paper we will be focusing solely on companion shocking models to explain early excesses. We do not claim that the models can perfectly explain every aspect of the dataset: we refer to the discussion section of Burke et al. (2022b) for an explicit list of their pros and cons. Perhaps the strongest point against them is the lack of H observed in the nebular spectra of SNe Ia (see e.g. Sand et al. 2019; Tucker et al. 2020), even though the ejecta-companion interaction should strip H from a non-degenerate companion (Botyánszki et al. 2018; Dessart et al. 2020). They also struggle to fit UV data: even though the process of shock heating should make the early excess strongest in the UV , the models consistently overpredict the UV flux (see e.g. Hosseinzadeh et al. 2017, 2022). Keeping these caveats in mind (and again, for a more in-depth discussion we refer to

Burke et al. 2022b), we nevertheless favor the models and use them to investigate the sample of SNe Ia presented here.

This paper follows very similar methodology to Burke et al. (2022b), but applied to a different sample of SNe Ia. The sample here has an order of magnitude more objects but limited multi-band information when compared to Burke et al. (2022b), making this a complementary analysis. In Section 4.2 we briefly describe our data and sample, and in Section 4.3 we describe the companion interaction models we use to fit the data. We show and discuss the results of the fits in Section 4.4, before concluding in Section 4.5.

4.2 Data and Sample

The full dataset in this paper comes from Yao et al. (2019), so we refer to that paper for details of its acquisition and reduction. The data come from the ZTF survey (Bellm et al. 2019), and the dataset has many advantages: the large number of objects (127); the uniform inclusion of non-detections; and the high cadence of coverage, with some objects being observed not only nightly, but revisited six times per night (thrice in g and thrice in r). The primary downside of the dataset is that it is in only two filters, g and r, which strongly limits the number of filter combinations which can be used to determine color/temperature (compare e.g. the $UBVgri$ data used in Burke et al. 2022b).

To obtain the data, we simply downloaded the digital version of Table 5 of Yao et al. (2019), which is a FITS file containing the full dataset in flux space. We convert to magnitude space following Equations 7–10 of that paper.

The sample was introduced in a series of three papers: Paper I (Yao et al. 2019) described the overall data reduction method and the properties of the sample itself; Paper II (Miller et al. 2020b) modeled the rising lightcurves of the sample to infer rise times; and Paper III (Bulla et al. 2020) analyzed the sample's color evolution. Again,

we refer to Yao et al. (2019) for a full description of the sample. In short, the sample contains 127 SNe Ia. All objects have observations earlier than at least 10 rest-frame days before maximum light, and 50 of the objects have detections earlier than 14 rest-frame days before peak. The median redshift of the sample is 0.076. Though we focus on photometry here, Yao et al. (2019) also discusses the spectroscopic classifications of the objects: 107 objects are "normal" SNe Ia (including the 25 SNe listed in the paper as "normal*," i.e. tentatively classified as normal), 10 objects are 99aa-likes (including three tentative classifications), four objects are super-Chandrasekhar SNe Ia (including two tentative classifications), three are 91T-likes (including two tentative classifications), one is an 86G-like, one is an 02cx-like, and one is a Ia-CSM. We again refer to Yao et al. (2019) for details of the classifications, and also to Taubenberger (2017) for a discussion of the various different subtypes of SNe Ia.

4.3 Models

4.3.1 Initial Parameter Measurements

Following Burke et al. (2022b), we utilize the Python package `SNooPy` (Burns et al. 2011) to measure several necessary quantities for the objects. We do `SNooPy` fits using the default `EBV_model` and the `fitMCMC()` procedure, enforcing $R_{V,\mathrm{host}} = 3.1$. We impose a uniform prior on `EBVhost` ranging from 0 to 1. We limit the data to the epochs relevant for `SNooPy` models, i.e. -10 to $+50$ days from peak (using $\mathrm{MJD}_{\mathrm{peak}}$ as measured by Yao et al. 2019). We visually inspect fits to ensure that they are reasonable. We adopt the `SNooPy` values of distance moduli and host extinction for all objects throughout our analysis. We convert each object's $E(B-V)$ (Milky Way + host) to per-filter extinction values using the Schlafly & Finkbeiner (2011) recalibration of the Schlegel et al. (1998)

dust maps, accessed by the Python package `extinction` (Barbary 2016).

We also use `SNooPy` to measure K-corrections for the data, similar to Bulla et al. (2020). The way that `SNooPy` fits SN Ia lightcurves already involves K-corrections, making them straightforward to extract from the fits. This method of K-correction is the largest deviation from the methodology of Burke et al. (2022b), which otherwise this paper follows quite closely. The sample of Burke et al. (2022b) was low redshift ($z < 0.01$), so any K-correction would both be small and (as is inherent in doing K-corrections) would rely on assumptions about the underlying SED, even though those assumptions could be incorrect for objects with early excesses since their early spectra differ from SNe Ia without excesses (see e.g. Marion et al. 2016; Hosseinzadeh et al. 2017; Burke et al. 2021). Due to the much higher redshift of the sample here (median redshift 0.076) we deemed K-corrections necessary, since the models described in Section 4.3.2 rely on accurate absolute magnitudes both to compare to the rest-frame g and r template lightcurves and to compare to the strengths of any early excesses.

4.3.2 Companion Shocking Models

Description of models

Our models are similar to the ones used in Burke et al. (2022b) (along with Hosseinzadeh et al. 2017 and Hosseinzadeh et al. 2022 and to some extent those in Dimitriadis et al. 2019a and Miller et al. 2020a). They make use of the `lightcurve_fitting` Python package (Hosseinzadeh 2019), which performs MCMC fits using the `emcee` package (Foreman-Mackey et al. 2013). The model consists of two components: a template lightcurve from `SiFTO` (Conley et al. 2008) which is scaled and stretched to maximize overlap with the data, to which is added a blackbody component (which can dominate at early times) representing a companion shock interaction based on the analytical formu-

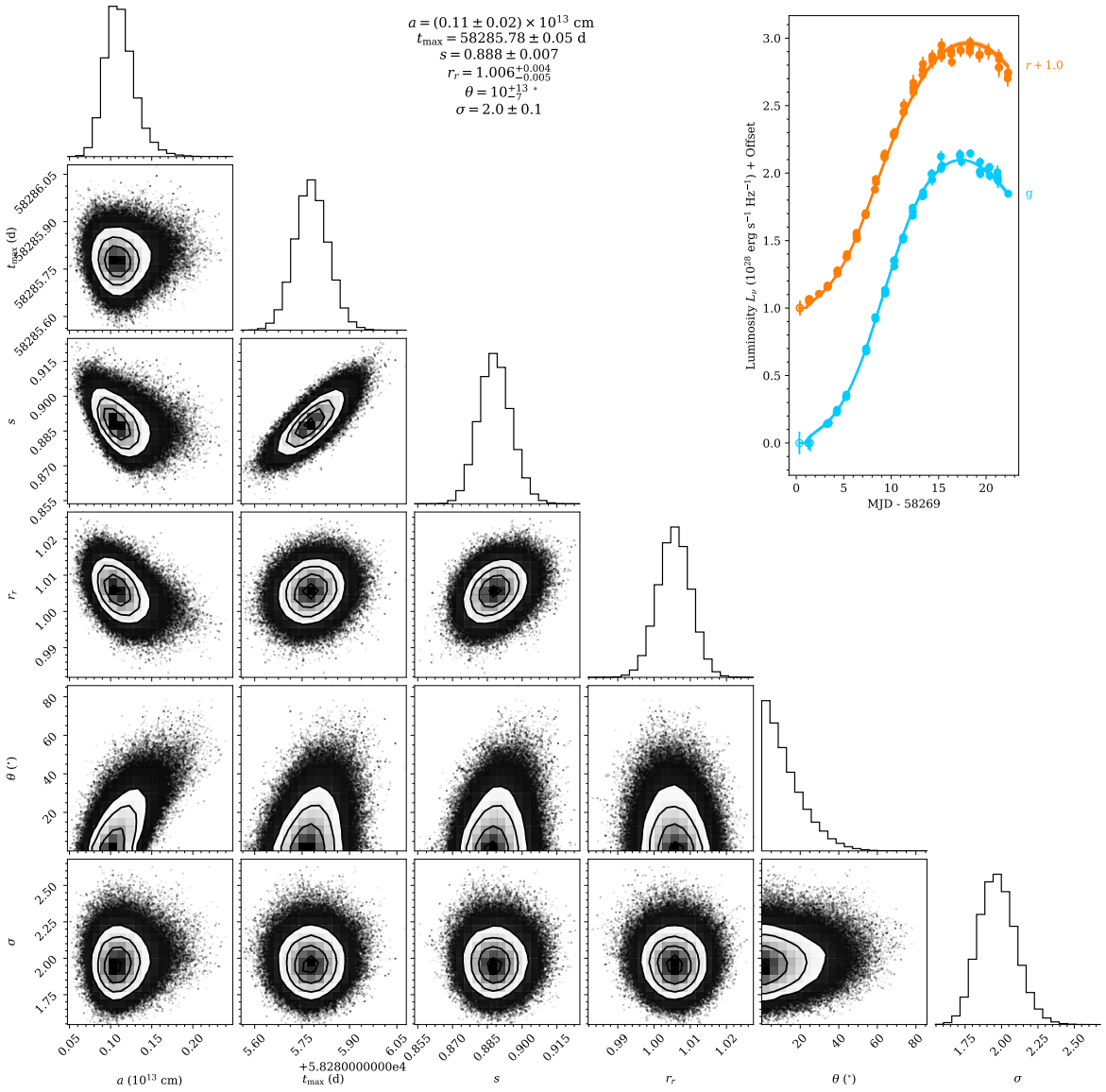

Figure 4.1: Corner plot of the model described in Section 4.3.2 for ZTF18aaxsioa, one of the objects we identify as having an early excess (see the beginning of Section 4.4.1 for early-excess selection criteria). The inset data show the extremely high cadence and useful non-detections (first epoch shown, unfilled circles) typical of the sample.

lae from Kasen (2010). As in Burke et al. (2022b) we add a parameter to represent the viewing angle, implemented as a multiplicative factor on the shock component following the semi-analytic formulation of Brown et al. (2012a).

This results in a total of six parameters:

1. a, the companion separation of the shock component
2. $t_{\max}$, the time of B-band maximum light for the stretch component
3. s, the stretch applied to the stretch component
4. r_r, a factor on the r-band flux of the stretch component
5. θ, the viewing angle (which determines a multiplicative factor on the shock component)
6. σ, a multiplicative factor on the errors of the data to account for error underestimation.

The models are identical to those used in Burke et al. (2022b), except for the fact that two parameters used in that paper are excluded because they affect only non-gr data and are thus irrelevant for the dataset here. We refer to that paper for a more detailed description of the models – the two differences here are the slightly fewer parameters and the fact that we do the fits on the K-corrected data. We also refer to the discussion section of that paper for an explicit list of the pros and cons of the model, including various simplifying assumptions it makes.

A corner plot for an object we identify as having an early excess is shown in Figure 4.1.

Is It Valid to Use Just gr Data in Companion Shocking Models?

Most of the literature using this style of modeling has access to highly multiwavelength datasets (see Burke et al. 2022b for the most direct comparison, but also Cao et al. 2015; Hosseinzadeh et al. 2017; Dimitriadis et al. 2019a; Miller et al. 2020a; Burke et al.

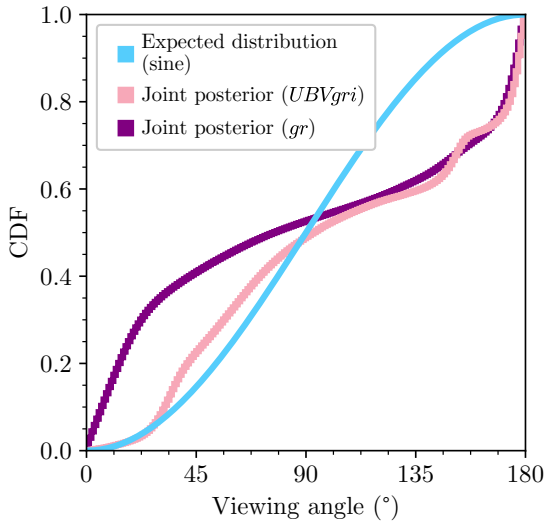

Figure 4.2: Joint viewing angle posteriors for the sample modeled in Burke et al. (2022b), which markedly change from the result presented in that paper (the pink line) when the lightcurves are limited to just gr data (the purple line). We conclude that these models can still be used to detect early excesses in gr data, as objects exhibiting early excesses converge to low viewing angles, but the models shouldn't be used to measure physical parameters. It also means that the K-S test method used in Burke et al. (2022b) is no longer applicable for gr data alone.

2021; Hosseinzadeh et al. 2022). The wavelength coverage is often $UBVgri$, but sometimes extends further into the UV with data from the Neil Gehrels Swift Observatory (Swift; Gehrels et al. 2004). The temperature of the early data, accessed through different filter/color combinations, is a critical parameter implicitly measured in the models, making it natural to ask: is it valid to use only gr data with these models?

To summarize the answer to that question: these models can still detect early excesses using only gr data, but they should not be used to measure physical parameters.

To see why this is the case, we reexamine the objects modeled in Burke et al. (2022b), limiting the data from $UBVgri$ down to gr. One result from that paper had to do with the joint MCMC posteriors of the θ parameter from the nine objects in that sample, where, when comparing the joint posterior to the expected distribution of viewing angles

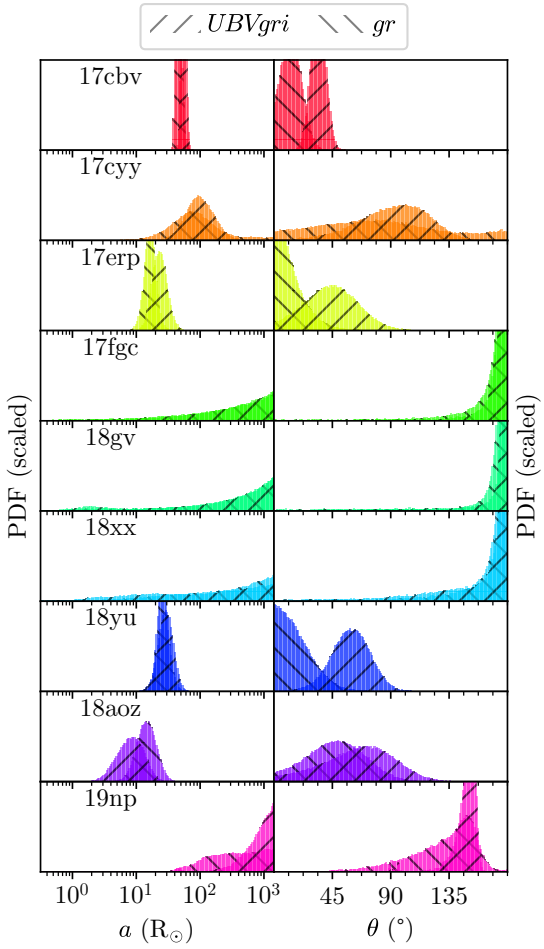

Figure 4.3: The per-object posteriors of the sample presented in Burke et al. (2022 b), which change depending on whether we use the object's $UBVgri$ dataset (as done in that paper) or just its gr data (as we do for the sample presented here). The three objects identified in that paper as having early excesses (SNe 2017cbv, 2017erp, and 2018yu) have best-fit viewing angles which shift towards $\theta = 0$ when the data are limited to gr.

if all SNe Ia arose from single-degenerate systems, there was not enough evidence to disprove that null hypothesis.

Figure 4.2 shows the joint viewing angle posterior both as it was presented in that paper (the pink line), and when the data are limited to just gr (the purple line). This behavior is shown per-object in Figure 4.3, for both the θ and a posteriors. Looking at

the figures, it's clear that objects which have no detectable excess have still converged to having their maximum likelihood at $\theta = 180°$, as they did in the $UBVgri$ models (see SNe 2017fgc, 2018gv, and 2018xx in Figure 4.3). However, the three objects with detectable excesses (SNe 2017cbv, 2017erp, and 2018yu) now have a maximum likelihood closer to $\theta = 0°$ in the gr fits.

This has three implications when the data are limited to gr. One is that the best-fit values of the two relevant physical parameters (i.e. θ and a) should not fully be believed: for example, even though the viewing angles seem to have converged nicely for the gr models, there is a systematic offset from the best-fit $UBVgri$ values for the three objects with early excesses (SNe 2017cbv, 2017erp, and 2018yu). Their best-fit companion separations are also systematically lower, though at lower significance. However, even though the gr models shouldn't be used to measure physical parameters, they can still be used to detect early excesses since early excesses are still present in the data, regardless of filter (see Figure 3 of Burke et al. 2022b). Lastly, it also means that the K-S test done in Burke et al. (2022b) to compare the joint viewing angle posterior to the null hypothesis is no longer applicable, since the per-object posteriors have changed significantly.

ZTF	a ($R_\odot$)	t_{max} (MJD)	s	r_r	θ (°)	σ	ΔBIC	IAU	z	Subtype
abcflnz	$9.4^{+1.5}_{-1.4}$	$58304.78^{+0.08}_{-0.08}$	$0.962^{+0.008}_{-0.007}$	$0.969^{+0.004}_{-0.004}$	6^{+9}_{-5}	$2.03^{+0.08}_{-0.07}$	90.1	cuw	0.0273	normal
aaqcozd	170^{+67}_{-25}	$58253.02^{+0.11}_{-0.11}$	$0.825^{+0.020}_{-0.015}$	$0.863^{+0.019}_{-0.015}$	37^{+40}_{-25}	$0.92^{+0.09}_{-0.08}$	62.7	bjc	0.0732	normal
aaxsioa	$15.8^{+2.7}_{-2.3}$	$58285.78^{+0.05}_{-0.05}$	$0.888^{+0.007}_{-0.007}$	$1.006^{+0.004}_{-0.005}$	10^{+13}_{-7}	$1.97^{+0.13}_{-0.12}$	58.9	cfa	0.0315	normal*
aazblzy	910^{+350}_{-360}	$58291.13^{+0.09}_{-0.09}$	$0.837^{+0.008}_{-0.009}$	$0.943^{+0.007}_{-0.007}$	151^{+4}_{-8}	$1.33^{+0.07}_{-0.07}$	38.3	cri	0.0653	normal
abfhryc	$15.9^{+6.9}_{-4.2}$	$58322.39^{+0.09}_{-0.08}$	$0.980^{+0.010}_{-0.009}$	$1.009^{+0.005}_{-0.005}$	25^{+27}_{-18}	$1.93^{+0.13}_{-0.12}$	21.3	dhw	0.0323	normal
abdfwur	240^{+130}_{-62}	$58310.78^{+0.19}_{-0.19}$	$1.034^{+0.016}_{-0.008}$	$0.906^{+0.015}_{-0.015}$	95^{+25}_{-23}	$1.55^{+0.09}_{-0.08}$	19.1	eps	0.07	normal
aaqcugm	850^{+400}_{-450}	$58254.21^{+0.11}_{-0.11}$	$0.879^{+0.013}_{-0.014}$	$0.962^{+0.010}_{-0.011}$	151^{+5}_{-15}	$1.63^{+0.15}_{-0.12}$	19.0	bhi	0.0619	normal
aazsabq	$12.1^{+4.8}_{-3.3}$	$58293.40^{+0.10}_{-0.10}$	$0.891^{+0.012}_{-0.011}$	$1.006^{+0.006}_{-0.006}$	21^{+26}_{-15}	$1.38^{+0.09}_{-0.08}$	15.8	crn	0.06	normal
abimsyv	55^{+28}_{-19}	$58333.03^{+0.19}_{-0.18}$	$1.003^{+0.021}_{-0.020}$	$0.915^{+0.012}_{-0.012}$	41^{+31}_{-26}	$1.16^{+0.07}_{-0.06}$	13.6	eni	0.088	normal*
abucvbf	150^{+68}_{-43}	$58384.12^{+0.07}_{-0.07}$	$0.965^{+0.010}_{-0.009}$	$0.945^{+0.006}_{-0.006}$	124^{+13}_{-13}	$1.50^{+0.10}_{-0.09}$	12.1	ggw	0.0549	normal
aavrwhu	$31.5^{+8.7}_{-7.5}$	$58275.29^{+0.13}_{-0.13}$	$1.090^{+0.019}_{-0.017}$	$0.967^{+0.006}_{-0.007}$	15^{+22}_{-11}	$1.42^{+0.13}_{-0.11}$	8.9	bxo	0.062	normal
abxxssh	47^{+28}_{-15}	$58396.54^{+0.22}_{-0.19}$	$1.077^{+0.027}_{-0.022}$	$0.902^{+0.013}_{-0.014}$	27^{+34}_{-19}	$1.49^{+0.12}_{-0.11}$	8.9	gvj	0.0782	normal
abssuxz	34^{+17}_{-11}	$58376.82^{+0.20}_{-0.19}$	$0.860^{+0.024}_{-0.018}$	$0.987^{+0.014}_{-0.014}$	31^{+47}_{-23}	$1.15^{+0.13}_{-0.11}$	6.1	gfe	0.0649	normal
abclfee	800^{+400}_{-350}	$58299.06^{+0.08}_{-0.08}$	$0.685^{+0.010}_{-0.009}$	$0.925^{+0.010}_{-0.010}$	154^{+5}_{-8}	$1.68^{+0.09}_{-0.09}$	5.7	cxk	0.029	02cx-like
abdfazk	94^{+53}_{-23}	$58306.60^{+0.22}_{-0.20}$	$0.906^{+0.032}_{-0.025}$	$0.924^{+0.019}_{-0.017}$	43^{+49}_{-29}	$1.17^{+0.11}_{-0.10}$	4.0	dbe	0.084	normal
aawjywv	38^{+19}_{-12}	$58270.85^{+0.18}_{-0.17}$	$0.855^{+0.024}_{-0.020}$	$0.962^{+0.015}_{-0.016}$	30^{+40}_{-22}	$2.02^{+0.19}_{-0.16}$	3.6	ccj	0.0509	normal*
aaxcntm	46^{+26}_{-14}	$58278.81^{+0.08}_{-0.08}$	$0.878^{+0.015}_{-0.013}$	$0.992^{+0.010}_{-0.009}$	73^{+41}_{-32}	$1.70^{+0.13}_{-0.12}$	0.5	ccl	0.0269	normal

Table 4.1: Values of the best-fit parameters and some object properties for the 17 SNe we identify as having early excesses. The "ZTF18" column is the ZTF name (with the "ZTF18-" excluded for space). The next six columns are the best-fit parameters from the models described in Section 4.3.2, followed by the ΔBIC value used to distinguish early-excess SNe as discussed in Section 4.4.1. Lastly we give the IAU name (again excluding the "SN 2018-" for space), the redshift, and the classification as listed in Yao et al. (2019).

4.4 Results

4.4.1 Early Excess Rate

In Burke et al. (2022b), SNe were classified as having an early excess if they met three criteria: (1) if the object had data within five rest-frame days of inferred first light (the typical epochs for an early excess in Kasen 2010), (2) if the best-fit viewing angle was less than 90°, and (3) if the residuals with respect to the stretch template showed a systematic which was representative of an early-but-fading shock component (i.e. if they showed an initial discrepancy of $>5\sigma$ which decreased over time).

In light of the fitting differences caused by the limited filters (see Section 4.3.2), we have changed the criteria to the following: we keep criterion (1) unchanged; we loosen the requirement of criterion (3) due to the lower S/N of the dataset, although such a pattern is still obvious for some objects; and we change criterion (2) completely. Instead of using a hard threshold based on the posterior distribution of a single parameter, we instead compare with a model which only has a stretched template component, excluding the companion shocking component of the model described in Section 4.3.2 (i.e. it does not have the a or θ parameters). We compare the two best-fit models (with and without a companion shocking component) by calculating their respective Bayesian information criteria (BIC; Schwarz 1978), which allows us to select objects where the extra companion shocking parameters quantitatively improve the fit. For each object we calculate a $\Delta\text{BIC} \equiv \text{BIC}_{\text{stretch}} - \text{BIC}_{\text{companion shocking}}$, and identify objects with $\Delta\text{BIC} > 0$ as early-excess SNe Ia.

Applying these criteria to the gr data of the sample in Burke et al. (2022b) accurately recovers the early-excess classifications of that paper, with the exception of SN 2018aoz: Burke et al. (2022b) did not classify that object as early-excess (with some caveats, including the fact that other studies showed it to have extreme color evolution within

the first 24 hours of explosion; Ni et al. 2022a,b), but with a ΔBIC value of 10.6 (the lowest positive value for the sample), this methodology would classify it as such. With only one object having a different classification between the two substantially different approaches (applying a θ cut on posteriors from $UBVgri$ data vs. calculating a ΔBIC from gr data), we believe this validates our use of ΔBIC for early-excess SN selection.

Using the criteria detailed above, we identify 17 objects with early excesses in our sample. Table 4.1 lists the best-fit parameters and some object properties for these 17 SNe. Since the sample contains 127 SNe in total, these 17 objects naïvely represents 13.4% of the total sample, although as we will discuss more shortly, the intrinsic rate of early excesses is slightly higher due to the low S/N of early data potentially obscuring some excesses.

Table 4.1 also includes the ΔBIC values for each object, which range from 90.1 for ZTF18abcflnz (causing a confident classification of it as an early-excess object) to 0.5 for the more marginal ZTF18aaxcntm. The threshold of $\Delta\text{BIC} > 0$ is well-motivated but in the end somewhat arbitrary, since we are mapping a continuous probability (i.e. the likelihood that an object has an early excess) to a binary classification ("this SN is/is not an early-excess SN"). Stricter cuts in ΔBIC, e.g. using $\Delta\text{BIC} > 10$ as the dividing line for early-excess SNe, would of course change the numerical rate of early excesses we ultimately calculate. With this caveat in mind, we will use $\Delta\text{BIC} > 0$ as the threshold for the rest of this paper.

Figure 4.4 shows the best-fit model and residuals for a single object which we identify as having an early excess (ZTF18aaxsioa, the same object shown in Figure 4.1). The distinctive pattern in the residuals with respect to the stretch template (diamonds), where their discrepancy diminishes over time, is characteristic of an early-but-fading shock component (see Figure 3 of Burke et al. 2022b).

The sample modeled in Burke et al. (2022b) consisted of nine objects, three of which

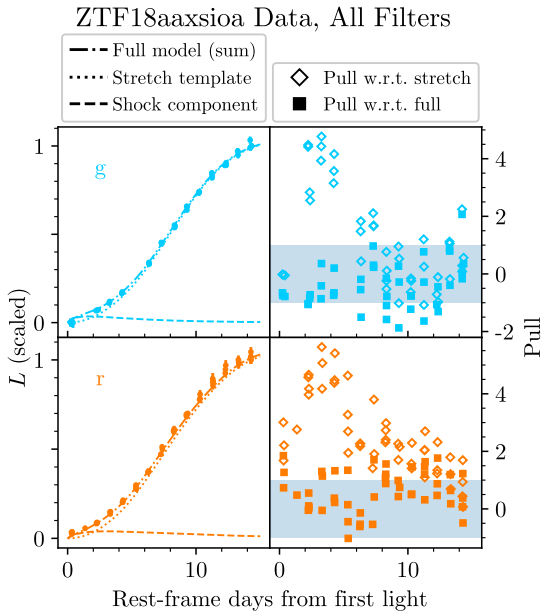

Figure 4.4: The best-fit model and residuals for ZTF18aaxsioa, an object with an early excess. The left panels show the per-filter data and the two components of the model: the stretched template (dotted line) and the shock component (dashed), which are added together to the full model. The right panels show the residuals with respect to both the full model (filled squares) and the stretched template (empty diamonds), where the signature of the early excess is obvious (initial discrepancy which vanishes over time). "Pull" is defined as the number of standard deviations a data point is away from the relevant model, divided by the best-fit σ value – the majority of square points should cluster within one standard deviation of zero (the grey shaded box), which they do.

had early excesses: that paper therefore calculated an early excess rate from simple Poissonian statistics of $33 \pm 19\%$. However, the objects in that paper were extremely low-redshift ($z < 0.01$), and all objects were detected well above the telescopes' limiting magnitudes within five days of inferred first light. ("First light" in this context being the time when the SN flux is first detectable, which is not necessarily the same as when the explosion occurred due to "dark phases" in SNe Ia when the radiation has not yet diffused out of the ejecta – see Piro & Nakar 2013 where this is discussed in more detail.) Burke et al. (2022b) assumed that any potential early excesses would be revealed by

S/N cut (σ)	n_{objects}	n_{EEx}	Rate
N/A	127	17	$13.4 \pm 3.2\%$
3	103	17	$16.5 \pm 4.0\%$
5	92	17	$18.5 \pm 4.5\%$
8	68	17	$25.0 \pm 6.1\%$
10	49	14	$28.6 \pm 7.6\%$
15	26	10	$38 \pm 12\%$
20	18	8	$44 \pm 16\%$
30	9	2	$22 \pm 16\%$
50	4	2	$50 \pm 35\%$

Table 4.2: The effect on the early excess (EEx) rate of imposing different S/N cuts on the early data, e.g. requiring that at least one epoch within five rest-frame days of inferred first light has a $>10\sigma$ detection. We quote an overall early excess rate of $18.5 \pm 4.5\%$, the value from the 5σ cut.

the data. The sample here is significantly different: it is much higher redshift (median redshift of 0.076), resulting in lower average signal-to-noise (S/N) in the crucial earliest epochs.

This lower S/N could serve to obscure weak early excesses hiding in the data. For instance, in this sample only 81% of the objects (103 out of 127) are detected at all within 5 rest-frame days of inferred first light. Table 4.2 shows the results of imposing different S/N cuts on the early data of the sample, e.g. only considering objects which have a $>10\sigma$ detection with 5 days of first light. Each S/N cut leaves some total number of objects, and also some subset of the early-excess objects, from which an early excess rate can be calculated. The 30σ cut leaves a sample extremely similar to the one in Burke et al. (2022b): that paper had an early excess rate of 3 out of 9 objects ($33 \pm 19\%$), and limiting the sample here to SNe with a 30σ detection in the epochs where an early excess could be detected yields a rate of 2 out of 9 objects ($22 \pm 16\%$). We thus believe that the sample here is identical to the sample of Burke et al. (2022b), except at higher redshift and observed in fewer bands. As in that paper, the distribution of early excess strengths here is consistent with SNe Ia predominantly arising in single-degenerate systems.

Which rate should we quote as the single rate of early excesses in SNe Ia? As is obvious in Table 4.2, using a less restrictive S/N cut results in a smaller formal uncertainty due to the larger sample size, but it also means that lower intensity early excesses could be hidden in the data, undetected. We use the value calculated from the S/N>5 cut, since that S/N is sufficient to detect strong early excesses. It is possible that the higher rates derived from stricter S/N cuts are consistent with the prediction in Kasen (2010), i.e. that higher S/N data could detect weaker excesses, leading to a higher overall rate of excesses, but the uncertainties on the rates make it difficult to state this with confidence. We thus quote the rate of early excesses in SNe Ia as $18.5 \pm 4.5\%$.

The rate of early excesses in SNe Ia which we measure here is consistent with the rate calculated in Deckers et al. (2022) of $18 \pm 11\%$ (calculated from the same dataset), and is also consistent with the limit of $\lesssim$30% based on the non-detections in Miller et al. (2020 b), again calculated from the same dataset. It is also consistent with the rate calculated in Burke et al. (2022b) of $33 \pm 19\%$. Magee et al. (2020) find 5 excesses in a sample of 23 SNe, corresponding to a rate of $22 \pm 10\%$, which we are also consistent with. The theoretically expected rate quoted in Kasen (2010) is $\sim$10% for strong excesses: our value is formally discrepant with this, although since this rate is an approximation based on assumptions of S/N (detectability) and companion separation (intrinsic excess strength), the mild discrepancy is not too concerning. The rates of early excesses from all these studies, with their widely varying methodologies, are consistent with the null hypothesis that SNe Ia predominantly arise from single-degenerate systems.

Additionally, as seen in Table 4.1, all but one of the 17 early-excess SNe are classified as normal SNe Ia, with the exception being an underluminous 02cx-like. The sample contains 13 overluminous SNe Ia (i.e. 99aa-like or 91T-like), and Jiang et al. (2018) suggested that such overluminous SNe Ia uniformly have early excesses based on six out of six such objects in their sample exhibiting early excesses. We do not see this effect

here: most of the overluminous objects in this sample do have relatively low early S/N due to their higher redshift, but two of them (ZTF18abgmcmv and ZTF18abauprj) have early S/N > 30 and still have no detectable early excess. The early-excess objects are not even clustered to the luminous end of normal SNe Ia, with only four of the 17 having $\Delta m_{15} < 1.0$ (as measured by `SNooPy`).

4.4.2 Methodology-dependent Early Excess Detections

As noted in Section 4.2, this sample of objects was introduced in a series of three papers, and an additional paper (Deckers et al. 2022) examined the same dataset through the lens of Ni models. Each of these four previous studies, and now the one presented here, have independently looked for objects with early excesses. Table 4.3 therefore lists the early-excess objects identified by each paper, each of which approached the identification with a distinct methodology: Yao et al. (2019) identified two early-excess objects based on photometric comparison to other objects with extremely early data (more than 17 days before peak); Miller et al. (2020b) identified zero early-excess objects, since all rising lightcurves were consistent with their general power-law fits; Bulla et al. (2020) identified six objects which had red bumps at early times in their $g - r$ color evolutions; and Deckers et al. (2022) identified six objects with early excesses, based on quantitative measures of whether they could be fit by any Ni-mixing models in the model grids from Magee et al. (2018) and Magee et al. (2020). As the table makes apparent, each paper (i.e. each methodology) identified mostly mutually exclusive sets of SNe. As stated above, we identify 17 objects with early excesses based on their fits to companion shocking models, adding another mostly-mutually-exclusive set of early-excess SNe Ia from this sample.

Even though they might seem contradictory, two things are both true: this work and each of the papers mentioned above have (different) quantitative measures to detect early

[1]	[2]	[3]	[4]	[5]
		aapqwyv		
				aaqcozd
				aaqcugm
			aaqqoqs	
aavrwhu				aavrwhu
				aawjywv
				aaxcntm
				aaxsioa
			aayjvve	
				aazblzy
				aazsabq
		abcflnz		abcflnz
				abclfee
		abckujq		
		abcrxoj		
			abdfazk	abdfazk
			abdfwur	abdfwur
				abfhryc
		abgxvra		
				abimsyv
			abpamut	
				abssuxz
				abucvbf
abxxssh		abxxssh	abxxssh	abxxssh

Table 4.3: Which SNe in this sample have early excesses, as identified by different papers. The "ZTF18" has been omitted from each object name to save space. As is apparent in the table and as discussed in the text, the statement "this SN does/does not have an early excess" is methodology-dependent. References: 1: Yao et al. (2019), 2: Miller et al. (2020b), 3: Bulla et al. (2020), 4: Deckers et al. (2022), 5: this work.

excesses, and also they all mostly disagree on which objects have early excesses. These statements do not invalidate each other – we merely want to stress that even though the final cuts for which objects have early excesses can be quantitative (i.e. objective), the assumptions undergirding the methodologies introduce (subjective) biases which end up with different results.

Figures 4.5, 4.6, and 4.7 show the fits and residuals for three different sets of SNe

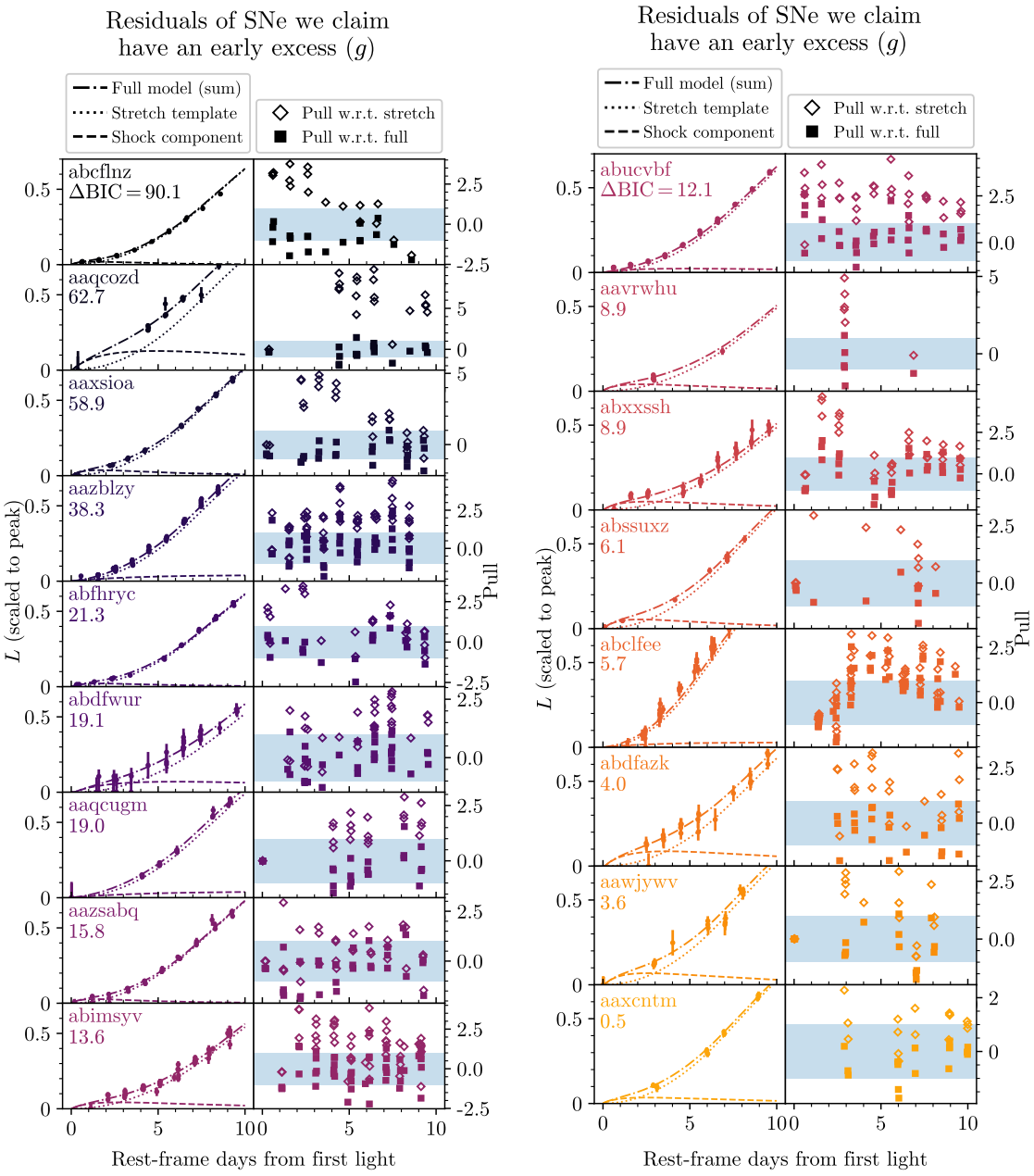

Figure 4.5: Fits and residuals for objects we identify as having an early excess. Objects are ordered by ΔBIC (see Table 4.1), which is included as a label on the left for each object.

drawn from the sample. Figure 4.5 shows the 17 objects which we identify as having an early excess, in the order of their ΔBIC as listed in Table 4.1. Two of the first

three objects (ZTF18aaxsioa and ZTF18abcflnz) have residuals which show a clear and temporally resolved shock component, manifesting as an initial discrepancy with respect to the stretch template which then fades over time, similar to the residuals of the early-excess SNe identified in Burke et al. (2022b). ZTF18aaxsioa was already plotted in Figure 4.4, since its residuals have such a clear systematic. The rest of the objects show a variety of behavior: some objects (e.g. ZTF18abfhryc, ZTF18aavrwhu, ZTF18abxxssh) have discrepancies with the stretched template which are only apparent in the first few epochs, while other objects require a shock component which is much stronger (ZTF18abdfazk) or longer-lasting (ZTF18abdfwur) than the weak but clearly resolved shocks seen for ZTF18abcflnz and ZTF18aaxsioa. The rest of the objects have less-obvious patterns in their residuals, but nevertheless they are poorly fit by the stretch template alone and the models unambiguously prefer some shock component.

The next set of objects (Figure 4.6) are the seven objects which other papers identify as having an early excess, but we do not. Some objects (ZTF18aapqwyv, ZTF18aaqqoqs) have converged to a similar region of parameter space as SN 2019np did in Burke et al. (2022b), with a large best-fit companion separation seen at a high viewing angle needed to explain the discrepancy with the stretch template. This matches the analysis of SN 2019np, where another study did identify it as having an early excess (Sai et al. 2022), even though Burke et al. (2022b) did not. Others (ZTF18aayjvve, ZTF18abgxvra) have no signs of disagreement with our stretch template – in the case of ZTF18abgxvra only Bulla et al. (2020) identified it as having an early excess, and since that paper relied on color evolution to identify excesses, the object's early peculiarities may not be obvious when looking filter-by-filter.

The last set of objects (Figure 4.7) was selected because the objects have exemplary early data, and also showed no signs of any early excesses (i.e. the two sets of residuals are on top of each other). We include this set primarily to show that some objects have

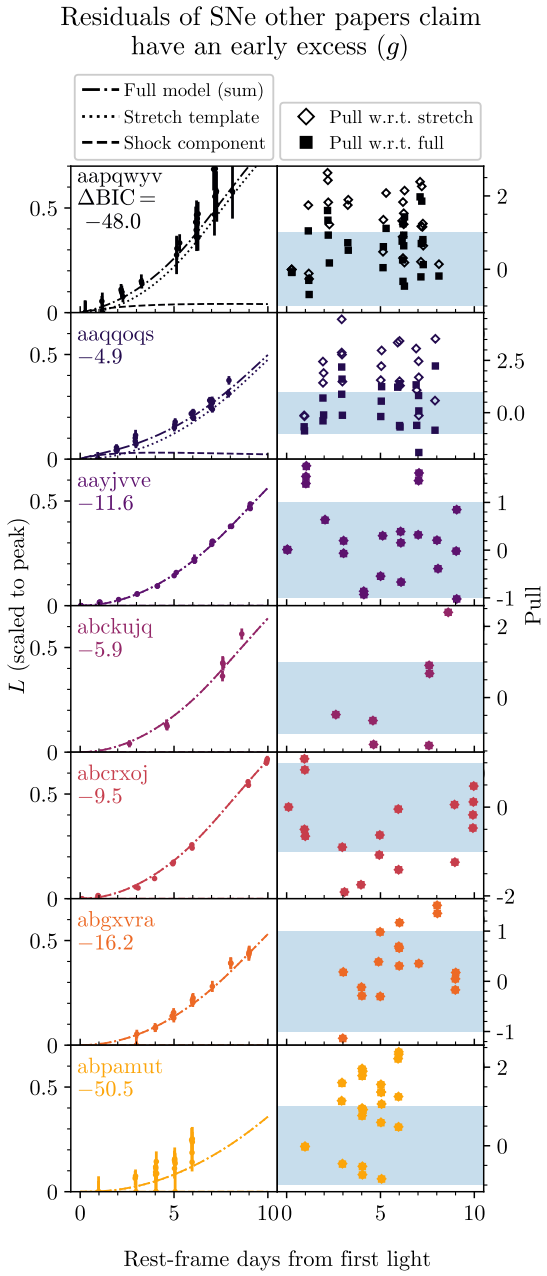

Figure 4.6: Identical to Figure 4.5, but for the objects which other papers identify as having an early excess (see Table 4.3). Panels are labelled with the object name, sans ZTF18-. See the text for discussion of different fits.

early lightcurves which are fit excellently by the stretch template alone, validating its use.

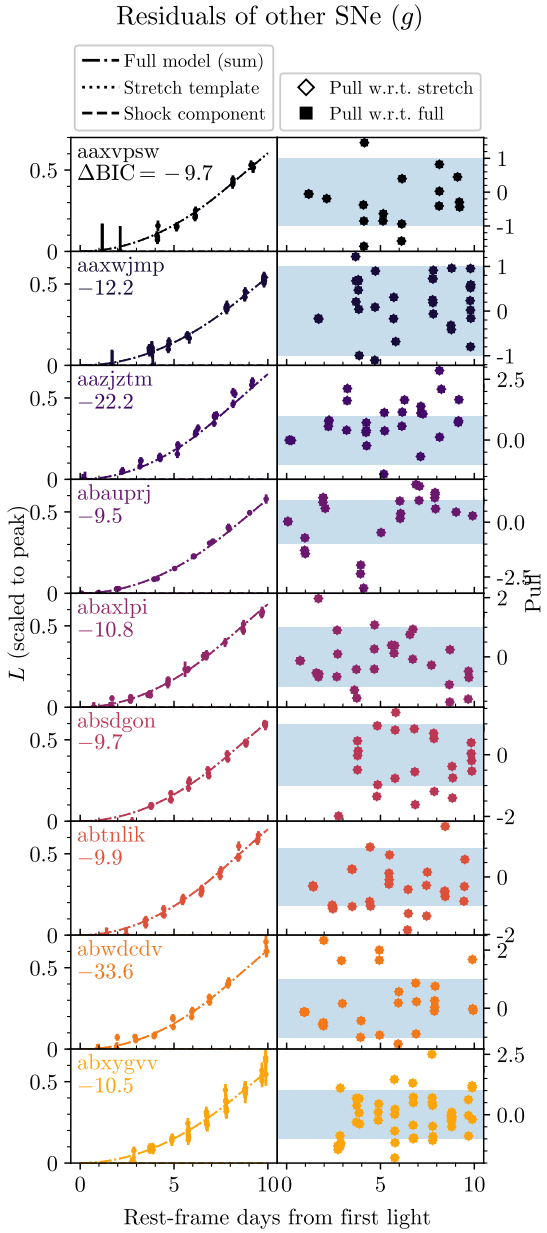

Figure 4.7: Identical to Figures 4.5 and 4.6, but for objects which have especially good early data, and show no signatures of an early excess. We include this figure to show that the stretch template by itself can be an excellent fit to some objects, validating its use.

Lastly, we show the color evolution of the sample in Figure 4.8, highlighting early-excess objects. In Burke et al. (2022b), the SN with the clearest early excess (SN 2017cbv)

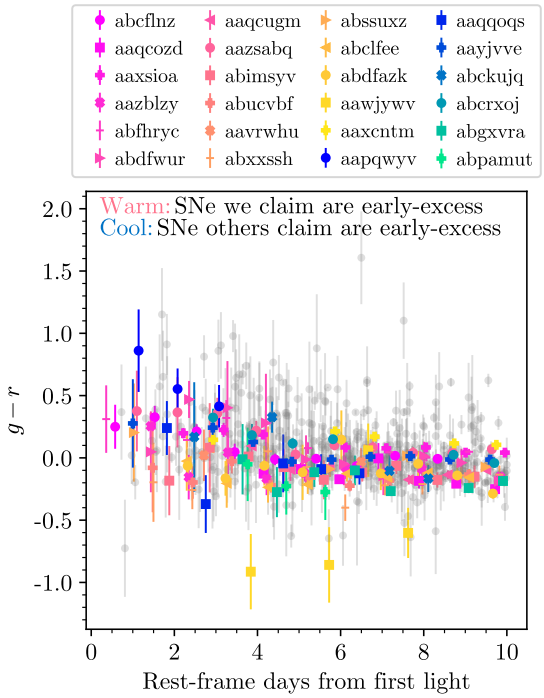

Figure 4.8: Color evolution of the sample. The 17 SNe we identify as having an early excess are shown in warm colors, and the 7 SNe other papers identify as having an early excess are shown in cool colors (see Table 4.3 for early-excess classifications). The rest of the sample is shown in grey. Colors have been extinction- and K-corrected. Compare Figures 1 and 4 of Bulla et al. (2020).

also had the bluest $g-r$ colors at early times. That is not quite true here, where the two SNe with the clearest early excesses in our fits (ZTF18aaxsioa and ZTF18abcflnz) are not the bluest at early times; however, ZTF18abxxssh is among the bluest SNe within three days of first light, and it is the object that most papers identify as having an early excess (see Table 4.3). Generally, SNe Ia seem to show lower dispersion in their early $g-r$ evolution compared to other colors (such as $B-V$ or UV filter combinations, see Figures 9 and 10 from Burke et al. 2022b), but we refer to Bulla et al. (2020) for a much more thorough investigation of this sample's color properties.

4.5 Conclusion

We have reexamined the 2018 ZTF sample of early SNe Ia (Yao et al. 2019; Miller et al. 2020b; Bulla et al. 2020), using models from Kasen (2010) to search for signatures of nondegenerate companion interaction in the form of early excesses in the lightcurves. We found 17 such objects with signatures of companion interaction: this naïvely represents 13.4% of the sample, but when compensating for the S/N of the early data we calculate an overall early excess rate of $18.5 \pm 4.5\%$. This rate is consistent with several others calculated throughout the literature, using different methodologies and/or samples to detect early excesses. This rate is also consistent with the expectation that SNe Ia predominantly arise from progenitor systems with a Roche-lobe-overflowing nondegenerate companion. However, early excesses only occur in this sample in normal SNe Ia (and one underluminous SN) and not in any of the 13 overluminous objects, which is inconsistent with the claim in Jiang et al. (2018) that overluminous SNe Ia have ubiquitous early excesses.

In addition to this result, we also showed that the detection of early excesses can be methodology-dependent. For instance, despite the fact that this same sample had been analyzed by four previous papers, each of which looked for objects with early excesses, we identify 12 SNe Ia as having early excesses which none of the previous papers identified as such. This meta-analysis shows that different methodologies make a variety of assumptions about the early lightcurves of SNe Ia, which can lead to different results.

Companion interaction models have been shown for several years to be excellent (if imperfect) fits to SNe Ia with early excesses (see e.g. Hosseinzadeh et al. 2017; Dimitriadis et al. 2019a; Burke et al. 2021; Hosseinzadeh et al. 2022; Burke et al. 2022b). We strongly encourage the observation of large samples of SNe Ia with high-cadence multiwavelength early data (such as the ones in this paper and in Burke et al. 2022b) so that models'

predictions might be tested and the the uncertainty around the progenitor systems of SNe Ia might be gradually reduced. We also encourage continued theoretical work on companion interaction models, since the state of the art is now more than a decade old (Kasen 2010).

Bibliography

Abbott, B. P., Abbott, R., Abbott, T. D., et al. 2017, ApJL, 848, L12

Arnett, W. D. 1982, ApJ, 253, 785

Ashall, C., Mazzali, P., Sasdelli, M., & Prentice, S. J. 2016, MNRAS, 460, 3529

Ashall, C., Lu, J., Shappee, B. J., et al. 2022, ApJL, 932, L2

Barbary, K. 2016, Extinction V0.3.0, Zenodo, Zenodo, doi:10.5281/zenodo.804967

Barbary, K., rbiswas4, Goldstein, D., et al. 2016,

Beasor, E. R., Davies, B., Smith, N., et al. 2020, MNRAS, 492, 5994

Bellm, E. C., Kulkarni, S. R., Graham, M. J., et al. 2019, PASP, 131, 018002

Benetti, S., Meikle, P., Stehle, M., et al. 2004, MNRAS, 348, 261

Bianco, F. B., Howell, D. A., Sullivan, M., et al. 2011, ApJ, 741, 20

Blondin, S., & Tonry, J. L. 2007, ApJ, 666, 1024

Blondin, S., Matheson, T., Kirshner, R. P., et al. 2012, AJ, 143, 126

Bostroem, K. A., Valenti, S., Sand, D. J., et al. 2020, ApJ, 895, 31

Bottinelli, L., Gouguenheim, L., Paturel, G., & de Vaucouleurs, G. 1985, A&AS, 59, 43

Botyánszki, J., Kasen, D., & Plewa, T. 2018, ApJL, 852, L6

Branch, D., Dang, L. C., Hall, N., et al. 2006, PASP, 118, 560

Breeveld, A. A., Curran, P. A., Hoversten, E. A., et al. 2010, MNRAS, 406, 1687

Brown, P. J., Breeveld, A. A., Holland, S., Kuin, P., & Pritchard, T. 2014, Ap&SS, 354, 89

Brown, P. J., Dawson, K. S., Harris, D. W., et al. 2012a, ApJ, 749, 18

Brown, P. J., Landez, N. J., Milne, P. A., & Stritzinger, M. D. 2017, ApJ, 836, 232

Brown, P. J., Perry, J. M., Beeny, B. A., Milne, P. A., & Wang, X. 2018, ApJ, 867, 56

Brown, P. J., Roming, P. W. A., Milne, P., et al. 2010, ApJ, 721, 1608

Brown, P. J., Dawson, K. S., de Pasquale, M., et al. 2012b, ApJ, 753, 22

Brown, P. J., Hosseinzadeh, G., Jha, S. W., et al. 2019, ApJ, 877, 152

Brown, T. M., Baliber, N., Bianco, F. B., et al. 2013, PASP, 125, 1031

Bulla, M., Miller, A. A., Yao, Y., et al. 2020, ApJ, 902, 48

Burke, J., Howell, D. A., Sand, D. J., & Hosseinzadeh, G. 2022a, arXiv e-prints, , arXiv:2208.11201

Burke, J., Howell, D. A., Sarbadhicary, S. K., et al. 2021, ApJ, 919, 142

Burke, J., Howell, D. A., Sand, D. J., et al. 2022b, arXiv e-prints, , arXiv:2207.07681

Burns, C. R., Stritzinger, M., Phillips, M. M., et al. 2011, AJ, 141, 19

Cao, Y., Kulkarni, S. R., Gal-Yam, A., et al. 2016, ApJ, 832, 86

Cao, Y., Kulkarni, S. R., Howell, D. A., et al. 2015, Natur, 521, 328

Cartier, R., Sullivan, M., Firth, R. E., et al. 2017, MNRAS, 464, 4476

Chevalier, R. A. 1982, ApJ, 259, 302

—. 1984, ApJL, 285, L63

—. 1998, ApJ, 499, 810

Chevalier, R. A., & Fransson, C. 2006, ApJ, 651, 381

Chomiuk, L., Soderberg, A. M., Moe, M., et al. 2012, ApJ, 750, 164

Chomiuk, L., Soderberg, A. M., Chevalier, R. A., et al. 2016, ApJ, 821, 119

Conley, A., Sullivan, M., Hsiao, E. Y., et al. 2008, ApJ, 681, 482

Deckers, M., Maguire, K., Magee, M. R., et al. 2022, MNRAS,

Dessart, L., Leonard, D. C., & Prieto, J. L. 2020, A&A, 638, A80

Dey, A., Schlegel, D. J., Lang, D., et al. 2019, AJ, 157, 168

Dimitriadis, G., Foley, R. J., Rest, A., et al. 2019a, ApJL, 870, L1

Dimitriadis, G., Rojas-Bravo, C., Kilpatrick, C. D., et al. 2019b, ApJL, 870, L14

Eggleton, P. P. 1983, ApJ, 268, 368

Elias-Rosa, N., Chen, P., Benetti, S., et al. 2021, A&A, 652, A115

Ellis, R. S., Sullivan, M., Nugent, P. E., et al. 2008, ApJ, 674, 51

Fausnaugh, M. M., Vallely, P. J., Kochanek, C. S., et al. 2021, ApJ, 908, 51

Fink, M., Röpke, F. K., Hillebrandt, W., et al. 2010, A&A, 514, A53

Firth, R. E., Sullivan, M., Gal-Yam, A., et al. 2015, MNRAS, 446, 3895

Folatelli, G., Phillips, M. M., Morrell, N., et al. 2012, ApJ, 745, 74

Foley, R. J., Narayan, G., Challis, P. J., et al. 2010, ApJ, 708, 1748

Foley, R. J., Pan, Y.-C., Brown, P., et al. 2016, MNRAS, 461, 1308

Foreman-Mackey, D., Hogg, D. W., Lang, D., & Goodman, J. 2013, PASP, 125, 306

Förster, F., González-Gaitán, S., Folatelli, G., & Morrell, N. 2013, ApJ, 772, 19

Galbany, L., Ashall, C., Höflich, P., et al. 2019, A&A, 630, A76

Ganeshalingam, M., Li, W., & Filippenko, A. V. 2011, MNRAS, 416, 2607

Ganeshalingam, M., Li, W., Filippenko, A. V., et al. 2010, ApJS, 190, 418

—. 2012, ApJ, 751, 142

Gehrels, N., Chincarini, G., Giommi, P., et al. 2004, ApJ, 611, 1005

Goldhaber, G., Groom, D. E., Kim, A., et al. 2001, ApJ, 558, 359

González-Gaitán, S., Perrett, K., Sullivan, M., et al. 2011, ApJ, 727, 107

González-Gaitán, S., Conley, A., Bianco, F. B., et al. 2012, ApJ, 745, 44

Guy, J., Astier, P., Baumont, S., et al. 2007, A&A, 466, 11

Hayden, B. T., Garnavich, P. M., Kasen, D., et al. 2010, ApJ, 722, 1691

Henden, A. A., Welch, D. L., Terrell, D., & Levine, S. E. 2009, AAS Meeting Abstracts, 214, 407.02

Heringer, E., van Kerkwijk, M. H., Sim, S. A., & Kerzendorf, W. E. 2017, ApJ, 846, 15

Hiramatsu, D., Howell, D. A., Moriya, T. J., et al. 2021, ApJ, 913, 55

Hodgkin, S. T., Breedt, E., Delgado, A., et al. 2020, Transient Name Server Astronomical Transient Report,

Höflich, P., Gerardy, C. L., Fesen, R. A., & Sakai, S. 2002, ApJ, 568, 791

Horesh, A., Kulkarni, S. R., Fox, D. B., et al. 2012, ApJ, 746, 21

Hosseinzadeh, G. 2019, Light Curve Fitting, vv0.0.0, Zenodo, doi:10.5281/zenodo.2639464

Hosseinzadeh, G., Sand, D. J., Valenti, S., et al. 2017, ApJL, 845, L11

Hosseinzadeh, G., Sand, D. J., Lundqvist, P., et al. 2022, ApJL, 933, L45

Howell, D. A. 2011, NatCo, 2, 350

Howell, D. A., & Global Supernova Project. 2017, in American Astronomical Society Meeting Abstracts, Vol. 230, American Astronomical Society Meeting Abstracts #230, 318.03

Hoyle, F., & Fowler, W. A. 1960, ApJ, 132, 565

Hsiao, E. Y., Marion, G. H., Phillips, M. M., et al. 2013, ApJ, 766, 72

Hsiao, E. Y., Phillips, M. M., Marion, G. H., et al. 2019, PASP, 131, 014002

Iben, I., J., & Tutukov, A. V. 1984, ApJS, 54, 335

Itagaki, K. 2017, Transient Name Server Discovery Report, 2017-647, 1

—. 2018, Transient Name Server Discovery Report, 2018-57, 1

—. 2019a, Transient Name Server Discovery Report, 2019-53, 1

—. 2019b, Transient Name Server Discovery Report, 2019-2720, 1

Jha, S., Riess, A. G., & Kirshner, R. P. 2007, ApJ, 659, 122

Jha, S. W., Maguire, K., & Sullivan, M. 2019, Nature Astronomy, 3, 706

Jiang, J.-a., Doi, M., Maeda, K., & Shigeyama, T. 2018, ApJ, 865, 149

Jiang, J.-A., Doi, M., Maeda, K., et al. 2017, Nature, 550, 80

Jiang, J.-a., Maeda, K., Kawabata, M., et al. 2021, ApJL, 923, L8

Kasen, D. 2006, ApJ, 649, 939

—. 2010, ApJ, 708, 1025

Kasen, D., Röpke, F. K., & Woosley, S. E. 2009, Nature, 460, 869

Kawabata, M. 2020, Transient Name Server Classification Report, 2020-24, 1

Kerzendorf, W. E., & Sim, S. A. 2014, MNRAS, 440, 387

Khokhlov, A. M. 1991, A&A, 245, 114

Kochanek, C. S., Shappee, B. J., Stanek, K. Z., et al. 2017, PASP, 129, 104502

Kollmeier, J. A., Chen, P., Dong, S., et al. 2019, MNRAS, 486, 3041

Landolt, A. U. 1992, AJ, 104, 340

Levanon, N., & Soker, N. 2019, ApJL, 872, L7

Li, W., Wang, X., Vinkó, J., et al. 2019, ApJ, 870, 12

Liu, Z.-W., Moriya, T. J., & Stancliffe, R. J. 2015, MNRAS, 454, 1192

Magee, M. R., & Maguire, K. 2020, A&A, 642, A189

Magee, M. R., Maguire, K., Kotak, R., et al. 2020, A&A, 634, A37

Magee, M. R., Sim, S. A., Kotak, R., & Kerzendorf, W. E. 2018, A&A, 614, A115

Maguire, K., Taubenberger, S., Sullivan, M., & Mazzali, P. A. 2016, MNRAS, 457, 3254

Maguire, K., Sullivan, M., Thomas, R. C., et al. 2011, MNRAS, 418, 747

Maoz, D., Mannucci, F., & Nelemans, G. 2014, ARA&A, 52, 107

Marietta, E., Burrows, A., & Fryxell, B. 2000, ApJS, 128, 615

Marion, G. H., Brown, P. J., Vinkó, J., et al. 2016, ApJ, 820, 92

Mattila, S., Lundqvist, P., Sollerman, J., et al. 2005, A&A, 443, 649

Miller, A. A., Cao, Y., Piro, A. L., et al. 2018, ApJ, 852, 100

Miller, A. A., Magee, M. R., Polin, A., et al. 2020a, ApJ, 898, 56

Miller, A. A., Yao, Y., Bulla, M., et al. 2020b, ApJ, 902, 47

Milne, P. A., Brown, P. J., Roming, P. W. A., Bufano, F., & Gehrels, N. 2013, ApJ, 779, 23

Ni, Y. Q., Moon, D.-S., Drout, M. R., et al. 2022a, Nature Astronomy,

—. 2022b, arXiv e-prints, , arXiv:2206.12437

Nugent, P., Phillips, M., Baron, E., Branch, D., & Hauschildt, P. 1995, ApJL, 455, L147

Nugent, P. E., Sullivan, M., Cenko, S. B., et al. 2011, Nature, 480, 344

Olling, R. P., Mushotzky, R., Shaya, E. J., et al. 2015, Natur, 521, 332

Pakmor, R., Kromer, M., Taubenberger, S., et al. 2012, ApJL, 747, L10

Pakmor, R., Kromer, M., Taubenberger, S., & Springel, V. 2013, ApJL, 770, L8

Panagia, N., Van Dyk, S. D., Weiler, K. W., et al. 2006, ApJ, 646, 369

Pankey, Titus, J. 1962, PhD thesis, Howard University, Washington DC

Papadogiannakis, S., Goobar, A., Amanullah, R., et al. 2019, MNRAS, 483, 5045

Parrent, J., Friesen, B., & Parthasarathy, M. 2014, Ap&SS, 351, 1

Parrent, J. T., Thomas, R. C., Fesen, R. A., et al. 2011, ApJ, 732, 30

Patat, F., Benetti, S., Cappellaro, E., et al. 1996, MNRAS, 278, 111

Pérez-Torres, M. A., Lundqvist, P., Beswick, R. J., et al. 2014, ApJ, 792, 38

Perlmutter, S., Gabi, S., Goldhaber, G., et al. 1997, ApJ, 483, 565

Perlmutter, S., Aldering, G., Goldhaber, G., et al. 1999, ApJ, 517, 565

Pessi, P. J., Hsiao, E. Y., Folatelli, G., et al. 2022, MNRAS, 510, 4929

Phillips, M. M. 1993, ApJL, 413, L105

Phillips, M. M., Lira, P., Suntzeff, N. B., et al. 1999, AJ, 118, 1766

Phillips, M. M., Simon, J. D., Morrell, N., et al. 2013, ApJ, 779, 38

Piro, A. L., & Morozova, V. S. 2016, ApJ, 826, 96

Piro, A. L., & Nakar, E. 2013, ApJ, 769, 67

Polin, A., Nugent, P., & Kasen, D. 2019, ApJ, 873, 84

—. 2021, ApJ, 906, 65

Poznanski, D., Prochaska, J. X., & Bloom, J. S. 2012, MNRAS, 426, 1465

Prieto, J. L., Rest, A., & Suntzeff, N. B. 2006, ApJ, 647, 501

Prieto, J. L., Chen, P., Dong, S., et al. 2020, ApJ, 889, 100

Rau, U., & Cornwell, T. J. 2011, A&A, 532, A71

Rayner, J. T., Toomey, D. W., Onaka, P. M., et al. 2003, PASP, 115, 362

Richmond, M. W., Treffers, R. R., Filippenko, A. V., et al. 1995, AJ, 109, 2121

Riess, A. G., Filippenko, A. V., Challis, P., et al. 1998, The Astronomical Journal, 116, 1009–1038

Roming, P. W. A., Kennedy, T. E., Mason, K. O., et al. 2005, SSRv, 120, 95

Rothberg, B., & Joseph, R. D. 2006, AJ, 131, 185

Ryder, S. D., Sadler, E. M., Subrahmanyan, R., et al. 2004, MNRAS, 349, 1093

Sai, H., Wang, X., Elias-Rosa, N., et al. 2022, MNRAS,

Salas, P., Bauer, F. E., Stockdale, C., & Prieto, J. L. 2013, MNRAS, 428, 1207

Sand, D. J., Graham, M. L., Botyánszki, J., et al. 2018, ApJ, 863, 24

Sand, D. J., Amaro, R. C., Moe, M., et al. 2019, ApJL, 877, L4

Sand, D. J., Sarbadhicary, S. K., Pellegrino, C., et al. 2021, ApJ, 922, 21

Schlafly, E. F., & Finkbeiner, D. P. 2011, ApJ, 737, 103

Schlegel, D. J., Finkbeiner, D. P., & Davis, M. 1998, ApJ, 500, 525

Schmidt, G. D., Weymann, R. J., & Foltz, C. B. 1989, PASP, 101, 713

Schwarz, G. 1978, Annals of Statistics, 6, 461

SDSS Collaboration, Albareti, F. D., Allende Prieto, C., et al. 2017, ApJS, 233, 25

Shappee, B. J., Prieto, J. L., Grupe, D., et al. 2014, ApJ, 788, 48

Shappee, B. J., Holoien, T. W. S., Drout, M. R., et al. 2019, ApJ, 870, 13

Shen, K. J., Blondin, S., Kasen, D., et al. 2021, ApJL, 909, L18

Shen, K. J., Boubert, D., Gänsicke, B. T., et al. 2018, ApJ, 865, 15

Siebert, M. R., Dimitriadis, G., Polin, A., & Foley, R. J. 2020, ApJL, 900, L27

Silverman, J. M., & Filippenko, A. V. 2012, MNRAS, 425, 1917

Sim, S. A., Fink, M., Kromer, M., et al. 2012, MNRAS, 420, 3003

Smartt, S. J., Valenti, S., Fraser, M., et al. 2015, A&A, 579, A40

Soderberg, A. M., Chevalier, R. A., Kulkarni, S. R., & Frail, D. A. 2006, ApJ, 651, 1005

Stetson, P. B. 2000, PASP, 112, 925

Stritzinger, M. D., Shappee, B. J., Piro, A. L., et al. 2018, ApJL, 864, L35

Tartaglia, L., Sand, D. J., Valenti, S., et al. 2018, ApJ, 853, 62

Taubenberger, S. 2017, in Handbook of Supernovae, ed. A. W. Alsabti & P. Murdin (Springer, Cham)

Taubenberger, S., Kromer, M., Pakmor, R., et al. 2013, ApJL, 775, L43

Terry, J. N., Paturel, G., & Ekholm, T. 2002, A&A, 393, 57

Thomas, R. C., Aldering, G., Antilogus, P., et al. 2011, ApJ, 743, 27

Tonry, J. L., Dressler, A., Blakeslee, J. P., et al. 2001, ApJ, 546, 681

Tonry, J. L., Denneau, L., Heinze, A. N., et al. 2018, PASP, 130, 064505

Tucker, B. E. 2011, Ap&SS, 335, 223

Tucker, M. A., Shappee, B. J., & Wisniewski, J. P. 2019, ApJL, 872, L22

Tucker, M. A., Shappee, B. J., Vallely, P. J., et al. 2020, MNRAS, 493, 1044

Tucker, M. A., Ashall, C., Shappee, B. J., et al. 2021, ApJ, 914, 50

Valenti, S., Sand, D., Pastorello, A., et al. 2014, MNRAS, 438, L101

Valenti, S., Howell, D. A., Stritzinger, M. D., et al. 2016, MNRAS, 459, 3939

Wang, B., & Han, Z. 2012, NewAR, 56, 122

Wang, X., Filippenko, A. V., Ganeshalingam, M., et al. 2009, ApJL, 699, L139

Weiler, K. W., Williams, C. L., Panagia, N., et al. 2007, ApJ, 671, 1959

Whelan, J., & Iben, Icko, J. 1973, ApJ, 186, 1007

White, C. J., Kasliwal, M. M., Nugent, P. E., et al. 2015, ApJ, 799, 52

Wyatt, S. D., Sand, D. J., Hsiao, E. Y., et al. 2021, ApJ, 914, 57

Yang, S., Sand, D. J., Valenti, S., et al. 2019, ApJ, 875, 59

Yao, Y., Miller, A. A., Kulkarni, S. R., et al. 2019, ApJ, 886, 152

Yaron, O., & Gal-Yam, A. 2012, PASP, 124, 668

Yoon, S. C., & Langer, N. 2005, A&A, 435, 967

Zeng, X., Wang, X., Esamdin, A., et al. 2021, ApJ, 919, 49

Zhang, K., Wang, X., Zhang, J., et al. 2016, ApJ, 820, 67

Zheng, W., Kelly, P. L., & Filippenko, A. V. 2018, ApJ, 858, 104